Wide Bandgap Conjugated Polymer Donors based on Alkyloxime Substituted Thiophene for Organic Solar Cells

by

Yunsheng Jiang

A thesis

presented to the University of Waterloo

in fulfilment of the

thesis requirement for the degree of

Master of Applied Science

in

Chemical Engineering

Waterloo, Ontario, Canada, 2021

Author's Declaration

I hereby declare that I am the sole author of this thesis. This is a true copy of the thesis, including any required final revisions, as accepted by my examiners.

I understand that my thesis may be made electronically available to the public.

Abstract

Remarkable progress has been made for non-fullerene based organic solar cells (OSCs), with a power conversion efficiency (PCE) of over 18% having been achieved. Conjugated polymer donors consisting of alternating donor and acceptor units can form complementary light absorption and suitable energy levels with non-fullerene acceptors. Thus, rational design and matching of the conjugated polymer donor with narrow bandgap non-fullerene acceptors (NFAs) is essential for breakthroughs in OSC performance.

By incorporating the thiophene unit as a π bridge between the donor unit (BDT) and the acceptor unit (oxime substituted thiophene (TO)), a new wide bandgap polymer donor TTOT was designed, synthesized, and characterized. It exhibited wide optical bandgap of 1.98 eV, and the energy of the highest occupied molecular orbital (E_{HOMO}) of TTOT was -5.33 eV. In addition, TTOT polymer neat film showed a high hole mobility of up to 3.36×10^{-3} $cm^2V^{-1}s^{-1}$. By matching with the non-fullerene acceptor Y6, the as-cast TTOT-based OSC achieved a PCE of 7.65%, J_{SC} of 23.58 mA/cm^2, V_{OC} of 0.62 V, and FF of 0.52. However, the incorporation of electron-donating thiophene spaces led to a rise in E_{HOMO} to -5.33 eV, which resulted in the relatively low V_{OC} of the OSCs.

To further improve the V_{OC} of TTOT-based OSC, a halogenation strategy was adopted to downshift the E_{HOMO} of TTOT. Two new wide bandgap polymer donors TTOTF and TTOTCl were designed and synthesized by substituting BDT with fluorinated BDTTDFSn and chlorinated BDTTDClSn, respectively. Both polymers have wide optical bandgaps of over 1.97 eV, with E_{HOMO}'s of -5.46 eV (TTOTF) and -5.48 eV (TTOTCl). Then Y6 was chosen as the acceptor to investigate the photovoltaic performance. The best TTOTF-based OSC device showed good device performance with a J_{SC} of 27.61 mA/cm^2, improved V_{OC} of 0.72 V and FF

of 0.69, resulting in an almost two-fold higher PCE of 13.57% when comparing with TTOT based OSCs. Furthermore, the optimized TTOTCl-based OSC device showed an even higher PCE of 14.91%, V_{OC} of 0.70 V, FF of 0.68 and a record-high J_{SC} of 31.03 mA/cm^2 among non-fullerene OSCs. The largely increased FF and J_{SC} are the results of the considerably improved SCLC hole mobility of TTOTF and TTOTCl in OSCs. In addition, the optimized TTOTF and TTOTCl-based OSC devices demonstrated excellent long-term air stability, retaining nearly 80% PCE after 2 months without encapsulation.

Lastly, to further improve the device performance of TTOTCl-based OSCs, some future directions are proposed. The first approach is to match TTOTCl with non-fullerene acceptors that have higher E_{HOMO}'s than Y6. As a result, the HOMO offset between donor and acceptor can be reduced, resulting in a lower energy loss and higher device performance. The second approach is to optimize TTOTCl-based OSC through incorporating LiTFSI as a hole transport enhancement layer. The OSCs with a thin LiTFSI layer achieved an excellent PCE of 15.96%, with an enhanced V_{OC} of 0.72 V and FF of 0.71. Further investigations are needed to fully understand the effect and improve the film quality of the LiTFSI layer.

This thesis demonstrated the use of thiophene π spacers with fluorine or chlorine substitutions are highly effective for reducing energy loss, enhancing charge carrier mobility, and improving film morphology in OSCs. In addition, the TO-based polymer TTOTCl is a very promising donor material for fabricating highly efficient and air stable OSCs.

Acknowledgements

I would like to express my sincere thanks to my supervisors, Prof. Yuning Li and Prof. Bo Cui, who offered me the opportunity to pursue my interest in research. My supervisors have always provided guidance, support, and encouragement during my master's program.

I would like to give deepest thanks to Keqiang He for being helpful and supportive in the labs and providing me valuable advice.

I also wish to thank my colleagues, Zhaoyi Yin, John Polena, Yuan Yi, Pankaj Kumar, Xiguang Gao, Dr Marwa Abd-Ellah and Dr. Jenner Ngai. Thank you all for the help and valuable discussions throughout my master's program.

Many thanks to the committee members, Prof. Eric Croiset and Prof. Xianshe Feng for reading my thesis and giving insightful feedback.

Lastly, I would like to thank my family and friends for their constant support.

Table of Contents

List of Figures

List of Tables

List of Abbreviations

AFM: atomic force microscopy

BHJ: bulk heterojunction

CV: cyclic voltammetry

DFT: density functional theory

DSC: differential scanning calorimetry

EQE: external quenching efficiency

ETL: electron transport layer

FF: fill factor

FMO: frontier molecular orbital

GPC: gel permeation chromatography

HTL: hole transport layer

J-V: current density-voltage

NFA: non-fullerene acceptor

NMR: nuclear magnetic resonance

OPV: organic photovoltaic

OSC: organic solar cell

PCE: power conversion efficiency

PL: photoluminescence

RMS: root mean square

SCLC: space charge limited current

SMA: small molecular acceptor

TGA: thermogravimetric analysis

UV-vis: ultraviolet-visible

WBG: wide bandgap

XRD: X-ray diffraction

List of Symbols

E_g^{opt}: optical bandgap

E_{HOMO}: energy of the highest occupied molecular orbital

E_{LUMO}: energy of the lowest unoccupied molecular orbital

J_{SC}: short-circuit current density

M_n: number average molecular weight

M_w: mass average molecular weight

V_{OC}: open circuit voltage

λ_{max}: maximum absorption wavelength

μ_h: hole mobility

μ_e: electron mobility

Chapter 1 Introduction

1.1 Overview of organic solar cell

With the increasing need for renewable energy, solar photovoltaic technology has been the subject of widespread attention in the past several decades. Silicon-based solar cells are the dominant contributor in the solar cell market, as they can easily achieve power conversion efficiencies (PCEs) up to 24% in large-area commercial cases.[1] Organic solar cells (OSCs), acting as the alternative candidate for silicon-based solar cells, have the advantages of low fabrication cost, ease of mass manufacturing, lightweight properties and mechanical flexibility.[2,3,4] The most known high-efficient organic solar cells are constructed using a bulk heterojunction (BHJ) structure with a p-type conjugated polymer as a donor and an n-type semiconductor as an acceptor.[5] Among all the acceptor materials, non-fullerene acceptors (NFAs) are widely used in recent years due to their tunable optical and electronic properties, better thermal and photochemical stability, and longer device lifetimes when comparing with traditional fullerene acceptors.[6,7] In addition, PCEs over 18% were discovered in non-fullerene based OSCs.[8,9] Conjugated polymer donors with wide optical bandgaps have the advantage of forming a complementary light absorption range with narrow bandgap NFAs, and their tunable frontier molecular orbital (FMO) energy levels make them match well with most of the NFAs (ITIC, IT-4F, Y6 and etc.). Thus, rational design and matching of the conjugated polymer donor with narrow bandgap NFAs is essential for achieving breakthroughs in PCE.

1.2 Working mechanism of bulk heterojunction organic solar cells

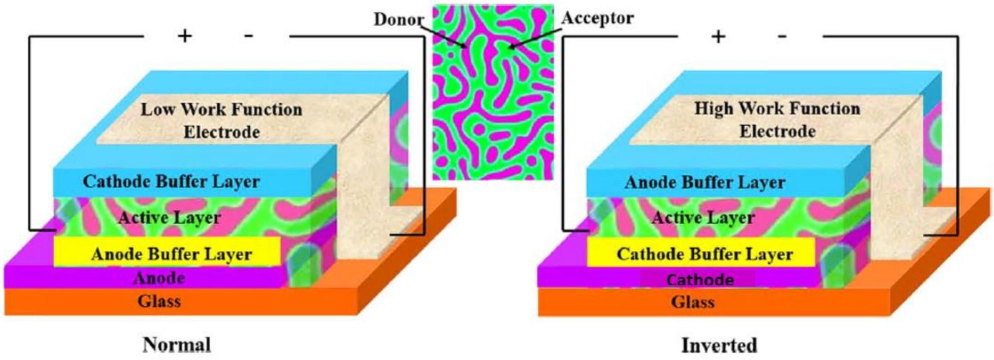

Figure 1-1. Device structures of the (a) conventional and the (b) inverted BHJ OSCs.[10]

As shown in Figure 1-1, the typical structure of a BHJ OSC contains an active layer that consists of a blend of donor and acceptor materials to form a nanoscale phase separation and bicontinuous interpenetrating network.[11] The active layer is sandwiched between the cathode buffer layer and anode buffer layer, otherwise referred to as the electron transport layer (ETL) and hole transport layer (HTL), respectively. These interfacial layers between the active layer and the electrodes enhanced the solar cell performance and stability in BHJ OSCs.[12] Furthermore, many studies have shown that the inverted configuration tends to exhibit higher environmental stability than the normal configuration for OSC devices.[13,14,15]

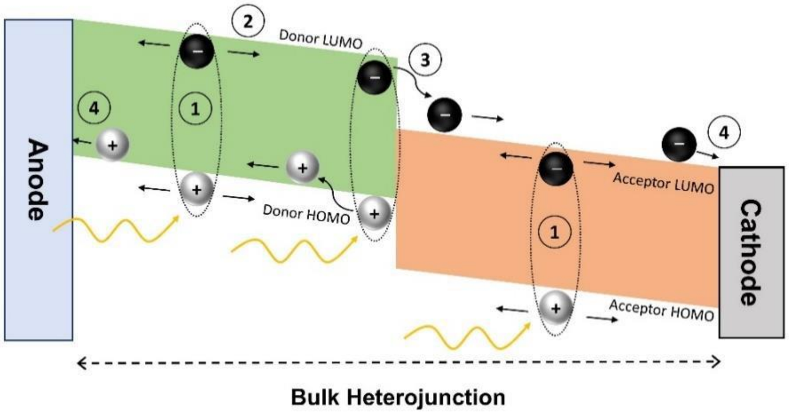

Figure 1-2. Schematic illustrations of the working mechanism in BHJ OSCs.[16]

As illustrated in Figure 1-2, the working mechanism of BHJ OSCs can be summarized into four elementary steps: (1) light absorption and exciton generation; (2) exciton diffusion; (3) charge dissociation; (4) charge transportation and collection. The initial step is the absorption of the sunlight, followed by the generation of an electron and hole pair in the active layer. More specifically, the electron is excited from the highest occupied molecular orbital (HOMO) to the lowest unoccupied molecular orbital (LUMO) in the donor material upon the absorption of a photon. Then the photogenerated excitons need to diffuse to the donor/acceptor interface before recombination, and the diffusion lengths are varied from 5 to 15 nm for conjugated polymer donors.[17,18,19,20] The third step is driven by the offset between LUMO energy levels of the donor and acceptor materials, occurring when the electron is transferred from the LUMO of donor to the LUMO of acceptor. After the dissociation process, the charge carriers will be transported to the corresponding electrodes through the interpenetrated donor and acceptor pathways. Lastly, the collected charge carriers at respective electrodes will produce photocurrents.

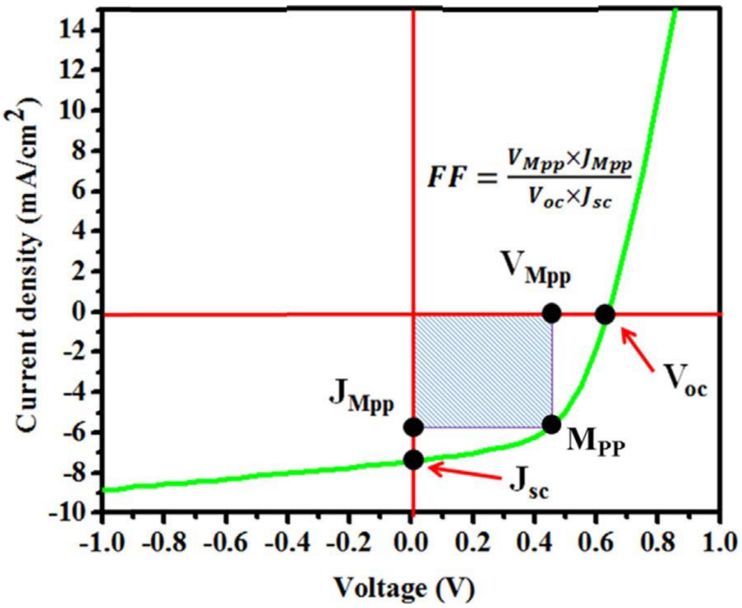

Figure 1-3. Current density – voltage (J-V) curve of OSC device.[10]

To evaluate the OSC device performance, the current density-voltage (J-V) measurement is utilized to calculate PCE and to characterize performance parameters, such as short circuit current density (J_{SC}), open circuit voltage (V_{OC}) and fill factor (FF). Figure 1-3 showed a typical J-V curve of an OSC device, where J_{MPP} and V_{MPP} represents the current density and voltage at the maximum power. J_{SC}, V_{OC}, J_{MPP} and V_{MPP} can be simply obtained from the J-V curve, and FF is expressed in Equation (1):

$$FF = \frac{J_{MPP} \times V_{MPP}}{V_{OC} \times J_{SC}} \tag{1}$$

Then the overall PCE can be calculated according to Equation (2):

$$PCE = \frac{V_{OC} \times J_{SC} \times \mathrm{FF}}{P_{in}} \tag{2}$$

Where P_{in} is the input power, equalling to 100 MW/cm^2 under AM 1.5G illumination.

As can be seen in equation (2), since the characteristic parameters (J_{SC}, V_{OC}, FF) are proportional to the PCE, these values should be maximized to enhance the OSC device performance.

1.3 Non fullerene acceptors for organic solar cell

Comparing with NFAs, traditional fullerene acceptors, such as C_{60}, $PC_{61}BM$ and $PC_{71}BM$, have the drawbacks of poor light absorption, limited chemical-structure and energy-level tunability, high synthetic cost, and weak morphological stability.[21,22,23] In addition, a large energy loss of 0.8 to 1.0 eV was revealed in fullerene-based OSCs.[24] As a result, the PCE of the best fullerene acceptor based OSC was only around 12%.[25] In contrast, remarkable progress has been made for NFAs in the past few years. Benefiting from the tunable energy levels, good light absorption and flexible geometry, PCEs over 18% were achieved in non-fullerene based OSCs.[8,9]

Among the non-fullerene acceptors, significant effort has been devoted to small molecule acceptors (SMAs) due to their advantages of adjustable chemical structure and excellent repeatability in batch-to-batch production when comparing with polymer acceptors.[23,26] Thus, two novel series of SMAs, indacenodithiophene (IDT)-based acceptors and Y-series acceptors will be briefly illustrated.

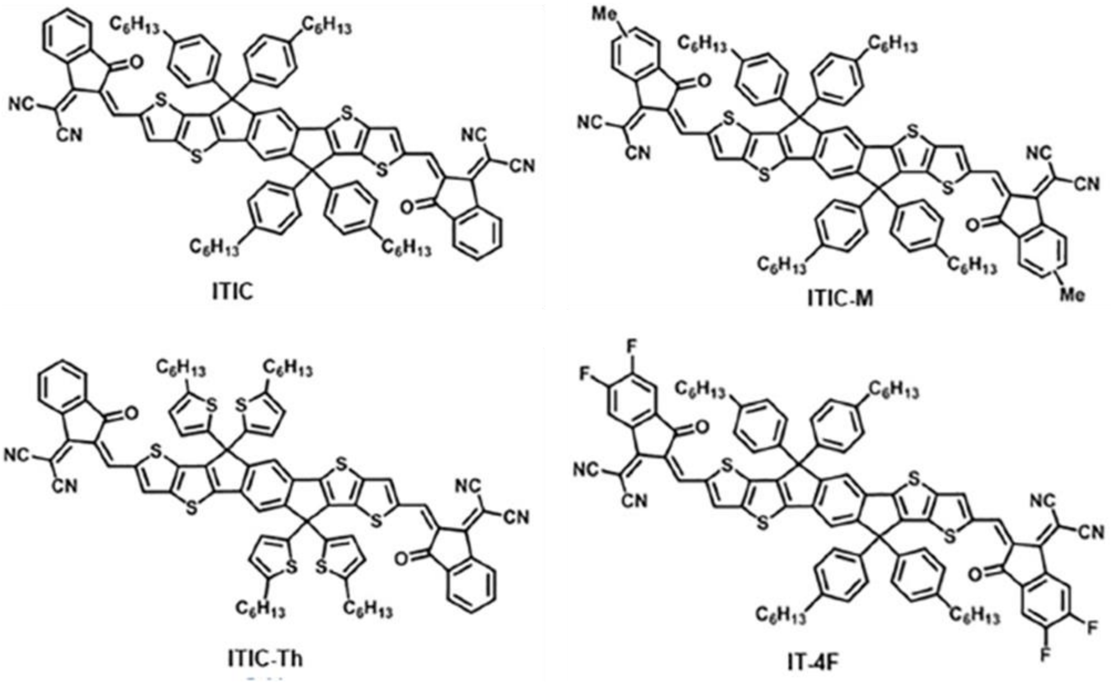

Figure 1-4. Chemical structures of representative IDT-based non-fullerene SMAs.

Figure 1-4 display chemical structures of some representative IDT-based acceptors. Typically, IDT-based SMAs consist of three parts: 5-11 linearly fused and ladder-type aromatic rings, 4 solubilizing alkyl or alkylaryl side chains, and 2 electron-withdrawing end units which can be easily modified to tune optical and electrochemical properties.[27] For example, IT-4F, the best performing member in IDT-based acceptor family, was synthesized through the fluorination on the four end-capping units on ITIC. IT-4F based OSC devices achieved PCEs over 14% when matching with wide bandgap polymer donors.[28,29,30]

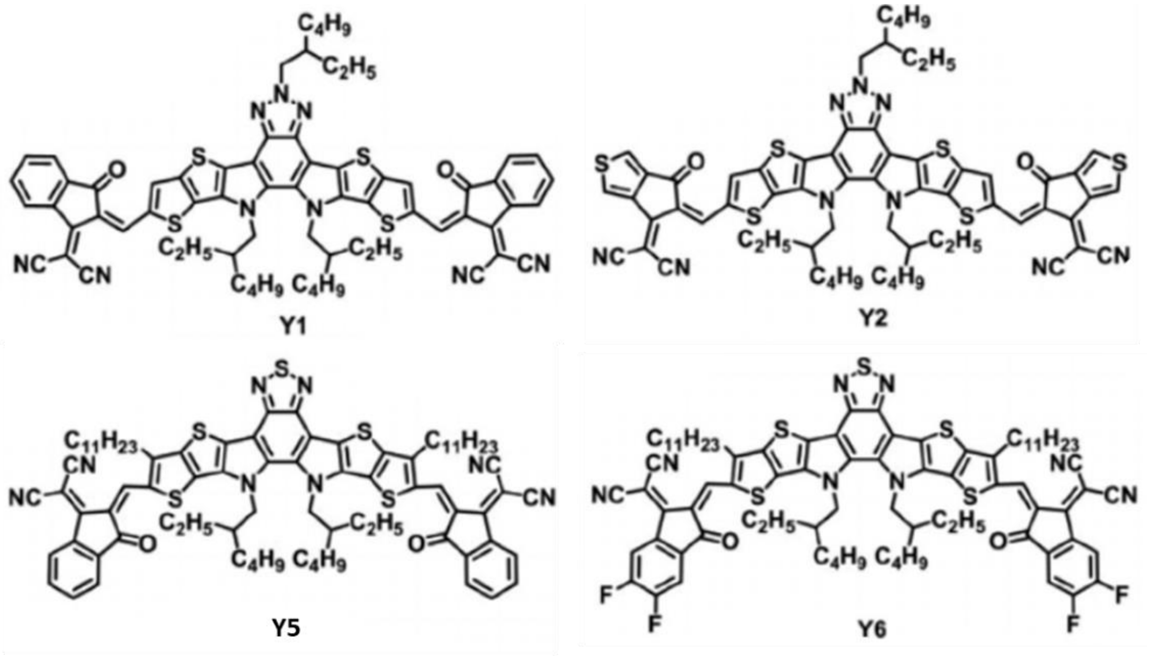

Figure 1-5. Chemical structures of representative Y-series non-fullerene SMAs.

Figure 1-5 shows the chemical structure of some representative Y-series acceptors. Unlike IDT-based fused-ring electron acceptors, Y-series acceptors utilize an electron deficient core with multiple nitrogen atoms on the pyrrole rings, leading to high electron mobility and low energy loss in the OSCs.[31] As a result, the PCEs of OSCs utilizing Y-series acceptors were boosted to over 17%, making them the best performing acceptors to date.[9,32,33,34]

1.4 Wide bandgap polymer donors for organic solar cell

Based on the optical bandgap (E_g^{opt}), polymer donors can be classified into three categories: low bandgap (LBG, $E_g^{opt} < 1.6$ eV), medium bandgap (MBG, 1.6 eV $< E_g^{opt} <$ 1.8 eV) and wide bandgap (WBG, $E_g^{opt} > 1.8$ eV).[35,36] Among them, MBG and WBG polymer donors have been the subject of widespread attention due to their abilities to form complementary light absorption with NFAs. Comparing with MBG polymer donors, WBG polymer donors can easily achieve over 16% PCE in OSC devices.[37,38,39,40] Currently, the highest performing non-fullerene OSC device constructed uses a WBG polymer as the donor.[9]

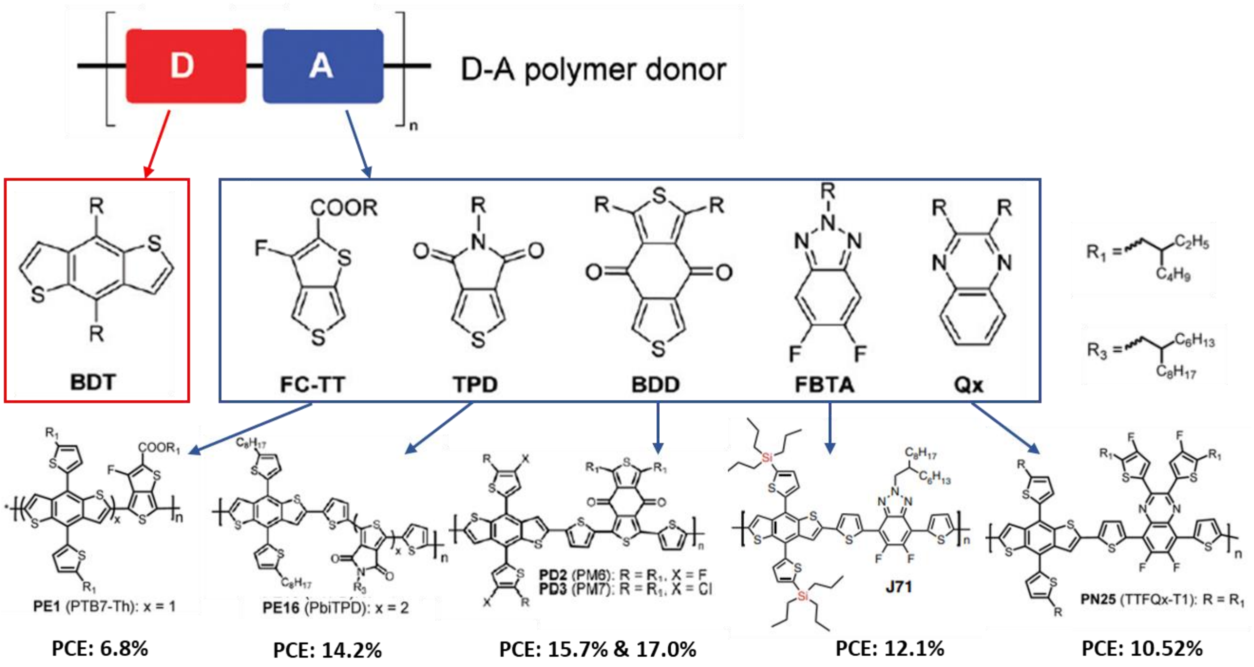

Figure 1-6. Molecular structures of representative BDT-based polymer donors with different A building blocks.[41,42,34,43,44,45]

The emergence of D-A type polymers consisting of alternating electron donor (D) and electron acceptor (A) moieties has dominated the WBG conjugated polymer donor design in the past decade.[46] The incorporation of selected repeating D and A units into the polymer backbone can rationally tune the optical and electronic properties of polymer donor. This so-called "push-pull" effect can allow polymer donor being designed in a way that can match well with particular NFA based on light absorption range, energy levels and charge carrier mobility.[47]

Most of the high-performance (PCE >16%) WBG polymer donors were using benzo[1,2-b:4,5-b']dithiophene (BDT) based building blocks as the D unit. Whereas representative A building blocks include FC-TT, TPD, BDD, FBTA and Qx.[48] The representative conjugated polymer donor designed based on the above mentioned building blocks are shown in Figure 1-6. The PCE of OSC based on different combination of D and A building blocks can vary significantly when matching with non-fullerene acceptors. Thus, rational design and careful selection of D and A building blocks are essential for the further improvement and achieving breakthroughs in OSCs.

1.5 π spacer and halogenation strategies for polymer donor design

In the past decade, various techniques have been successfully implemented to design polymer donors for highly efficient OSCs.[49,50,51,52] Among them, halogenation strategies such as fluorination and chlorination can effectively lower the HOMO energy level of the polymer donor, resulting in better compatibility with NFAs and higher V_{OC}'s in the OSCs.[34,53,54] In 2018, Hou's group designed and synthesized two novel conjugated polymer donors PBDB-T-2F and PBDB-T-2Cl through fluorination and chlorination strategy, respectively.[55,29] By doing so, they successfully downshifted the HOMO energy level of the non-halogenated polymer PBDB-T from -5.34 eV to -5.50 eV (PBDB-T-2F) and -5.52 eV (PBDB-T-2Cl). As a result, OSCs based on these two polymer donors exhibited lower energy losses and notably improved PCEs of 13.2% (PBDB-T-2F) and 14.4% (PBDB-T-2Cl) in comparison to PBDB-T based OSCs.

Furthermore, spacers such as thiophene, thiazole, selenophene, furan and thieno[3,2-b]thiophene are widely incorporated in conjugated polymer donors as a π bridge to enhance hole mobility in OSCs by improving backbone planarity, reducing steric hindrance and facilitating electron delocalization.[56,39,57,58,59,60,61] For example, PB3T was designed by incorporating a thiophene unit between the two identical acceptor units in the conjugated polymer donor PB2T. According to the DFT simulations, the main backbone twisting angle was largely improved from 87° in PB2T to 17° in PB3T. Consequently, dramatic hole mobility (6.4×10^{-8} $cm^2V^{-1}s^{-1}$ to $1.1 \times$

10^{-4} $cm^2V^{-1}s^{-1}$) and PCE (0.08% to 11.7%) improvements were revealed in the OSC devices when matching with the acceptor IT-M.[62]

In this thesis, the above-mentioned halogenation strategy and the incorporation of spacers will be combined to design conjugated polymer donors for highly efficient OSCs.

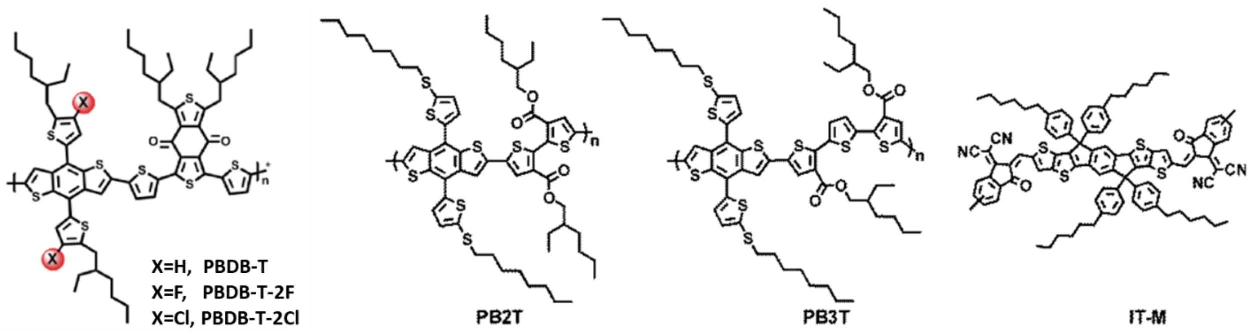

Figure 1-7. Molecular structures of PBDB-T, PBDB-T-2F, PBDB-T-2Cl, PB2T, PB3T and IT-M.

1.6 Polymer and OSC device characterization tools and methods

Polymer characterization methods used in this thesis include nuclear magnetic resonance (NMR), cyclic voltammetry (CV), ultraviolet-visible (UV-vis) spectroscopy, gel permeation chromatography (GPC), differential scanning calorimetry (DSC) and thermogravimetric analysis (TGA). Whereas OSC devices related characterization techniques are photoluminescence (PL), external quenching efficiency (EQE) and space charge limited current (SCLC). Finally, atomic force microscopy (AFM) and X-ray diffraction (XRD) were utilized to characterize the morphology of polymers and OSC devices.

NMR spectroscopy

NMR spectroscopy was utilized to analyze product purity and to confirm the molecular structure of the synthesized organic compound. For example, when a nucleus is placed in a strong magnetic field, it will start to spin and cause energy transfer. A unique resonance frequency will then be generated along with the energy transition and will be detected by radio receivers to form NMR spectra. In this work, chemical shifts (δ) were reported as values (ppm) relative to the reference compound tetramethylsilane (0 ppm) and ^{1}H NMR and ^{13}C NMR spectra were recorded on Bruker DPX 300-MHz in chloroform.

CV measurement

CV was utilized to study the electrochemical properties of polymers. A three-electrode cell was used, where both the auxiliary and working electrodes are made of platinum rods and the reference electrode uses Ag/AgCl. A dry acetonitrile solution containing 0.1 M n-Bu_4NPF_6 was used as an electrolyte and at a scan rate of 100 mVs^{-1}. Then the HOMO energy level of the polymer materials was estimated by the oxidation onset potential vs. Fc/Fc^{+}:

$$E_{HOMO}(eV) = -e\,({E_{onset}}^{ox}) - 4.8\ eV \tag{3}$$

All data were obtained on a CHI600E electrochemical analyzer.

UV-vis spectroscopy

UV-vis spectroscopy was utilized to determine the optical properties of the polymers. The UV absorption spectra of both polymer thin films and solutions can be measured to identify the absorption range, molecular packing behaviour and E_g^{opt} of the materials. The E_g^{opt} can be estimated through the equation shown below:

$$E_g{}^{opt}(eV) = h\frac{c}{\lambda_{onset}} = \frac{1240\ (eVnm)}{\lambda_{onset}\ (nm)} \tag{4}$$

Where h is the Planck constant, c is the speed of light in vacuum and λ_{onset} represents the onset value of absorption spectrum in thin film.

Then the LUMO energy level of the polymers can be calculated by:

$$E_{LUMO}(eV) = E_g{}^{opt}(eV) + E_{HOMO}(eV) \quad (5)$$

All measurements were carried out on a Cary 7000 Universal Measurement Spectrophotometer (UMS).

GPC measurement

GPC measurement was conducted to analyze the dispersity (*Đ*), number average molecular weight (M_n) and mass average molecular weight (M_w) of the polymer. The column used for GPC is packed with size-controlled porous gels to separate molecules regarding to their sizes in eluent, where organic solvents are used for organic polymers.

All measurements were performed on a Malvern HT-GPC system at a column temperature of 110 °C using 1,2,4-trichlorobenzene as the eluent and polystyrene as the standard.

DSC and TGA measurements

Thermal properties of polymers were studied through DSC and TGA analysis. The weight loss of polymers at different heating temperatures can be monitored through TGA. Polymer thermal stability can be determined through the thermal degradation profile. DSC can be employed to investigate the thermal phase transition of the polymers by monitoring the heat flow and temperature. For amorphous polymers, glass transition temperature (T_g) can be determined, whereas for semicrystalline polymers, T_g, crystallization temperature (T_c) and melting temperature (T_m) can be observed.

All TGA and DSC measurements were carried out on a TA Instruments SDT 2960 under nitrogen at a scan rate of 10 and 20 °Cmin^{-1}, respectively.

PL measurement

The effectiveness of photoinduced charge transfer can be determined through PL measurements. By exciting the material valence states at a specific wavelength, the PL spectrum is obtained by recording the emission intensity. To get a high PL quenching efficiency, the HOMO or LUMO offset of selected donor and acceptor materials must be sufficient and the miscibility of the two materials need to be sufficient as well.

All photoluminescence spectra were recorded on Horiba PTI QuantaMasterTM 8000 Series Fluorimeter.

EQE measurement

Quenching efficiency was utilized to characterize the device's incident photon conversion efficiency at different wavelengths. It is calculated according to the equation:

$$External\ quenching\ efficiency\ (EQE) = \frac{Number\ of\ charge\ carriers\ collected}{Number\ of\ incident\ photons} \tag{6}$$

The EQE measurement (PV Measurements, QEX10) of TTOTCl-based OSC was carried out under monochromatic light as filtered by a dual grating monochromator from a xenon arc lamp source, coupled with a germanium photodiode. The EQE of the TTOT and TTOTF-based devices were measured by an ORIEL IQE200B system from Newport.

SCLC mobility measurement

SCLC mobility measurements were carried out in single carrier devices to study the charge carrier mobilities of polymers and blend films. Hole-only and electron-only devices with configurations of ITO/PEDOT:PSS (40nm)/Active layer/MoO_3 (10 nm)/Ag (100 nm) and ITO/ZnO (40 nm)/Active layer/LiF (1 nm)/Al (100 nm), respectively, were fabricated. Hole and electron mobilities are calculated by fitting the dark J-V curves of the devices using Mott-Gurney equation:

$$J = \frac{9\varepsilon_0 \varepsilon_r \mu V^2}{8L^3} \tag{7}$$

where ε_0 is the permittivity of the free space (8.8542 × 10 $C^{-}V^{-1}m^{-1}$), ε_r is the active layer dielectric constant, μ is the carrier mobility and L is active layer thickness.[63]

Furthermore, the dielectric constant (ε_r) of the active layer material can be calculated using the equation:

$$\varepsilon_r = \frac{Cd}{\varepsilon_0 A} \tag{8}$$

where C is the capacitance, $\varepsilon_0 = 8.8542 \times 10^{-12}\ \mathrm{Fm}^{-1}$, A is the active device area and d is the active layer material thickness.

AFM and XRD characterizations

The surface morphology of the active layer was examined through AFM and the molecular packing of polymer donors and blend film was studied by XRD measurements.

AFM images were recorded on a Dimension 3100 scanning probe microscope. All XRD patterns were collected by a Bruker D8 Discover powder diffractometer with a standard Bragg–Bretano geometry using Cu Kα radiation ($\lambda = 1.5418$ Å).

1.7 Objective and thesis outline

Rapid progress has been made for non-fullerene based OSCs in recent years. However, in addition to aiming for high PCEs, it is also essential to develop new WBG polymers with low synthetic cost and long-term environmental stability to work towards commercialization.[64,65]

Several techniques have been employed to design polymer donors to form complementary light absorption and suitable energy levels with NFAs.

In Chapter 2, a new wide bandgap conjugated polymer donor TTOT was designed and synthesized. DFT simulations were conducted to study the influence of the thiophene spacers. The synthetic route and synthesis methods of TTOT were given. The thermal, optical, and electrochemical properties of TTOT was then characterized. Y6 was chosen as the acceptor and inverted device structure was used to investigate the photovoltaic performance. SCLC mobility measurement, PL quenching experiment and EQE measurement were carried out to further understand the device performance. Lastly, AFM and XRD were adopted to characterize the thin film morphology and microstructure.

In Chapter 3, two new wide bandgap conjugated polymers TTOTF and TTOTCl were designed and synthesized. DFT simulations were conducted to study the influence of the fluorine and chlorine atoms. The polymerization methods of TTOTF and TTOTCl were given. The thermal, optical, and electrochemical properties of TTOT was then characterized. The photovoltaic properties of these two polymers were studied by J-V curves, SCLC mobility measurement, PL quenching experiment, EQE measurement and 2-month stability test. Thin film morphology and microstructure were investigated by AFM and XRD.

In Chapter 4, a summary of this thesis and proposed future directions will be provided.

Chapter 2 Synthesis and characterization of TTOT polymer

2.1 Introduction

Recently, our group found that the weakly electron-withdrawing alkyloxime-substituted thiophene (TO) is a very promising building block for the development of high-performance wide bandgap polymer donors for NFA-based OSCs.[66,67] PTOBT and PBDTTO, which are copolymers of TO with common electron donating building blocks, bithiophene (BT) and benzodithiophene (BDT), have shown complementary light absorption and matching FMO energy levels with those of ITIC and Y6, reaching high PCE of 9.04% and 13.29%, respectively. One attractive feature of TO is its simple synthesis, which can effectively reduce the synthetic complexity and eventually the cost of OSCs, which is essential for the practical application of OSCs. While PTOBT showed a high hole mobility of up to 1.64 × 10^{-2} $cm^2V^{-1}s^{-1}$ as the active layer in organic thin film transistors (OTFTs), its SCLC hole mobility is three orders of magnitude lower (6.73 × 10^{-5} $cm^2V^{-1}s^{-1}$), due to the unfavourable edge-on crystal orientation of the polymer chains in the thin film. The low SCLC hole mobility resulted in in a relatively low FF of 0.5 for the OSC devices.[66] By replacing the BT donor units with the larger fused BDT units, the resultant PBDTTO showed improved SCLC hole mobility of up to 2.05 × 10^{-4} $cm^2V^{-1}s^{-1}$.[67] Although the FF of the OSC device was improved to 0.59, it is still inferior to the state-of-the art FF values (up to 0.78).[50] We found that the chain packing in the PBDTTO film is rather disordered, which is likely caused by the steric repulsion of the alkyloxime side chains and the adjacent BDT unit.

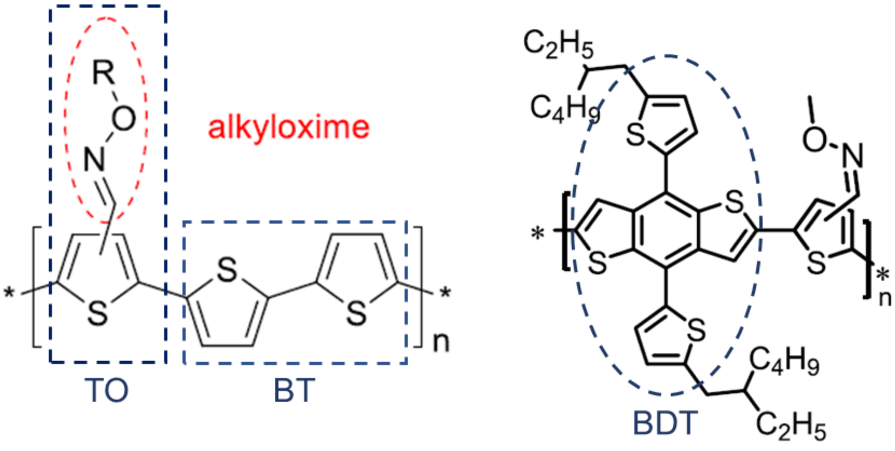

PTOBT **PBDTTO**

Figure 2-1. Chemical structures of PTOBT and PBDTTO.

As mentioned in Chapter 1, π-spacers are widely utilized in conjugated polymer donors as π bridges to enhance hole mobility in OSCs. Thus, to further reduce steric hindrance and improve backbone planarity of BDT-TO-based polymer donors, a thiophene unit was employed between the BDT and TO unit to enhance SCLC hole mobility. The resultant polymer poly{(Z)-5''-(4,8-bis(5-(2-ethylhexyl)thiophen-2-yl)-6-methylbenzo[1,2-b:4,5-b']dithiophen-2-yl)-5-methyl-[2,2':5',2''-terthiophene]-3'-carbaldehyde O-(2-butyloctyl) oxime}(TTOT) indeed showed a greatly enhanced SCLC mobility of up to 3.36 × 10^{-3} $cm^2V^{-1}s^{-1}$. By matching with the non-fullerene acceptor Y6, the best TTOT-based OSC device showed good device performance with a J_{SC} of 23.58 mA/cm^2, V_{OC} of 0.62 V, FF of 0.52 and PCE of 7.65%. However, the incorporation of electron-donating thiophene spaces led to a rise in the E_{HOMO} to -5.33 eV, which resulted in the relatively low V_{OC} of the OSCs.

In this chapter, the synthesis as well as the detailed characterizations of TTOT polymer will be provided. The photovoltaic properties, surface morphology and molecular packing of TTOT will also be investigated. At the end, the conclusion and future directions will be given.

2.2 Structure simulation by density functional theory

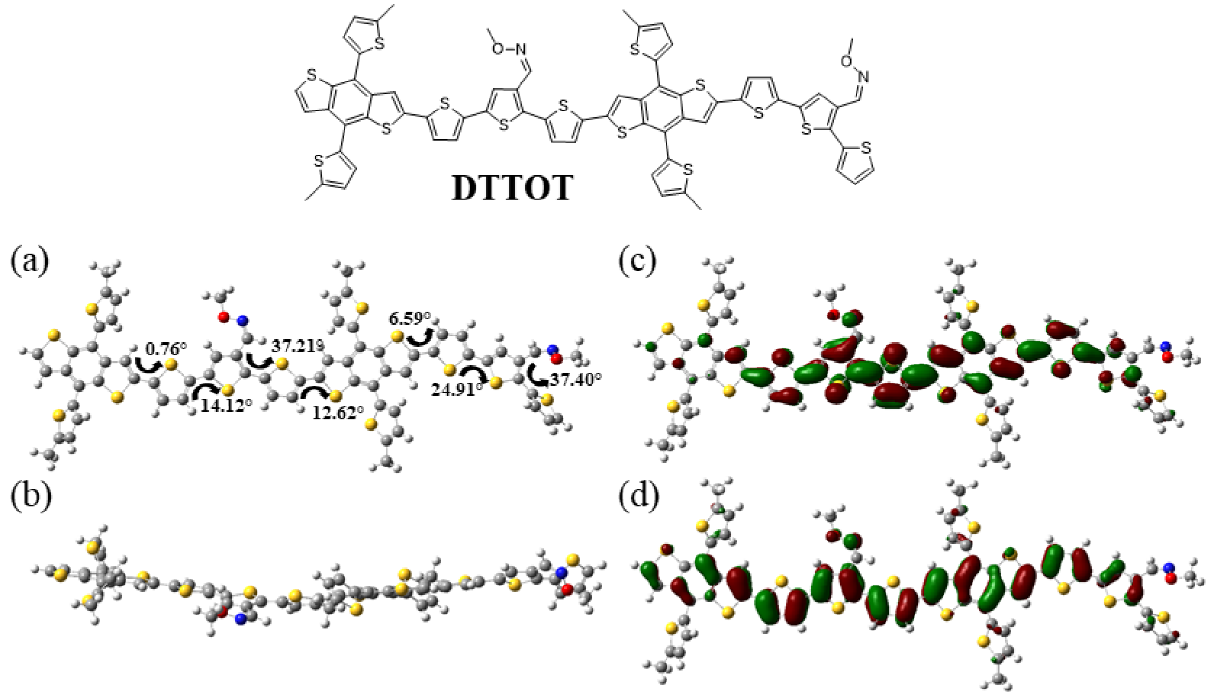

Figure 2-2. Chemical structure, top and side view of DFT computed molecular geometry, LUMO, and HOMO of compound DTTOT (a, b, c, d).

The density functional theory (DFT) calculations were carried out by Gaussian 09 with a hybrid B3LYP correlation function and 6-31G (d) basis set. The simulation was conducted on the dimer unit of TTOT, namely, DTTOT. The influence of the incorporation of the thiophene spacer was investigated, where the 2-ethylhexyl side chains on BDT unit and the 2-butyloctyl side chain on the TO unit were replaced by methyl group to reduce computation time.

As shown in Figure 2-2, the dihedral angle of PBDTTO was reduced from 38.8° to 37.2° by utilizing the thiophene unit as a π-bridge between the BDT and TO unit.[67] The slightly more planar backbone structure of DTTOT is essential for achieving a higher SCLC hole mobility in OSCs. Furthermore, DTTOT exhibited delocalized electrons for both HOMO and LUMO along the conjugated backbone, which is also essential for efficient charge separation.[68,69,70]

2.3 Synthesis of TTOT

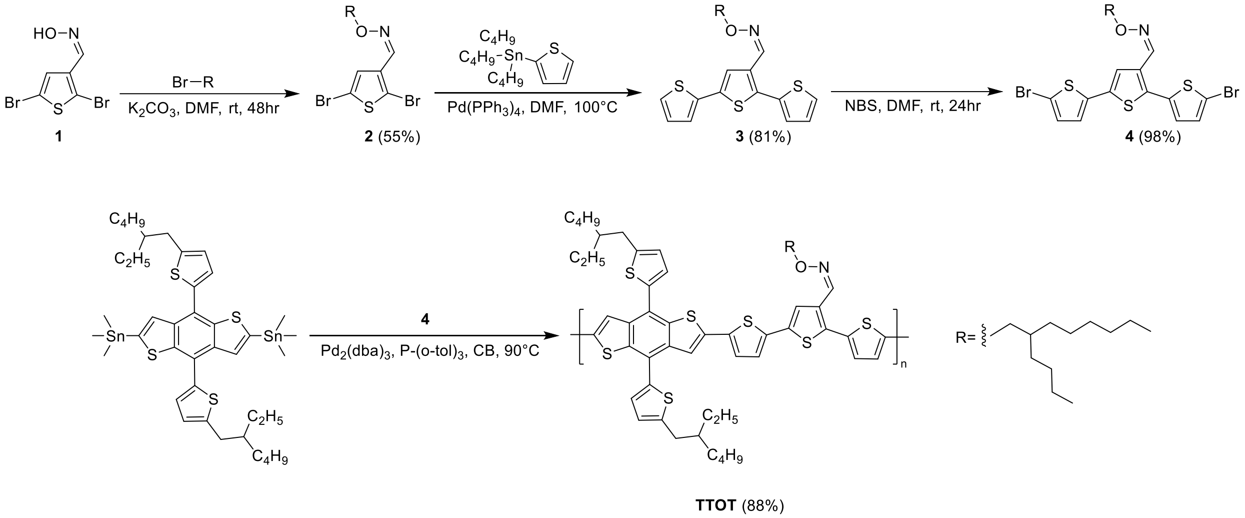

Figure 2-3. Synthetic route of TTOT.

The synthetic route of TTOT polymer is shown in Figure 2-3. (Z)-2,5-dibromothiophene-3-carbaldehyde oxime (**1**) was prepared through two simple and high-yield steps as previously reported.[66] Pure compound **2** was obtained through alkylation reaction using 2-butyloctyl bromide. It was then copolymerized with commercially available 2-(tributylstannyl) thiophene through a palladium-catalyzed Stille coupling reaction to form compound **3** with a yield of 81%, followed by a 98% yield bromination reaction using N-bromosuccinimide to obtain monomer compound **4**. Lastly, polymer TTOT was synthesized under a typical Stille cross coupling condition, and it showed good solubility in both chloroform and chlorobenzene.

Detailed synthesis procedures and NMR spectra are included in the experimental section.

2.4 Characterization of TTOT

2.4.1 Thermal properties

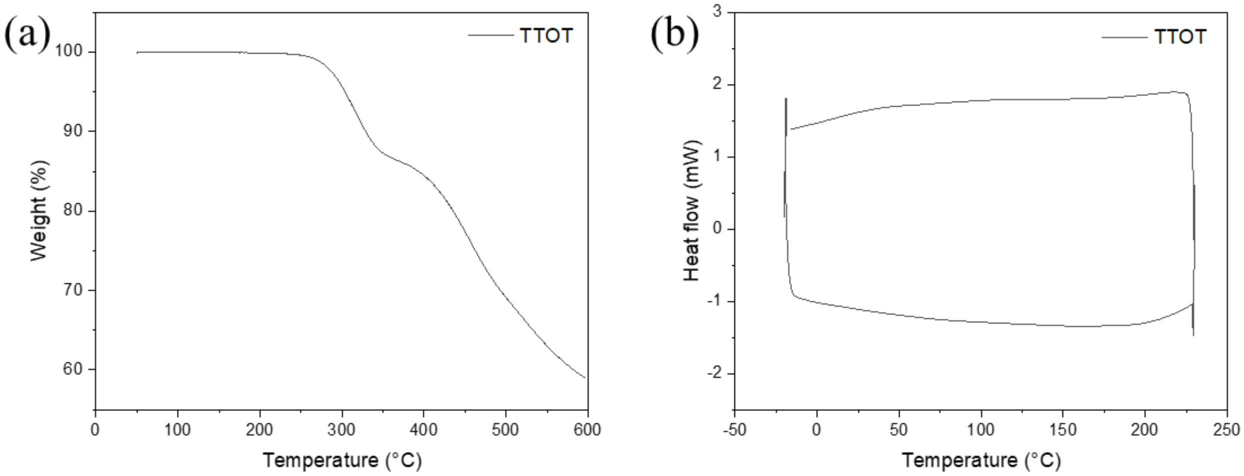

Figure 2-4. (a) TGA and (b) DSC curves of TTOT.

The thermal properties were studied by TGA and DSC. TGA result was shown in Figure 2-4 (a). TTOT polymer showed a 1% and 5% weight loss at temperature of 269 and 304°C, respectively, demonstrating a good thermal stability of TTOT for OSC devices. The DSC curves was shown in Figure 2-4 (b) at a temperature range of -20 to 230°C. No obvious phase transition peaks were observed in either endothermic or endothermic process, indicating the poor crystallinity of TTOT polymer or the decomposition temperature is lower than the melting point.

2.4.2 Optical and electrochemical properties

The optical property of TTOT polymer was investigated by UV-Vis spectroscopy. Figure 2-5 (a) shows the absorption spectrum of the polymer in chloroform solution, in thin films without annealing and annealed at 100°C. In chloroform solution, TTOT has a maximum absorption wavelength (λ_{max}) located at 536 nm and no pre-aggregation behaviour was observed. Whereas TTOT thin film showed a λ_{max} at 539 nm and a shoulder peak around 568 nm, which is attributed to the π-π stacking of the polymer backbones. In addition, the shoulder peak was intensified at an annealing temperature of 100°C, indicating a more ordered molecular packing in solid state after thermal annealing. The optical bandgap of TTOT was calculated to be 1.98 eV. The wide bandgap and strong UV absorption in the region from 425 nm to 620 nm wavelength is optimal for pairing with most of the NFAs to form complementary UV absorption in OSCs.

Cyclic voltammetry was utilized to measure the HOMO and LUMO energy levels of TTOT. As shown in Table 2-1, the E_{HOMO} of TTOT is calculated to be -5.33 eV and is 0.27 eV higher than that of PBDTTO (E_{HOMO} = -5.60 eV). The rise in the HOMO energy level is mainly caused by the incorporation of the electron-donating thiophene spacers, which potentially might cause a decrease in the V_{OC} of OSC devices.

Table 2-1. Molecular weights, optical and electrochemical properties of TTOT.

Polymer	M_n (kDa)	M_w (kDa)	$Đ$	λ_{max} (nm)[a]	λ_{onset} (nm)[a]	E_g^{opt} (eV)	E_{HOMO} (eV)[b]	E_{LUMO} (eV)[c]
TTOT	132.8	144.5	1.75	539, 569	627	1.98	-5.33	-3.35

[a] Obtained from thin film absorption spectra; [b] obtained by $E_{HOMO} = -(4.80 + E_{onset}^{ox})$; [c] obtained by $E_{LUMO} = E_{HOMO} + E_g^{opt}$.

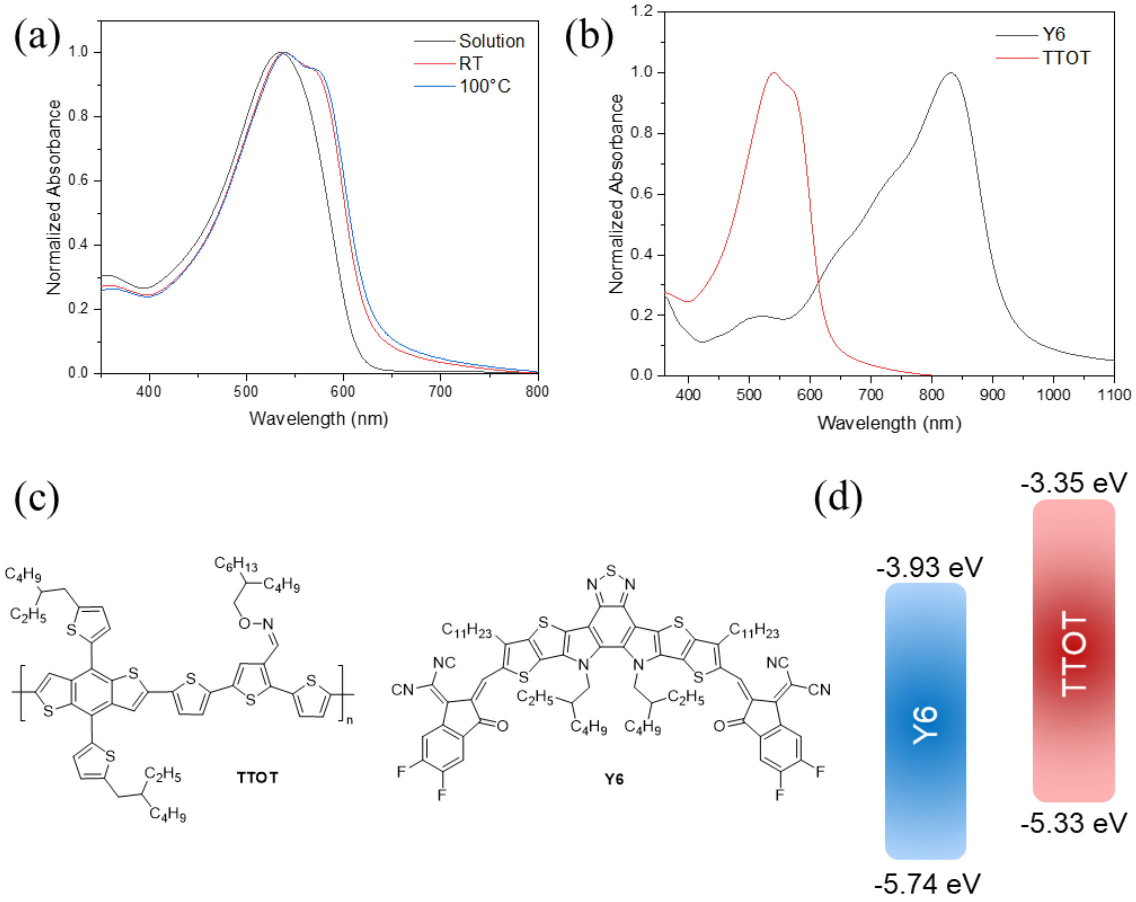

Figure 2-5. (a) Normalized UV-vis absorption spectra of TTOT in chloroform solution, in thin films at room temperature and anneal at 100°C, (b) normalized UV-vis absorption spectra of TTOT and Y6 in thin films, (c) chemical structures of TTOT and Y6, (d) frontier energy levels of TTOT and Y6 thin films.

2.5 Organic photovoltaic performances

The organic photovoltaic (OPV) performance of TTOT was evaluated by matching with a non-fullerene small molecular acceptor Y6 due to their suitable energy levels and complementary light absorption as shown in Figure 2-5 (b, d). The OSC devices were constructed using an inverted structure of ITO/ZnO/Active layer/MoO_3/Ag, where the active layer consists of the polymer donor TTOT and the NFA Y6.

Prior to device fabrication, the exciton diffusion and dissociation behaviour in the blend film was investigated through PL quenching experiments. As shown in Figure 2-6, TTOT:Y6 blend film showed excellent PL quenching efficiencies of 99.4% and 98.7% in the short and long wavelength region, respectively. The results showed that the size of the donor and acceptor phase in the blend film is smaller than the exciton diffusion length, and the exciton dissociation at the donor-acceptor interface is efficient as well.

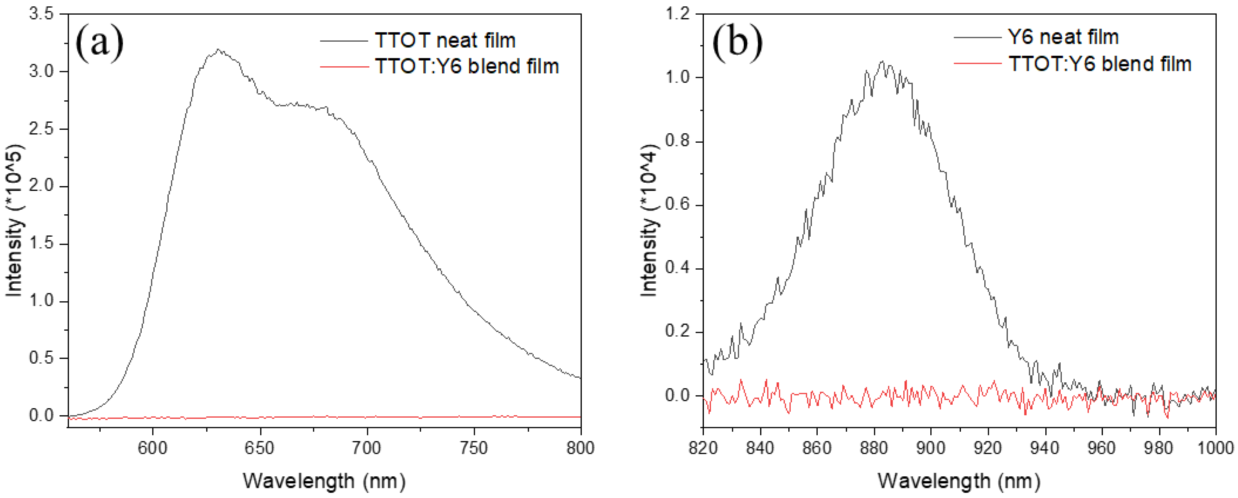

Figure 2-6. PL spectra of (a) TTOT neat and TTOT:Y6 blend films excited at 540 nm. (b) Y6 neat and TTOT:Y6 blend films excited at 800 nm.

The OSC device was then fabricated and serval parameters including the active layer thickness, thermal annealing, different processing solvents and different acceptors were optimized (Table 2-4, 2-5). The TTOT-based OSC performance results were summarized in Table 2-2.

Table 2-2. Photovoltaic results of the optimized TTOT-based OSC.

Temperature	Thickness	J_{SC} (mA/cm^2) [a]	V_{OC} (V) [a]	FF [a]	PCE (%) [a]
RT	**108 nm**	**23.58 (22.20 ± 1.22)**	**0.62 (0.62 ± 0.0059)**	**0.52 (0.51 ± 0.012)**	**7.65 (6.96 ± 0.66)**
RT	95 nm	21.56 (21.16 ± 1.03)	0.63 (0.62 ± 0.079)	0.55 (0.50 ± 0.032)	7.38 (6.68 ± 0.73)
100°C	95 nm	21.50 (21.51 ± 0.42)	0.59 (0.57 ± 0.012)	0.52 (0.50 ± 0.028)	6.61 (6.10 ± 0.40)

Processing solvent: chloroform, D/A ratio: 1:1, annealing time: 20 min.

[a] The values in parenthesis are average values and standard deviation obtained from at least four devices.

The as-cast TTOT-based device yielded a best PCE of 7.65% with a J_{SC} of 23.58 mA/cm^2, V_{OC} of 0.62 V and FF of 0.52. The J_{SC} value is comparable to that of the as-cast PBDTTO based device (23.53 mA/cm^2).[67] However, due to the higher E_{HOMO} (0.27 eV) of TTOT, V_{OC} of the OSC device was only 0.52 V, which is 0.31 V lower than that of the best PBDTTO based device. Furthermore, the FF is also low comparing to other NFA-based OSCs.[40,71,72,73] This low FF could be caused by the disordered or edge-on molecular packing of TTOT thin film and the unfavorable surface morphology TTOT:Y6 blend film. In addition, the unbalanced mobility ratio can also lead to a decrease in FF. At an annealing temperature of 100°C, the OSC device exhibited lower V_{OC} (0.63 to 0.59 V) and FF (0.55 to 0.52) than that of as-cast device. This result might be indicative of the more disordered and rougher surface of the active layer film after thermal annealing. As a result, SCLC mobility measurements, AFM and GIXD characterizations will be carried out to further explain the results.

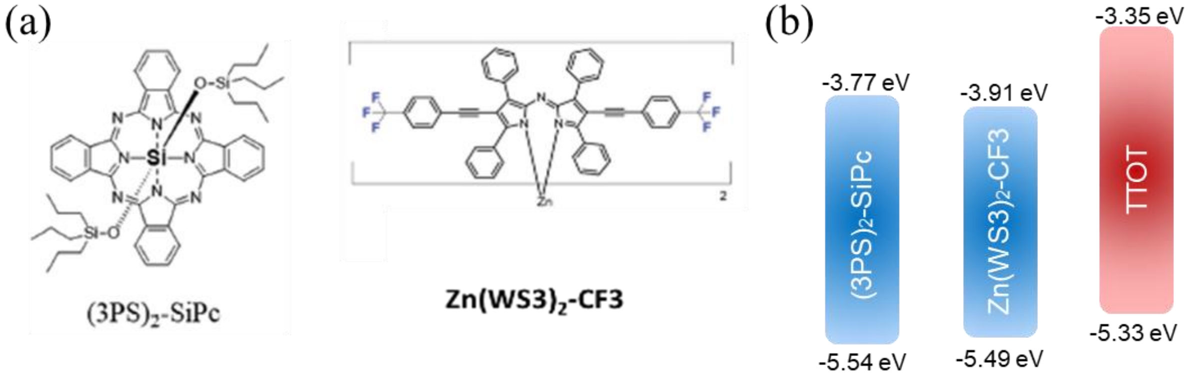

Figure 2-7. (a) Chemical structures of (3PS)$_2$-SiPc and Zn(WS3)$_2$-CF3, (b) frontier energy levels of TTOT, (3PS)$_2$-SiPc and Zn(WS3)$_2$-CF3 thin films.

Before further investigations of TTOT:Y6 systems, two acceptors, namely (3PS)$_2$-SiPc and Zn(WS3)$_2$-CF, were chosen to match with TTOT to enhance V$_{OC}$ in OSCs. Both acceptors have low synthetic complexity and higher E$_{HOMO}$ than that of Y6, can effectively reducing the HOMO offset (0.41 eV to 0.21 and 0.16 eV) and energy loss in TTOT based devices.[74,75] The UV absorption spectra and PL quenching results were shown in Figure 2-19, 2-20 and 2-21. The device performances were summarized in Table 2-6 and Table 2-7. The best (3PS)$_2$-SiPc based device only reached a PCE of 0.38% with an extremely low J$_{SC}$ of 1.12 mA/cm^2, a V$_{OC}$ of 0.60 V and an FF of 0.48. While the best Zn(WS3)$_2$-CF3 based OSC had a slightly higher PCE of 1.74%, a V$_{OC}$ of 0.73 V and an FF of only 0.41. The low J$_{SC}$'s were mainly attributed to the narrow UV absorption range and poor quenching efficiencies. Although the V$_{OC}$ of TTOT: Zn(WS3)$_2$-CF3-based device improved from 0.62 V to 0.73 V, this came at the cost of reducing J$_{SC}$ significantly, resulting in much lower photovoltaic performance.

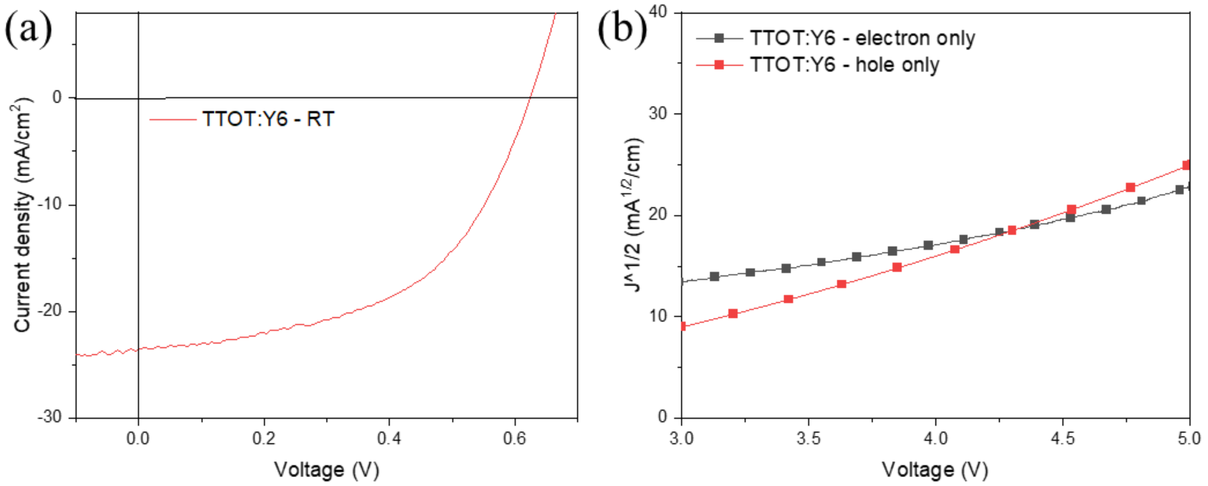

Figure 2-8. (a) J-V curve of the OSC device based on TTOT:Y6 blend film at room temperature, (b) $J^{1/2}$-V curves of hole-only and electron-only devices of TTOT:Y6 system.

SCLC mobility measurement was carried out to study the charge carrier mobilities of TTOT. As shown in Table 2-3, the hole mobility (μ_h) of the TTOT neat film at room temperature was measured to be 3.36×10^{-3} cm^{2}V^{-1}s^{-1}. This value is 16 times higher than that of PBDTTO (μ_h $=2.05 \times 10^{-4}$ cm^{2}V^{-1}s^{-1}), indicating the improved backbone planarity indeed facilitated charge carrier transfer.

For the TTOT:Y6 blend films, the measured SCLC μ_h and electron mobility (μ_e) are 2.84×10^{-4} cm^{2}V^{-1}s^{-1} and 3.22×10^{-5} cm^{2}V^{-1}s^{-1}, respectively. Compared to the mobilities of the neat TTOT and Y6 films (μ_e = ~10^{-4}-10^{-3} cm^{2}V^{-1}s^{-1}),[48] the significantly decreased hole and electron mobilities in the blend compared to their neat films indicate that the phase separation in the TTOT:Y6 blend is not optimal. This could have been a result of the inability to form efficient hole and electron transport channels, resulting in lower solar cell performance. In addition, the highly unbalanced μ_h /μ_e ratio (8.82) will potentially lead to the buildup and recombination of charge carriers, resulting in a decrease in the J_{SC} and FF.

Table 2-3. SCLC mobilities of TTOT neat films and blend films at room temperature.

Neat film / Blend film	$\mu_{h,max}$ ($\mu_{h,avg}$ ± std) ($cm^2\ V^{-1}\ S^{-1}$) [a]	$\mu_{e,max}$ ($\mu_{e,avg}$ ± std) ($cm^2\ V^{-1}\ S^{-1}$) [a]	μ_h / μ_e
TTOT - RT	3.36×10^{-3} ($2.24\times10^{-3}\pm6.47\times10^{-4}$)	-	-
TTOT:Y6 - RT	2.84×10^{-4} ($2.52\times10^{-4}\pm1.80\times10^{-5}$)	3.22×10^{-5}($1.70\times10^{-5}\pm1.05\times10^{-5}$)	8.82

[a] Above values are obtained from at least four devices.

The surface morphology of the active layer was examined through AFM and the molecular packing of polymer donor and blend film was studied by XRD measurements.

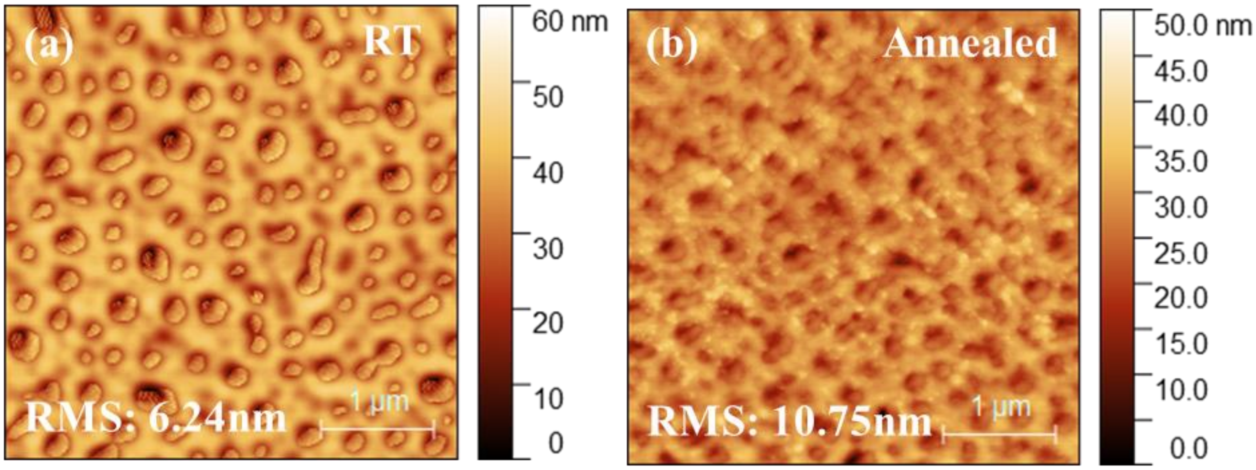

Figure 2-9. AFM height images of TTOT:Y6 blend film (a) at room temperature and (b) annealed at 100°C.

As shown in Figure 2-9, the root mean square (RMS) roughness reached 6.24 nm and large pinholes were observed in the TTOT:Y6 blend film at room temperature. The coarse film morphology would result in a poor interface between the active layer and the hole transport layer (MoO_3), leading to lower hole collection efficiency and recombination at the interface. Furthermore, the TTOT:Y6 blend film showed an even higher RMS value of 10.75 nm at an annealing temperature of 100°C. The largely increased surface roughness explained the decreased V_{OC} and PCE of the OSC device after thermal annealing.

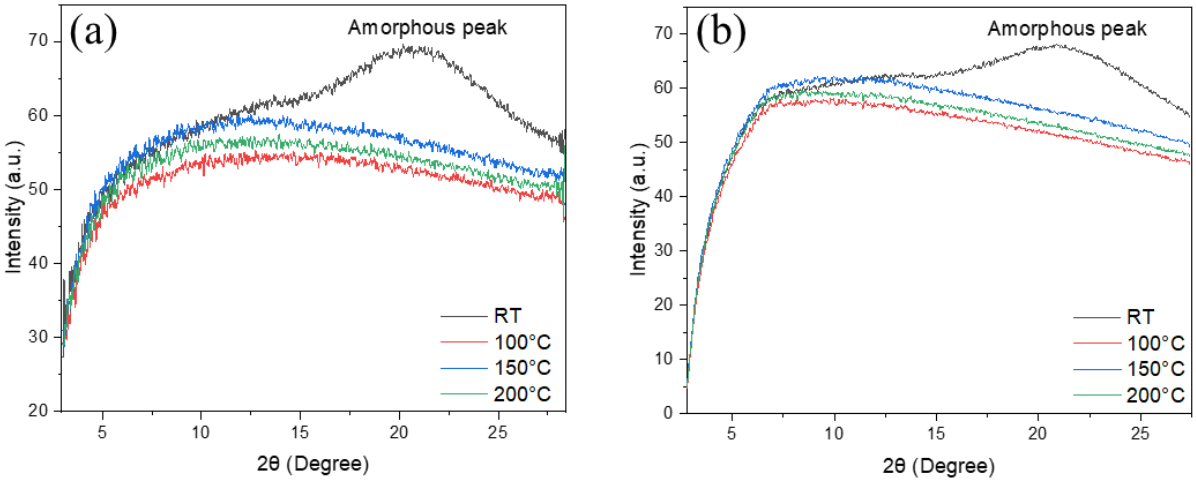

Figure 2-10. In-plane (a) and out-of-plane (b) line cuts of GIXD patterns of TTOT neat films at different annealing temperatures.

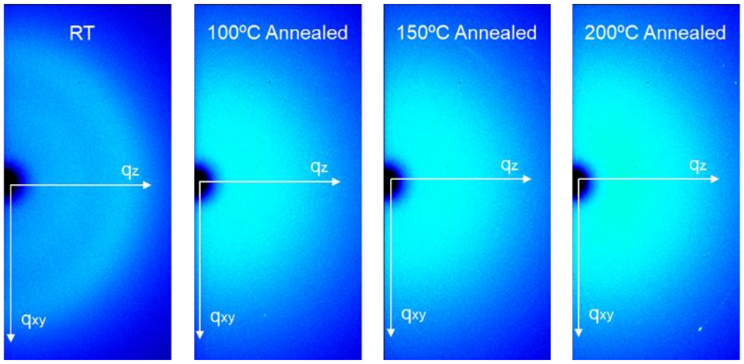

Figure 2-11. 2D-GIXD patterns of the TTOT neat films at different annealing temperatures.

As shown in Figure 2-10 and 2-11, the amorphous peak (2θ = ~21°) of the as-spun TTOT neat film (room temperature) in both in-plane and out-of-plane line cuts disappeared when annealed at 100°C or higher, which indicates that the film became less amorphous. However, no lamellar or π- π stacking peaks were observed for all annealing temperatures in both directions, which suggests that the annealed TTOT thin films remained poorly crystalline.

2.6 Conclusions and future directions

In conclusion, to further improve backbone planarity of BDT-TO-based polymer donors, a new wide conjugated bandgap polymer TTOT was designed with the incorporation of thiophene spacers for non-fullerene OSCs. It indeed showed a significantly enhanced SCLC hole mobility of up to 3.36×10^{-3} $cm^2V^{-1}s^{-1}$. However, due to the utilization of the electron-donating thiophene spacers, TTOT has a high E_{HOMO} of -5.33 eV. Furthermore, TTOT showed strong light absorption in the range from 425 to 620 nm wavelength region with a wide optical bandgap of 1.98 eV, which makes its UV absorption complementary to most of the NFAs. By pairing with the non-fullerene acceptor Y6, the best device showed a PCE of 7.65% with a J_{SC} of 23.58 mA/cm^2, relatively low V_{OC} of 0.62 V and FF of 0.52. A large energy loss was revealed in the TTOT:Y6 based device, which is due to the large E_{HOMO} offset of the donor and acceptor materials. To further enhance the OSC performance, halogenation strategies such as fluorination or chlorination can be employed to downshift the E_{HOMO} of TTOT. As a result, the energy loss can be reduced to achieve a higher V_{OC} and PCE in OSCs.

2.7 Experimental section

Synthesis of (Z)-2,5-Dibromothiophene-3-carbaldehyde O-(2-butyloctyl) oxime (2)[76]

K_2CO_3 (1.21 g, 8.77 mmol) was added to a mixture of 2-butyloctyl bromide (1.09 g, 4.39 mmol) and compound 2 (1.51 g, 5.26 mmol) in DMF (25mL). After 48 h stirring at room temperature, the mixture was quenched with $NaHCO_3$ and extracted with dichloromethane. Then the organic phase was washed with $NaHCO_3$ solution and dried over anhydrous Na_2SO_4. The crude product was purified through column chromatography using hexane as eluent, and the pure product appeared as transparent oil after vacuo. Yield: 1.27g. (64%) ^1H NMR (300 MHz, $CDCl_3$): δ (ppm) 8.02 (d, 1H), 7.30 (t, 1H), 4.06-4.03 (m, 2H), 1.71 (s, 1H), 1.31 (s, 16H), 0.90 (t, 6H). ^{13}C

NMR (75 MHz, CDCl3): δ (ppm) 141.23, 134.41, 127.88, 112.85, 112.29, 77.97, 37.73, 31.89, 31.22, 30.92, 29.72, 28.98, 26.71, 23.09, 22.71, 14.13.

Synthesis of (Z)-[2,2':5',2''-terthiophene]-3'-carbaldehyde O-(2-butyloctyl) oxime (3)[77]

Anhydrous DMF (15 mL) was injected through a septum to a 50 ml round bottom flask charged with compound 2 (0.57 g, 1.26 mmol) and 2-(Tributylstannyl) thiophene (1.17 g, 3.14mmol). Then tetrakis(triphenylphosphine)palladium (14.53 mg, 12.53 umol) was added in dry DMF through syringe. The mixture was heated to 100°C under argon in dark for 24 h. KF solution was added, and the crude product was extracted with dichloromethane, washed with $NaHCO_3$, and dried over anhydrous Na_2SO_4. Purification was done by column chromatography using dichloromethane and hexane (1:4) as the eluent. Pure product was obtained after vacuo as yellow oil. Yield: 0.47g. (81%) ^{1}H NMR (300 MHz, CDCl3): δ (ppm) 8.29 (s, 1H), 7.51 (s, 1H), 7.40-7.38 (m, 1H), 7.27-7.25 (m, 1H), 7.22-7.21 (m, 1H), 7.16-7.15 (m, 1H), 7.10-7.19 (m, 1H), 7.05-7.02 (m, 1H), 4.09 (d, 2H), 1.73 (t, 1H), 1.33-1.29 (t, 16H), 0.91-0.86 (t, 6H). ^{13}C NMR (75 MHz, CDCl3): δ (ppm) 142.75, 136.60, 136.36, 134.80, 133.72, 131.07, 127.87, 127.54, 126.99, 125.16, 124.34, 122.03, 77.67, 37.74, 31.88, 31.26, 30.96, 29.72, 28.97, 26.71, 23.10, 22.69, 14.04.

Synthesis of (Z)-5,5''-dimethyl-[2,2':5',2''-terthiophene]-3'-carbaldehyde O-(2-butyloctyl) oxime (4)[55]

Compound 3 (400 mg, 0.87 mmol) and N-bromosuccinimide (NBS) (317.5 mg, 1.78 mmol) was added into DMF (10 mL). The mixture was stirred at room temperature for 24 h, water was added into the mixture. Then the product was extracted with dichloromethane, and the organic layer was washed with NaHCO3 and water. The pure product appeared as brown oil without further purification. Yield: 0.523g. (98%) ^{1}H NMR (300 MHz, CDCl3): δ (ppm) 8.21 (s, 1H), 7.90 (s, 1H), 7.42 (s, 1H), 7.06 (d, 1H), 6.98 (d, 1H), 6.95 (d, 1H), 6.90 (d, 1H), 4.16 (d, 2H), 4.08 (d, 2H), 1.74 (s, 1H), 1.32 (d, 16H), 0.91 (d, 6H). ^{13}C NMR (75 MHz, CDCl3): δ (ppm) 142.08, 135.93, 133.61, 130.71, 127.88, 124.58, 122.35, 113.94, 112.11, 77.85, 37.76, 31.90, 31.25, 30.95, 29.74, 28.98, 26.72, 23.11, 22.71, 14.15.

Synthesis of TTOT

To a dried 25ml 2-necked round bottom flask, added tris(o-tolyl)phosphine ($P(o\text{-}tol)_3$) (0.08 equiv.), compound 4 (1 equiv.) and 1,1′-[4,8-Bis[5-(2-ethylhexyl)-2-thienyl]benzo[1,2-b:4,5-b′]dithiophene-2,6-diyl]bis[1,1,1-trimethylstannane] (BDT) (1 equiv.). Followed by adding 4ml anhydrous chlorobenzene and stirring the mixture until dissolved. Then tris-(dibenzylideneacetone)dipalladium ($Pd_2(dba)_3$) (0.02 equiv.) was injected through septum in anhydrous chlorobenzene to the stirring mixture. After 24 h reaction at 90°C under dark and argon atmosphere, 0.5 ml 2-bromobenzene was added. After cooling to room temperature, the mixture was poured into 150 ml methanol. The solid was collected by filtration, purified through Soxhlet extraction using acetone, hexane, and chloroform. The target polymer TTOT was obtained from chloroform fraction, the yield was 88.3mg (88%).

OSC device fabrication

The OSC devices were fabricated using an inverted structure of ITO/ZnO (40 nm)/Active layer/MoO3 (10 nm)/Ag (100 nm). The ITO glass substrate was emersed and ultrasonicated in deionized water, HPLC acetone and HPLC iso-propanol for 20 minutes. The ZnO precursor solution was prepared by mixing 197 mg zinc acetate, 54 µl ethanolamine and 2 ml 2-methoxyethanol at room temperature overnight. Then the solution was filtered with 0.22 µm

PTFE filter before use. A 40-nm thick ZnO was spin coated onto 10 min O_2 plasma cleaned ITO glass substrate at a spin rate of 3500 rpm for 60 s, followed by annealing at 200°C for one hour in the air. The active layer was prepared by stirring a mixture of donor and acceptor material (D/A ratio=1:1) at a concentration of 20 mg/ml overnight in the glovebox. At a spin rate of 4000 rpm, TTOT:Y6 (108 nm) was coated onto the substrate in glove box after filtering with 0.22 μm PTFE filter. The device was then transferred to the thermal evaporator and vacuumed until the chamber pressure is below 1×10^{-6} torr. The MoO_3 layer (10 nm) was coated at a deposition rate of 0.5 Å/s, and the Ag layer (100 nm) was coated at a deposition rate of 1 Å/s. Each device has an area of 0.0574 cm^2. An Agilent B2912A Semiconductor Analyzer equipped with a Science Tech SLB300-A Solar Simulator was used to measure the current density-voltage (J-V) curve, and the light source came from a 450 W xenon lamp and an air mass (AM 1.5G) filter.

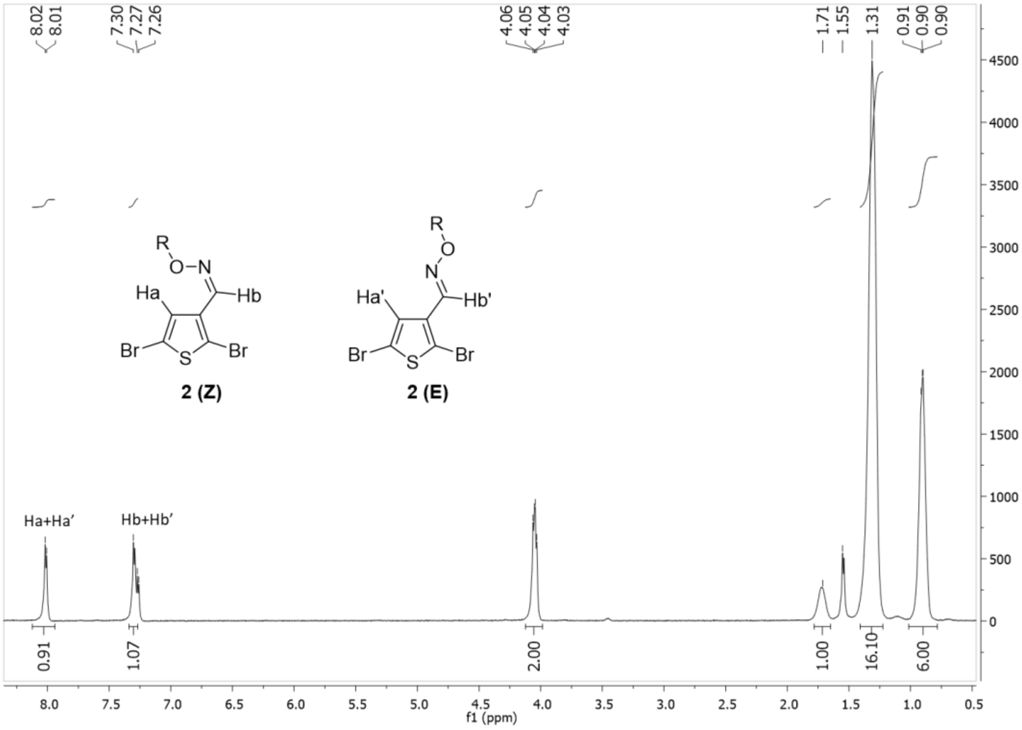

Figure 2-12. ^{1}H NMR spectra of compound **2**.

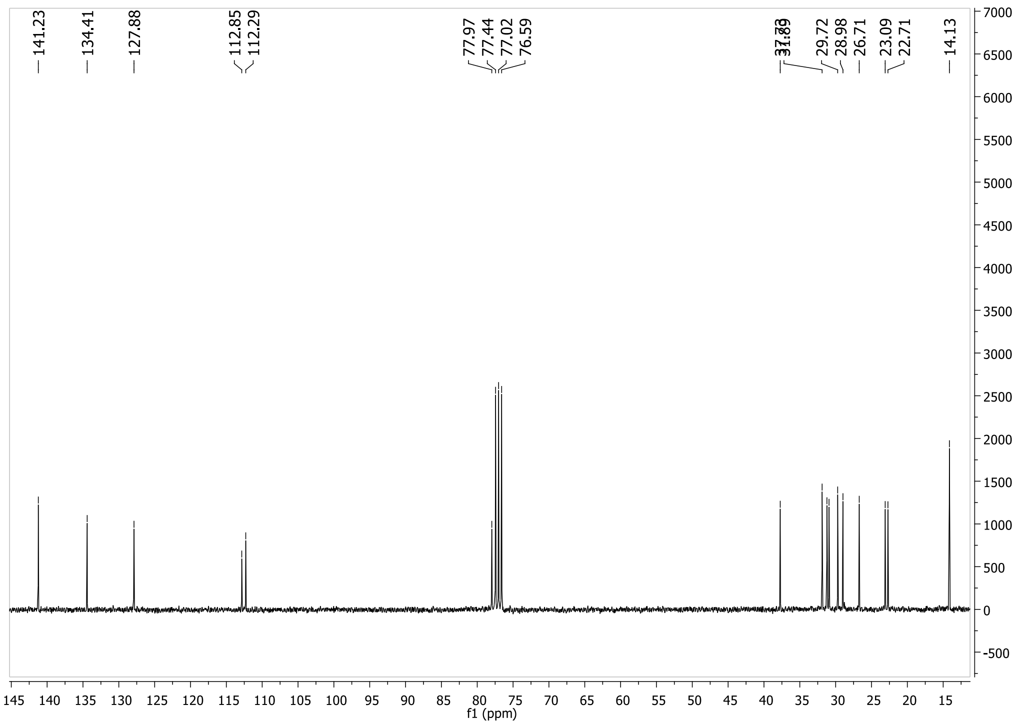

Figure 2-13. ^{13}C NMR spectra of compound **2**.

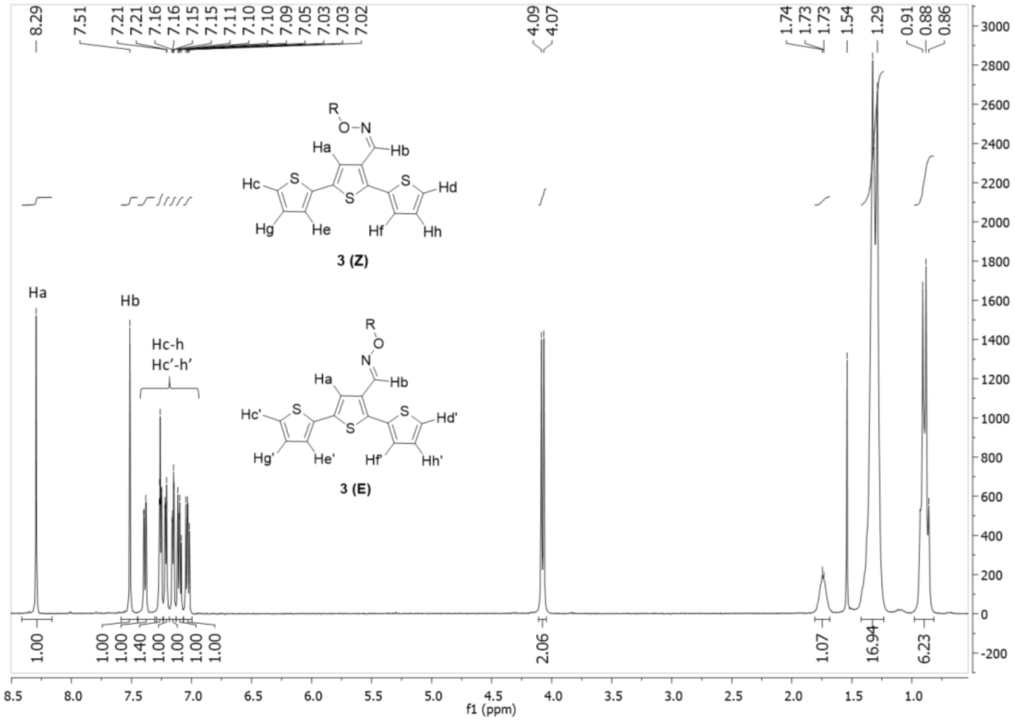

Figure 2-14. ^{1}H NMR spectra of compound **3**.

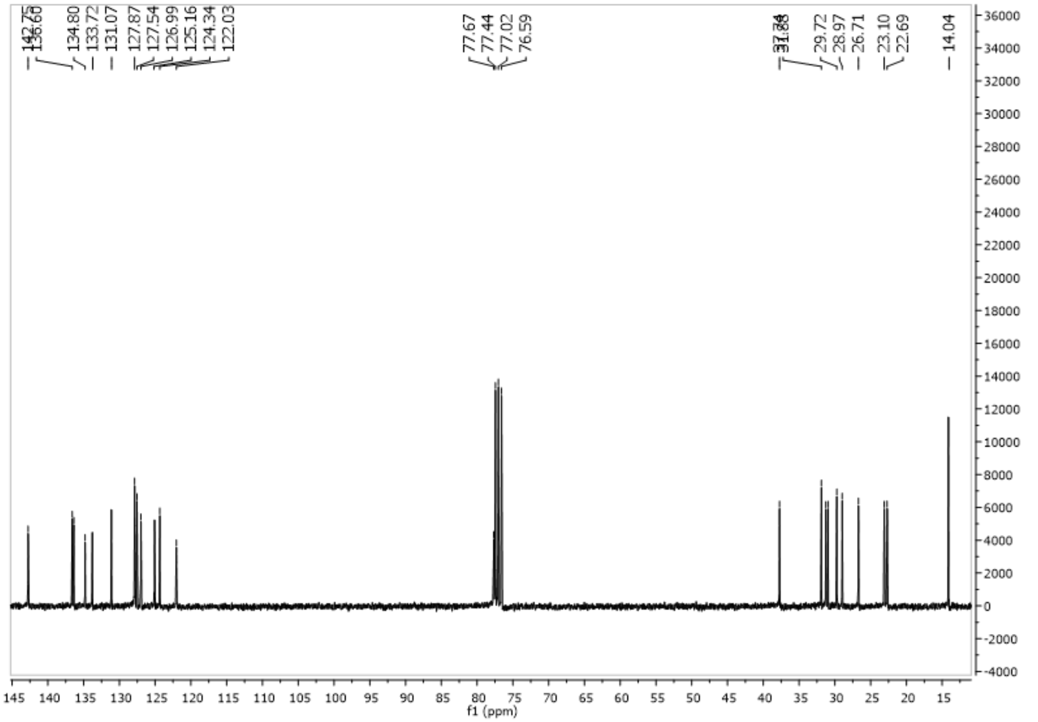

Figure 2-15. ^{13}C NMR spectra of compound **3**.

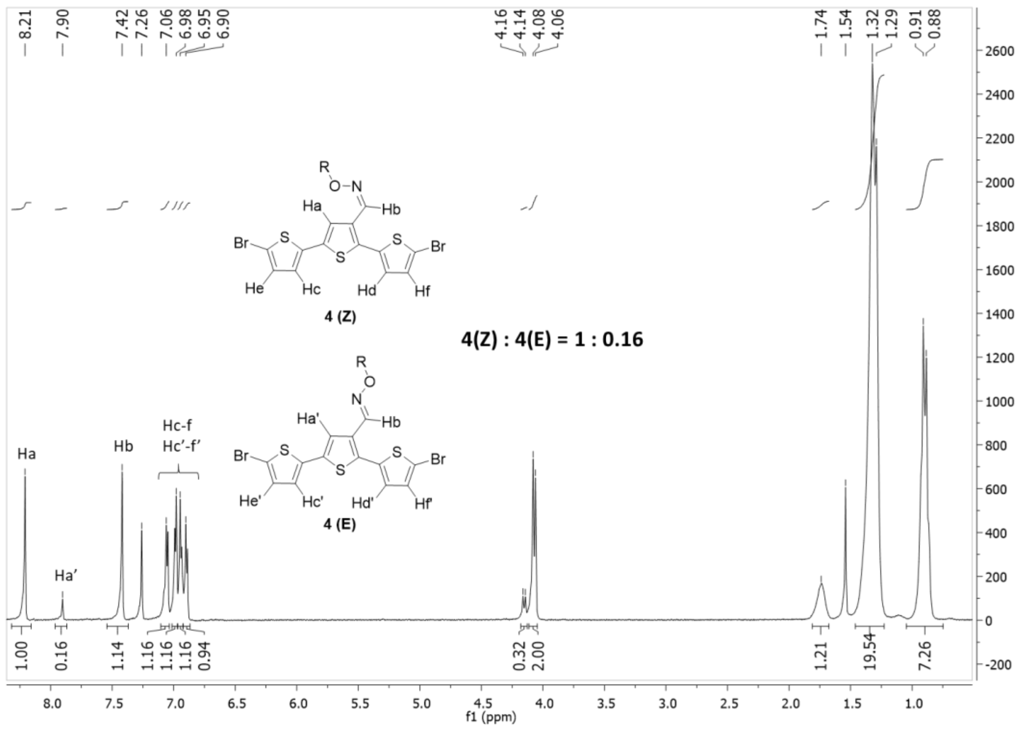

Figure 2-16. ^{1}H NMR spectra of compound **4**.

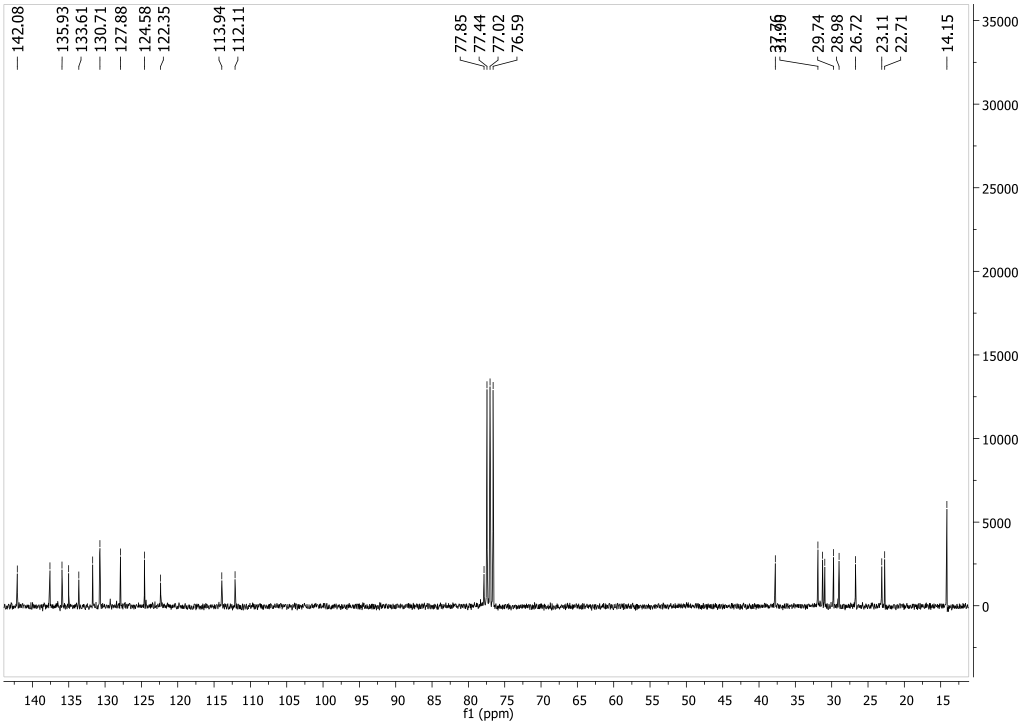

Figure 2-17. ^{13}C NMR spectra of compound **4**.

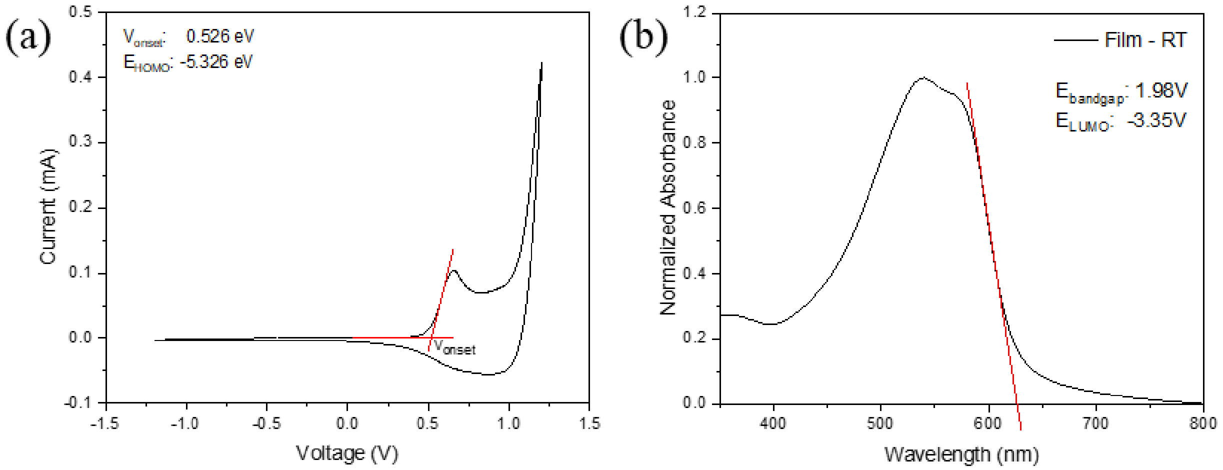

Figure 2-18. (a) Cyclic voltammograms of TTOT thin film. (b) UV-vis absorption spectra of TTOT thin film at room temperature.

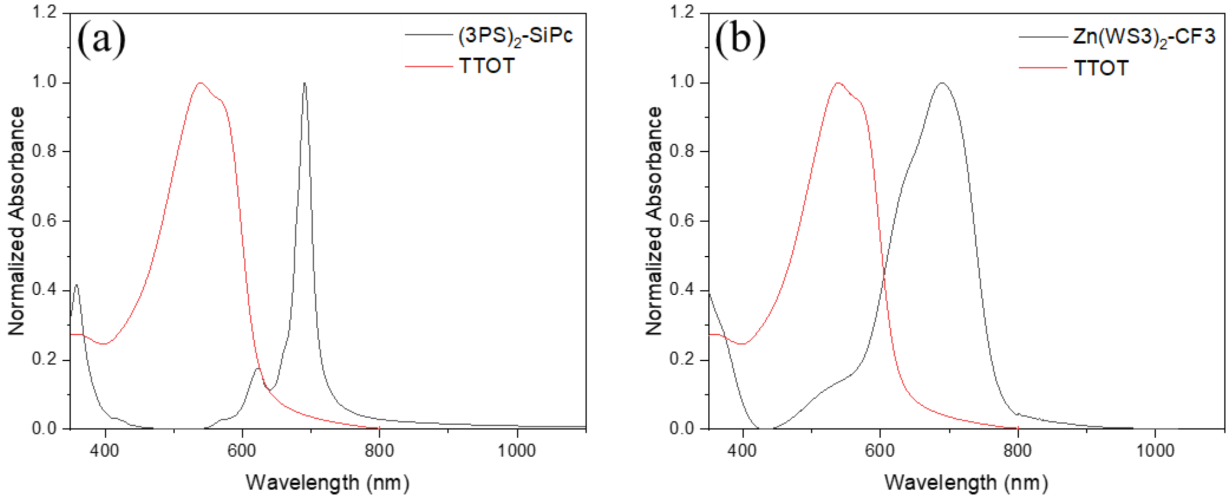

Figure 2-19. UV-vis absorption spectra of TTOT and (a) (3PS)$_2$-SiPc and (b) Zn(WS3)$_2$-CF3 thin films at room temperature.

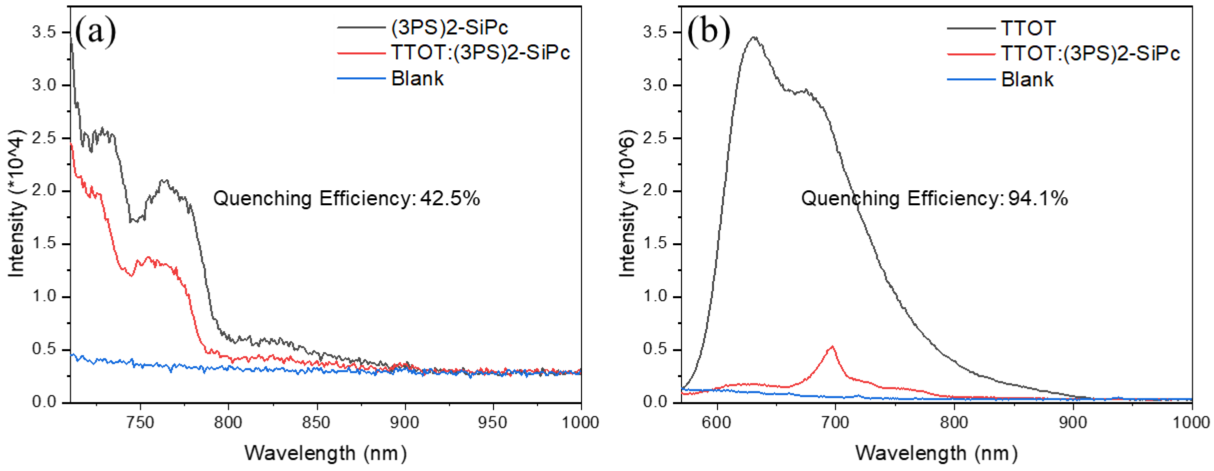

Figure 2-20. PL spectra of (a) TTOT neat and TTOT:(3PS)$_2$-SiPc blend films excited at 550 nm. (b) (3PS)$_2$-SiPc neat and TTOT:(3PS)$_2$-SiPc blend films excited at 690 nm.

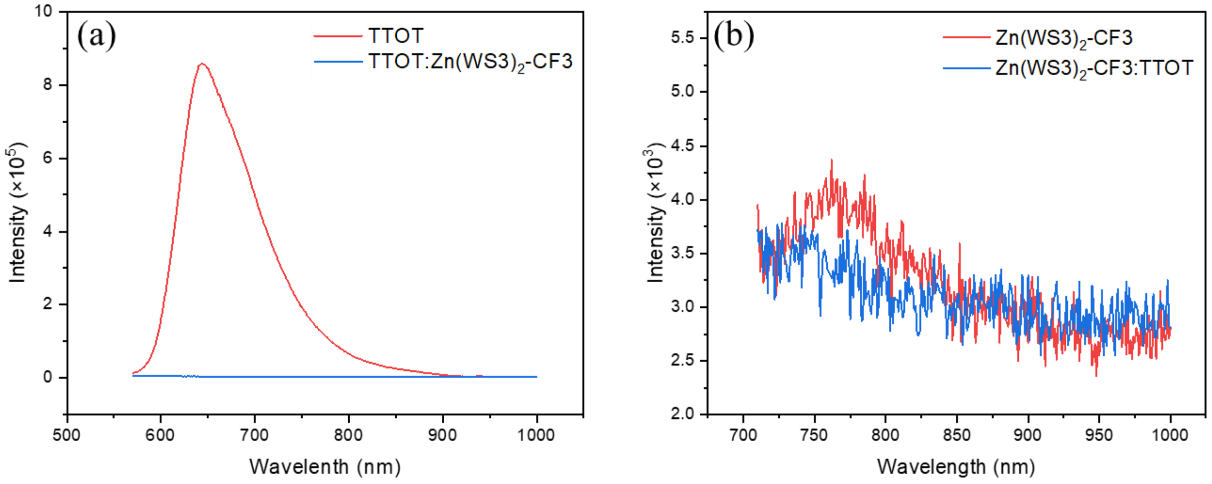

Figure 2-21. PL spectra of (a) TTOT neat and TTOT:Zn(WS3)$_2$-CF3 blend films excited at 550 nm. (b) Zn(WS3)$_2$-CF3 neat and TTOT:Zn(WS3)$_2$-CF3 blend films excited at 690 nm.

Table 2-4. Performance optimization of TTOT:Y6 based devices with different active layer film thickness and annealing temperature.

Temperature	Thickness	J_{SC} (mA/cm^2) [a]	V_{OC} (V) [a]	FF [a]	PCE (%) [a]
RT	205 nm	18.06 (18.30 ± 0.34)	0.65 (0.65 ± 0.0011)	0.40 (0.40 ± 0.0086)	4.75 (4.73 ± 0.01)
RT	180 nm	20.57(19.20 ± 1.07)	0.66(0.65 ± 0.0058)	0.44 (0.44 ± 0.0043)	6.00 (5.52 ± 0.38)
RT	165 nm	20.23(19.13 ± 1.04)	0.67(0.66 ± 0.0065)	0.47 (0.47 ± 0.020)	6.35 (5.86 ± 0.51)
RT	115 nm	24.19 (21.50 ± 2.35)	0.63 (0.62 ± 0.012)	0.49 (0.47 ± 0.019)	7.49 (6.33 ± 1.04)
RT	**108 nm**	**23.58 (22.20 ± 1.22)**	**0.62 (0.62 ± 0.0059)**	**0.52 (0.51 ± 0.012)**	**7.65 (6.96 ± 0.66)**
RT	100 nm	21.34 (21.03 ± 0.70)	0.63 (0.63 ± 0.0045)	0.54 (0.52 ± 0.025)	7.29 (6.84 ± 0.51)
RT	95 nm	21.56 (21.16 ± 1.03)	0.63 (0.62 ± 0.079)	0.55 (0.50 ± 0.032)	7.38 (6.68 ± 0.73)
100°C	95 nm	21.50 (21.51 ± 0.42)	0.59 (0.57 ± 0.012)	0.52 (0.50 ± 0.028)	6.61 (6.10 ± 0.40)

Processing solvent: chloroform, D/A ratio: 1:1, annealing time: 20min.

[a] The values in parenthesis are average values and standard deviation obtained from at least four devices.

Table 2-5. Performance optimization of TTOT:Y6 based devices with different processing solvents.

Processing Solvent	Thickness	J_{SC} (mA/cm^2) [a]	V_{OC} (V) [a]	FF [a]	PCE (%) [a]
Chlorobenzene	125 nm	17.14 (16.78 ± 0.32)	0.58 (0.58 ± 0.0046)	0.55 (0.55 ± 0.006)	5.37 (5.32 ± 0.06)
Chlorobenzene	105 nm	17.03 (16.55 ± 0.58)	0.57 (0.57 ± 0.0025)	0.59 (0.58 ± 0.013)	5.77 (5.48 ± 0.27)
Chlorobenzene	80 nm	16.84 (16.22 ± 0.70)	0.59 (0.59 ± 0.0001)	0.55 (0.56 ± 0.010)	5.46 (5.28 ± 0.17)
Dichlorobenzene	72 nm	10.88 (10.6 ± 0.64)	0.57 (0.57 ± 0.012)	0.58 (0.57 ± 0.006)	3.61 (3.38 ± 0.27)
Dichlorobenzene	68 nm	10.55 (9.62 ± 0.74)	0.58 (0.57 ± 0.0076)	0.58 (0.57 ± 0.005)	3.54 (3.16 ± 0.31)

Processing temperature: RT, D/A ratio: 1:1.

[a] The values in parenthesis are average values and standard deviation obtained from at least four devices.

Table 2-6. Performance optimization of TTOT:$(3PS)_2$-SiPc based devices with different active layer film thickness and annealing temperature.

Temperature	Thickness (nm)	J_{SC} (mA/cm^2)	V_{OC} (V)	FF	PCE (%)
RT	135	1.3	0.68	0.35	0.31
RT	130	1.05	0.64	0.29	0.19
RT	120	1.16	0.63	0.34	0.25
RT	100	1.42	0.67	0.33	0.31
100°C-20min	130	1.12	0.60	0.48	0.38

D/A ratio: 1:1; Solvent: chloroform; Active layer concentration: 16mg/ml.

Table 2-7. Performance optimization of TTOT:Zn(WS3)$_2$-CF3 based devices with different active layer film thickness.

Temperature	Thickness (nm)	J_{SC} (mA/cm^2)	V_{OC} (V)	FF	PCE (%)
RT	120	4.89	0.71	0.37	1.28
RT	115	5.88	0.73	0.41	1.74

D/A ratio: 1:1; Solvent: chloroform; Active layer concentration: 16mg/ml.

Table 2-8. Dielectric constant and other related parameters of TTOT neat and blend films.

Neat film / Blend film	C_g (pF) [a]	f (Hz)	ε_r [a]
TTOT - RT	936	5×10^5	3.50
TTOT:Y6 – RT	1396	5×10^5	4.95

[a] Above values are obtained from at least five devices.

Chapter 3 Synthesis and characterization of TTOTF and TTOTCl polymers

3.1 Introduction

In Chapter 2, a new wide bandgap conjugated polymer donor TTOT was designed and synthesized. Due to the incorporation of the π-spacers, the polymer backbone planarity was enhanced and showed a high neat film hole mobility of 3.36×10^{-3} $cm^2V^{-1}s^{-1}$. However, the OSC device performance was relatively low, mainly attributed to the low V_{OC} caused by large E_{HOMO} offset. Halogenation strategies such as fluorination or chlorination can be employed to effectively downshift the E_{HOMO} of TTOT, resulting in better compatibility with NFAs and V_{OC} in the OSCs.[34,53,54] Therefore, we used a fluorine-substituted and a chlorine-substituted BDT monomer to synthesize two new polymers poly{(Z)-5''-(4,8-bis(4-fluoro-5-(2-ethylhexyl)thiophen-2-yl)-6-methylbenzo[1,2-b:4,5-b']dithiophen-2-yl)-5-methyl-[2,2':5',2''-terthiophene]-3'-carbaldehyde O-(2-butyloctyl) oxime}(TTOTF) and poly{(Z)-5''-(4,8-bis(4-chloro-5-(2-ethylhexyl)thiophen-2-yl)-6-methylbenzo[1,2-b:4,5-b']dithiophen-2-yl)-5-methyl-[2,2':5',2''-terthiophene]-3'-carbaldehyde O-(2-butyloctyl) oxime}(TTOTCl), respectively.

Both polymers have wide optical bandgap of over 1.97 eV and strong light absorption from the 425 to 620 nm wavelength region. TTOTF (E_{HOMO} = -5.46 eV) has a 0.13 eV lower-lying E_{HOMO} than that of TTOT, while TTOTCl further brings down the E_{HOMO} to -5.48 eV. To investigate the OSC device performance of these two polymers, Y6 was then chosen as the acceptor. The best TTOTF-based OSC device showed good device performance with a J_{SC} of 27.61 mA/cm^2, significantly improved V_{OC} of 0.72 V and FF of 0.69, resulting in an almost two-fold higher PCE of 13.57% when comparing to TTOT-based OSCs. Furthermore, the optimized TTOTCl-based OSC device showed an even higher PCE of 14.91%, with a Voc of 0.70 eV, a FF of 0.68 and a record-high J_{SC} of 31.03 mA/cm^2 among non-fullerene OSCs.[38,9,45] The largely increased FF and

J_{SC} are the results of the considerably improved SCLC hole mobilities of TTOTF and TTOTCl in OSCs. In addition, with the incorporation of the LiTFSI as a hole transport enhancement layer, the performance of the best TTOTCl-based OSC achieved an excellent PCE of 15.96%, with an enhanced V_{OC} of 0.72 V and FF of 0.71. The optimized TTOTF and TTOTCl-based OSC devices demonstrated excellent long-term stability without encapsulation under ambient condition. The TTOTCl-based OSC retained 90.4 % PCE of its initial value over a 30-day period, and both systems had almost 80% PCE retention after a 60-day period. This work demonstrates the potential of the TO-based polymer donor TTOTCl for the fabrication of highly efficient and stable OSCs.

3.2 Structure simulation by density functional theory

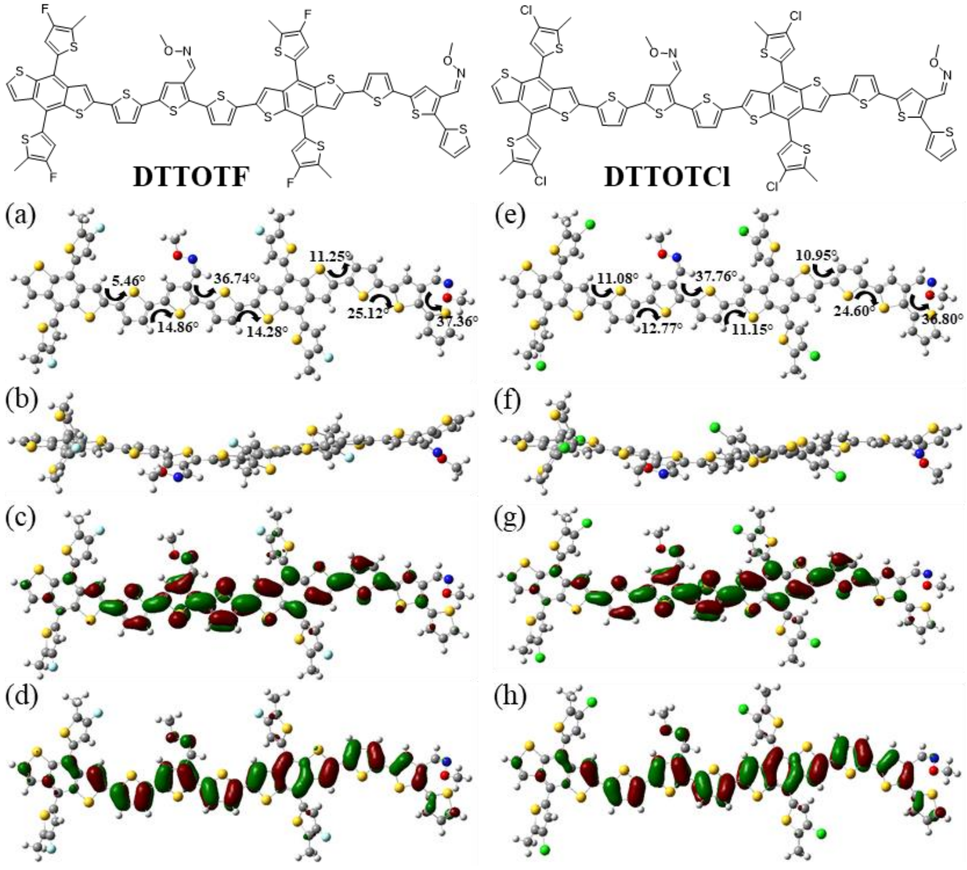

Figure 3-1. Chemical structures, top and side views of DFT computed molecular geometry, LUMOs, and HOMOs of compound DTTOTF (a, b, c, d) and DTTOTCl (c, f, g, h).

The DFT calculations were carried out by Gaussian 09 with a hybrid B3LYP correlation function and 6-31G (d) basis set. The simulation was conducted on the dimer units of TTOTF and TTOTCl, namely, DTTOTF and DTTOTCl. The influence of the incorporation of the fluorine and chlorine atom was investigated, where the 2-ethylhexyl side chains on BDT unit and the 2-butyloctyl side chain on the TO unit were replaced by methyl groups to reduce computation time.

According to DFT results (Figure 3-1), the dihedral angle of DTTOTF and DTTOTCl were 36.74° and 37.76°, respectively. The simulated E_{HOMO}'s of DTTOTF and DTTOTCl are -4.969 eV and -4.999 eV, respectively, which is 0.107 eV and 0.137 eV lower than that of DTTOT. These computational results clearly showed that the replacement of hydrogen with fluorine and chlorine atoms did not affect the backbone planarity but could effectively reduce the HOMO energy level. Further confirmations will be illustrated through experimental results.

3.3 Synthesis of TTOTF and TTOTCl

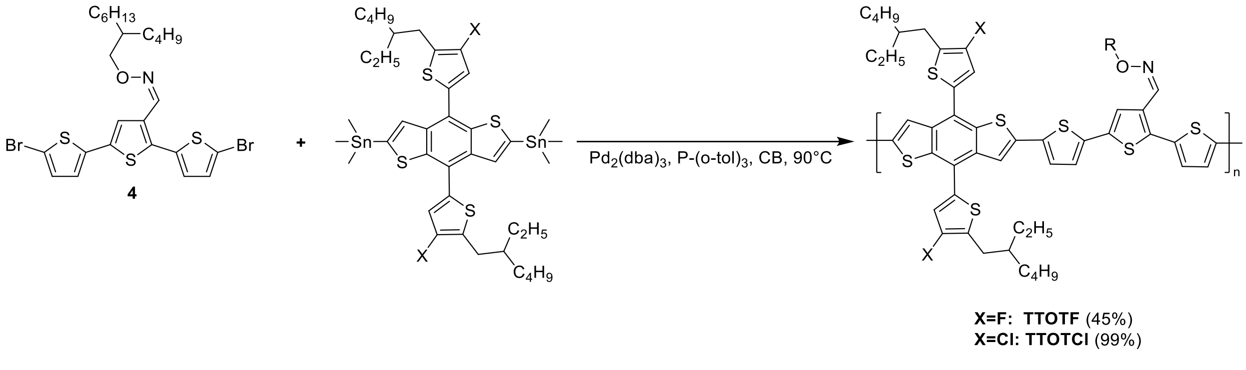

Figure 3-2. Synthetic routes of TTOTF and TTOTCl.

The synthetic routes of TTOTF and TTOTCl polymers are shown in Figure 3-2. The monomer compound **4** was prepared as reported in Chapter 2. Then TTOTF and TTOTCl polymers were synthesized under a typical Stille cross coupling condition using 2,6-bis(trimethytin)-4,8-bis(5-(2-ethylhexyl)-4-fluorothiophen-2-yl)benzo[1,2-b:4,5-b']dithiophene (BDTTDFSn) and 2,6-bis(trimethytin)-4,8-bis(5-(2-ethylhexyl)-4-chlorothiophen-2-yl)benzo[1,2-b:4,5-b']dithiophene (BDTTDClSn) as comonomers, respectively. Both polymers showed good solubility in chloroform and chlorobenzene.

3.4 Characterization of TTOTF and TTOTCl

3.4.1 Thermal properties

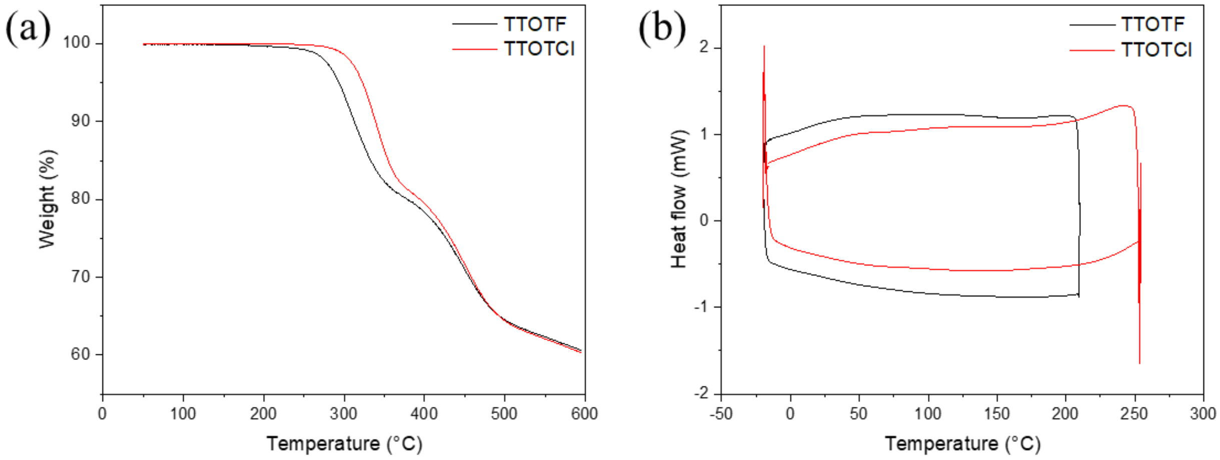

Figure 3-3. (a) TGA and (b) DSC curves of TTOTF and TTOTCl.

Thermal properties of TTOTF and TTOTCl were studied by TGA and DSC. As shown in Figure 3-3 (a), TTOTF polymer showed a 1% and 5% weight loss at temperature of 258°C and 292°C. While TTOTCl showed a 1% and 5% weight loss at 269°C and 323°C, respectively, indicating a lightly better thermal stability of TTOTCl. DSC results are shown in Figure 3-3(b), where no obvious phase transition peaks were observed, which is indicative of poor crystallinity and suggests that the melting points are higher than the decomposition temperatures for both polymers.

3.4.2 Optical and electrochemical properties

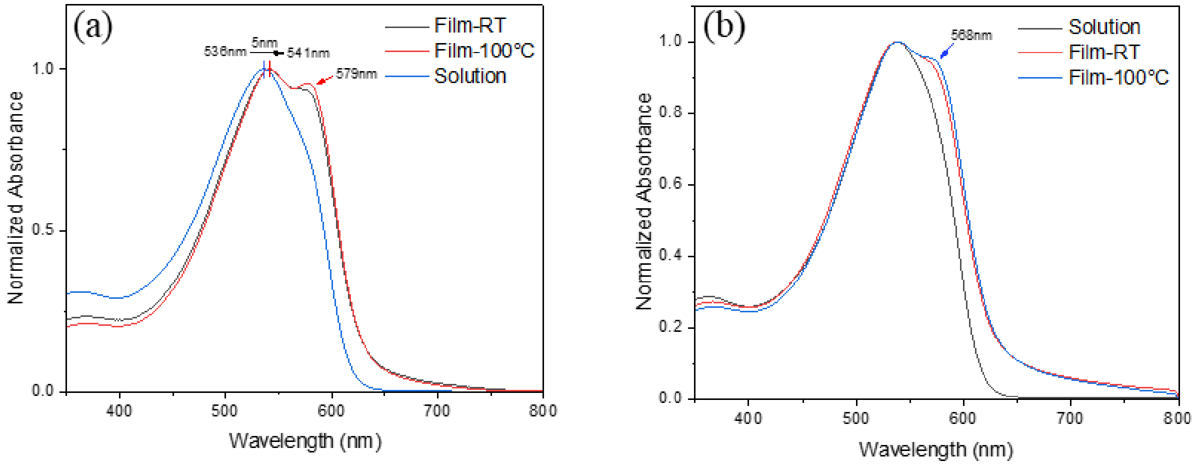

Figure 3-4. Normalized UV-vis absorption spectra of (a) TTOTF and (b) TTOTCl in chloroform solutions, in thin films at room temperature and annealing at 100°C.

The optical properties of TTOTF and TTOTCl were investigated by UV-Vis spectroscopy. Figure 3-4 (a) shows the absorption spectrum of TTOTF in chloroform solution, in thin films without annealing and annealing at 100°C. In chloroform solution, TTOTF has a λ_{max} located at 536 nm and a weak pre-aggregation behaviour was observed around 579 nm. The TTOTF thin film has a red-shifted maximum absorption peak at 541 nm and a shoulder peak at 579 nm, which is attributed to the π-π stacking of the polymer backbones. After annealing at 100°C, the shoulder peak was intensified, indicating a more ordered molecular packing of TTOTF after thermal annealing. As shown in Figure 3-4 (b), TTOTCl has a similar absorption profile in comparison to TTOTF. It had a maximum absorption peak at 538 nm and the vibronic absorption peak located at 568 nm was also intensified after thermal annealing. However, no pre-aggregation feature was observed in chloroform solution. The optical bandgaps of TTOTF and TTOTCl were calculated to be 1.98 eV and 1.97 eV, respectively. The wide bandgap and strong

UV absorption range from 425 nm to 620 nm is optimal for pairing with most NFAs to form complementary light absorption in OSCs.

Cyclic voltammetry was then employed to measure the HOMO and LUMO energy levels of TTOTF and TTOTCl. As shown in Table 3-1, the E_{HOMO} of TTOTF is calculated to be -5.46 eV and is 0.13 eV higher than that of TTOT (E_{HOMO} = -5.33 eV). Whereas TTOTCl has slightly deeper E_{HOMO} of -5.48 eV which is consistent with the DFT computed results. The introduction of the fluorine and chlorine atoms effectively lower the HOMO energy level of TTOT. As a result, lower energy loss and higher V_{OC} are expected in OSC devices.

Table 3-1. Molecular weights, optical and electrochemical properties of TTOTF and TTOTCl.

Polymer	M_n (kDa)	M_w (kDa)	$Đ$	λ_{max} (nm)[a]	λ_{onset} (nm)[a]	E_g^{opt} (eV)	E_{HOMO} (eV)[b]	E_{LUMO} (eV)[c]
TTOTF	20.8	56.2	2.71	541, 579	627	1.98	-5.46	-3.48
TTOTCl	43.0	109.9	2.56	538, 568	628	1.97	-5.48	-3.51

[a] Obtained from thin film absorption spectra; [b] obtained by $E_{HOMO} = -(4.80 + E_{onset}^{ox})$; [c] obtained by $E_{LUMO} = E_{HOMO} + E_g^{opt}$.

3.5 Organic photovoltaic performances

The OPV performance of TTOTF and TTOTCl were evaluated by matching with the non-fullerene acceptor Y6. Their molecular structures, frontier energy levels and normalized absorption spectra are shown in Figure 3-5 (a-c).

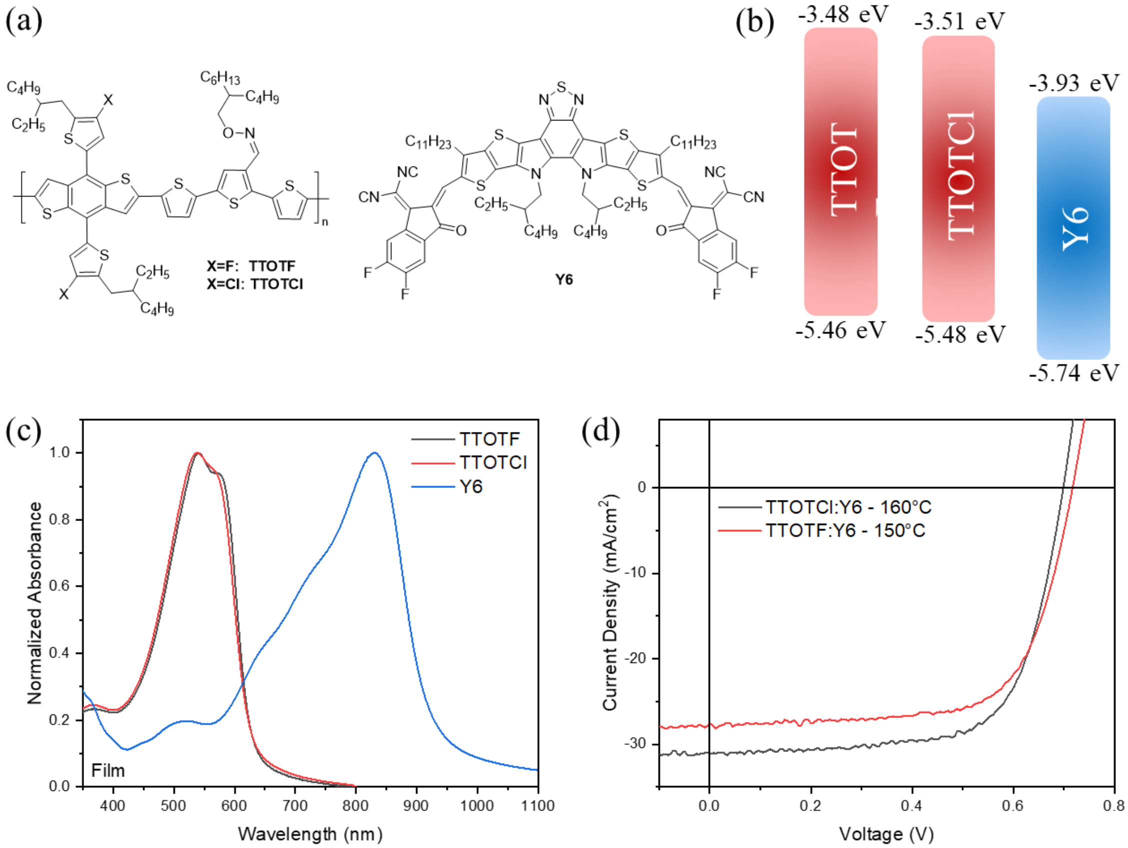

Figure 3-5. (a) Chemical structures of TTOTF, TTOTCl and Y6, (b) frontier energy levels of TTOTF, TTOTCl and Y6 thin films, (c) normalized UV-vis absorption spectra of TTOTF and TTOTCl in thin films with Y6, (d) J-V curves of the OSC devices based on TTOTF:Y6 and TTOTCl:Y6 blend films annealed at 150°C and 160°C for 20 min, respectively.

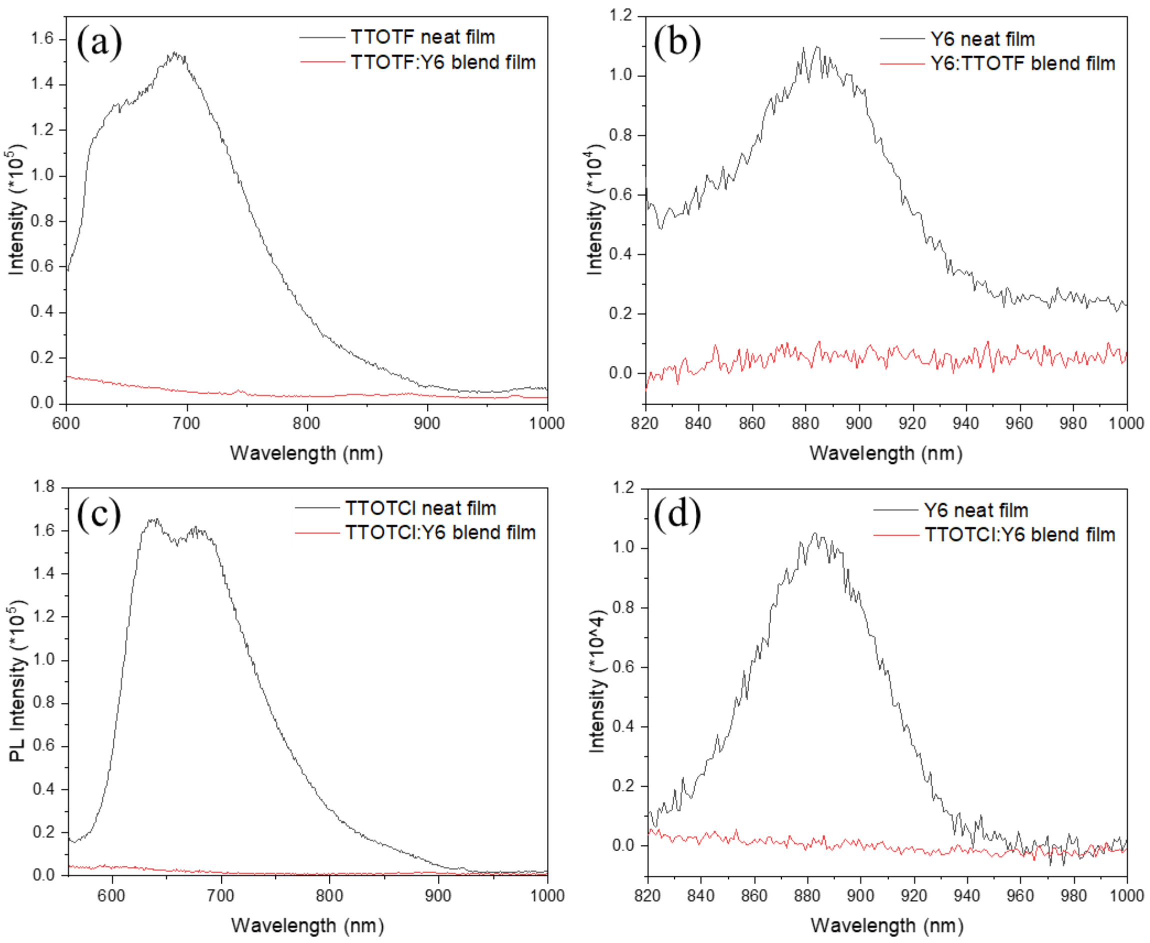

Figure 3-6. PL spectra of (a) TTOTF neat and TTOTF:Y6 blend films excited at 570 nm. (b) Y6 neat and TTOTF:Y6 blend films excited at 800 nm. (c) TTOTCl neat and TTOTCl:Y6 blend films excited at 540 nm. (d) Y6 neat and TTOTCl:Y6 blend films excited at 800 nm.

Prior to device fabrication, the exciton diffusion and dissociation behaviour in the blend film were investigated through PL quenching experiments. As shown in Figure 3-6, TTOTF:Y6 blend film demonstrated good PL quenching efficiencies of 91.7% and 91.1% in the short and long wavelength region, respectively. In comparison, the TTOTCl:Y6 blend film showed better quenching efficiencies of 96.9% for the short wavelength region and 99.7% for the long wavelength region, demonstrating a more effective exciton diffusion and dissociation.

The OSC devices were constructed using an inverted structure of ITO/ZnO/Active layer/MoO_3/Ag, where the active layer consisted of TTOTF or TTOTCl as the polymer donor and the Y6 as the acceptor. Several optimizing techniques were utilized, including the adjustments of active layer thickness, annealing temperatures, different acceptors, solvent additive, D/A ratios and MoO_3 thickness (Table 3-7 to 3-15). The J-V curves under 1.5G illumination (100 mW/cm^2) of the optimized devices are shown in Figure 3-5 (d), and the optimized OSC performance results were summarized in Table 3-2.

Table 3-2. Photovoltaic results of optimized TTOTF and TTOTCl based OSCs.

Active layer	J_{SC} (mA/cm^2) [a]	V_{OC} (V) [a]	FF [a]	PCE (%) [a]
TTOTF:Y6 -RT	25.03 (25.01 ± 0.34)	0.78 (0.77 ± 0.0027)	0.62 (0.61 ± 0.0075)	12.14 (11.91 ± 0.29)
TTOTF:Y6 -150°C	27.61 (26.50 ± 0.62)	0.72 (0.71 ± 0.0060)	0.69 (0.68 ± 0.0093)	13.57 (12.68 ± 0.46)
TTOTCl:Y6 -RT	26.70 (26.45 ± 0.73)	0.79 (0.79 ± 0.0017)	0.63 (0.63 ± 0.016)	13.30 (13.04 ± 0.31)
TTOTCl:Y6 -160°C	31.03 (29.65 ± 1.60)	0.70 (0.70 ± 0.0063)	0.68 (0.68 ± 0.014)	14.91 (14.27 ± 0.51)
TTOTCl:Y6 -160°C[b]	31.18 (29.82 ± 0.69)	0.72 (0.71 ± 0.0059)	0.71 (0.70 ± 0.011)	15.96 (14.78 ± 0.56)

[a] The values in parenthesis are average values and standard deviation obtained from at least four devices.

[b] Spin coated 10M LiTFSI in ACN at 5000 rpm between the active layer and HTL.

The as-cast TTOTF-based device yielded a PCE of 12.14% with a J_{SC} of 25.03 mA/cm^2, a V_{OC} of 0.78 V and an FF of 0.62. Comparing with the non-fluorinated polymer donor TTOT, the V_{OC} of TTOTF-based OSC improved by 0.16 eV. After annealing at 150°C, the PCE of TTOTF:Y6 based device reached 13.57%, with an increased FF of 0.69 and J_{SC} of 27.61 mA/cm^2. On the other hand, the as-cast TTOTCl:Y6 based device showed a high J_{SC} of 26.7 mA/cm^2, a V_{OC} of 0.79 V and an FF of 0.63, resulting in a high PCE of 13.3%. The 160°C annealed OSC achieved an even higher J_{SC} of 31.03 mA/cm^2, and the FF was also enhanced from 0.63 to 0.68, resulting in an excellent PCE close to 15%. However, the V_{OC} of the best TTOTCl-based device was still quite low comparing to other high performance Y6-based OSCs.[39,40,37] The energy loss (E_{loss}) of the device was calculated to be 0.63 eV by using the equation: $E_{loss} = E_g - eV_{OC}$,[78] which falls in the range of most OSCs (0.6 - 1.0 eV).[48,79] Therefore, further V_{OC} improvement in TTOTCl-based devices may be achieved by pairing with a narrow bandgap acceptor with a higher E_{HOMO} to lower the E_{HOMO} offset.

Lithium bis(trifluoromethanesulfonyl)imide (LiTFSI) is widely used as a dopant for the hole transport layer in perovskite solar cells due to its ability to enhance the hole mobility and conductivity of HTL.[80,81] In very few cases, it was used as an additive in the active layer of BHJ OSCs to improve charge carrier transport.[82,83] In this work, a thin layer of LiTFSI layer was spin coated between the active layer and the HTL to enhance the OSC device performance. Several parameters include LiTFSI concentration, processing solvent and thickness were optimized, and results are summarized in Table 3-16 to 3-18. As shown in Table 3-2, the performance of the best LiTFSI-based OSC achieved an excellent PCE of 15.96%, with an enhanced V_{OC} and FF of 0.72 V and 0.71, respectively. However, due to the hygroscopic nature of LiTFSI, the active layer surface of the OSC device was not smooth, which could result in moisture absorption and accelerate device degradation.[84] Additional optimizations and investigations are needed to further improve the film quality and understand the effect of the LiTFSI layer.

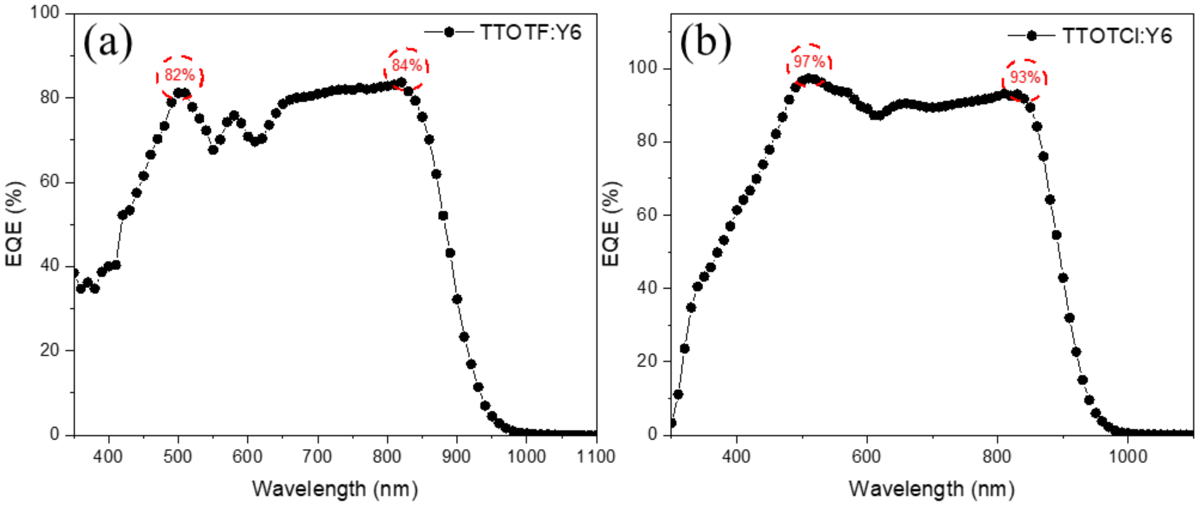

Figure 3-7. EQE spectrum of (a) TTOTF:Y6 based device annealing at 150°C for 20 min and (b) TTOTCl:Y6 based device annealing at 160°C for 20 min.

As shown in Figure 3-7, both EQE spectra exhibited high quenching peak at round 510 nm and 820 nm, which are consistent with the sharp light absorption peaks measured through UV spectra. TTOTF:Y6-based OSC showed the highest EQE of 84% at 820 nm and an integrated J_{SC} of 24.7 mA/cm^2 (with a 10.5% deviation). Whereas TTOTCl:Y6-based OSC showed a significantly enhanced EQE of over 85% in the 470 to 850 nm region, and reaching 97% at 510 nm. In addition, the integrated J_{SC} is 29.51 mA/cm^2, which agrees well with the measured J_{SC} with a 4.9% deviation. These results demonstrated that the active layer thickness of the optimized device was enough to have sufficient light absorption and the generated charge carriers in the device were efficiently transported and collected to produce photocurrents.[85]

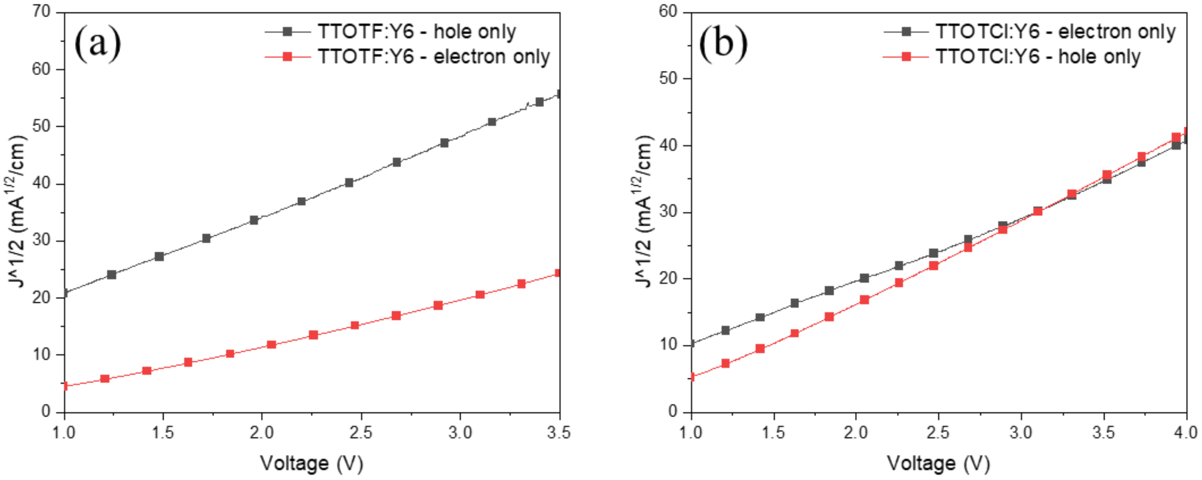

Figure 3-8. $J^{1/2}$-V curves of hole-only and electron-only devices of (a) TTOTF:Y6 and (b) TTOTCl:Y6 systems.

SCLC mobility measurements were carried out to study the charge carrier mobilities of TTOTF and TTOTCl polymers. Hole-only and electron-only devices with configurations of ITO/PEDOT:PSS (40nm)/Active layer/MoO_3 (10 nm)/Ag (100 nm) and ITO/ZnO (40 nm)/Active layer/LiF (1 nm)/Al (100 nm), respectively, were fabricated.

Table 3-3. SCLC mobilities of TTOTF and TTOTCl neat films and blend films annealed at 150 °C and 160 °C.

Neat film / Blend film	$\mu_{h,max}$ ($\mu_{h,avg}$ ± std) ($cm^2\ V^{-1}\ S^{-1}$) [a]	$\mu_{e,max}$ ($\mu_{e,avg}$ ± std) ($cm^2\ V^{-1}\ S^{-1}$) [a]	μ_h / μ_e
TTOTF - 150°C	$6.26\times10^{-4}(5.17\times10^{-4}\pm8.44\times10^{-5})$	-	-
TTOTCl - 160°C	$1.36\times10^{-3}(1.11\times10^{-3}\pm1.15\times10^{-4})$	-	-
TTOTF:Y6 - 150°C	$1.13\times10^{-3}(8.73\times10^{-4}\pm1.41\times10^{-4})$	$6.26\times10^{-4}(5.17\times10^{-4}\pm8.44\times10^{-5})$	1.81
TTOTCl:Y6 - 160°C	$9.34\times10^{-4}(8.47\times10^{-4}\pm7.44\times10^{-5})$	$6.12\times10^{-4}(4.40\times10^{-4}\pm1.37\times10^{-4})$	1.53

[a] Above values are obtained from at least four devices.

As shown in Table 3-3, the hole mobilities (μ_h's) of the TTOTF and TTOTCl neat films under the optimum conditions were measured to be 6.26×10^{-4} cm^{2}V^{-1}s^{-1} and 1.36×10^{-3} cm^{2}V^{-1}s^{-1}, respectively. For the TTOTF:Y6 blend films, the measured SCLC μ_h and μ_e are 1.13×10^{-3} cm^{2}V^{-1}s^{-1} and 6.26×10^{-4} cm^{2}V^{-1}s^{-1}, respectively, which are both one order of magnitude higher than μ_h (2.84×10^{-4} cm^{2}V^{-1}s^{-1}) and μ_e (3.22×10^{-5} cm^{2}V^{-1}s^{-1}) achieved in the TTOT:Y6 system. While for the TTOTCl:Y6 blend, the best μ_h and μ_e were measured to be 9.34×10^{-4} cm^{2}V^{-1}s^{-1} and 1.36×10^{-3} cm^{2}V^{-1}s^{-1}, respectively. Although the μ_h of TTOTCl:Y6 system is slightly lower than that of TTOTF:Y6-based OSC, the more balanced μ_h/μ_e (1.53 vs. 1.82) is beneficial for achieving high J_{SC} and FF in the TTOTCl:Y6-based OSCs.

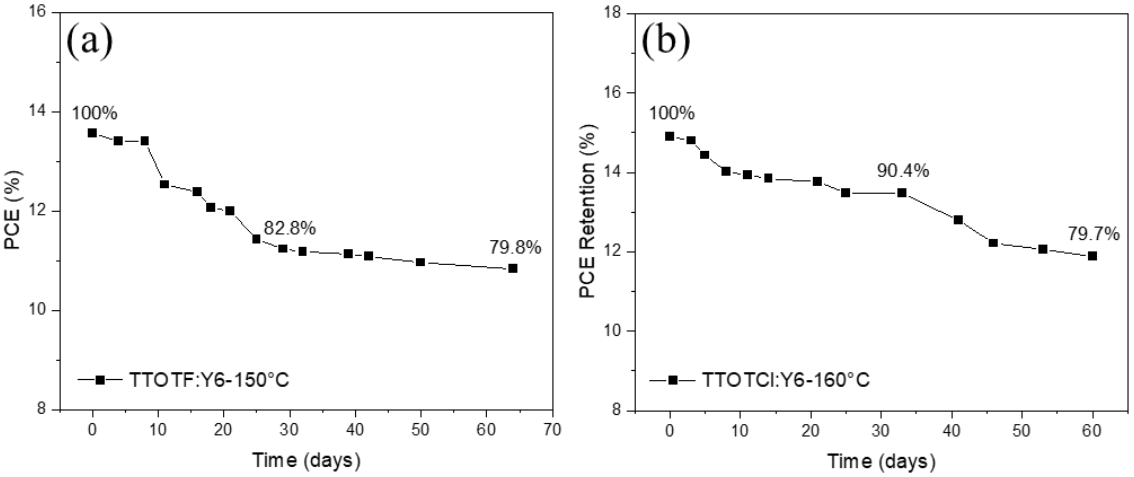

Figure 3-9. Stability tests conducted on unencapsulated best performance device of (a) TTOTF:Y6 and (b) TTOTCl:Y6 in ambient condition over a two-month period.

As the PCE of non-fullerene OSCs approaches commercial viability, achieving good long-term stability in both materials and devices is critical. Thus, the stability of the best performing device based on TTOTF:Y6 and TTOTCl:Y6 (without LiTFSI) systems were investigated by storing the freshly made device in ambient conditions without encapsulation. As shown in Figure 3-9, the

TTOTF:Y6-based device maintained 82.8% of the initial PCE over a 30-day duration. After a 64-day storage time, the device still maintained nearly 80% of the initial PCE. Furthermore, the TTOTCl:Y6-based OSC showed an even better air stability by retaining 90.4% PCE after a 30-day storage time. Similarly, it had an 80% PCE retention after a two-month period. It is worth mentioning that this degradation rate is one of the slowest achieved in unencapsulated non-fullerene and fullerene based OSCs.[86,87,88] Degradation of OSCs could be caused by the physical and chemical degradation in the active layer and carrier transport layers, or the defects formed at the interface between the active layer, HTL or electrodes due to the moisture and oxygen in ambient air.[87] The J_{SC} of both TTOTF-based and TTOTCl-based devices remained almost the same (31.0 to 30.9 mA/cm^2; 27.61 to 27.32 mA/cm^2) after 60 days (Table 3-4 and Table 3-5), indicating that the active layer materials are highly stable. The drop in PCE of both devices is mainly due to the decrease in the FF (from 0.69 to 0.60 for TTOTF and 0.68 to 0.57 for TTOTCl). It was found that the series resistance (Rs) of both devices increased slowly over time and the shunt resistance (Rsh) dropped dramatically, which is most likely caused by the degradation of the top Ag electrode layer and the MoO_3 hole transporting layer due to oxygen and moisture in the ambient air.

Table 3-4. Performances of the best TTOTF:Y6 based OSC device for over 2-month storage time under ambient condition without encapsulation.

Time (d)	J_{SC} (mA/cm^2)	V_{OC} (V)	FF	PCE (%)	Rs (ohmcm^2)	Rsh (ohmcm^2)
0	27.61	0.72	0.69	13.57	3.23	631.34
16	27.44	0.69	0.65	12.38	3.64	425.18
32	27.29	0.67	0.61	11.18	3.88	302.90
64	27.32	0.66	0.60	10.83	3.90	208.72

Table 3-5. Performances of the best TTOTCl:Y6 based OSC device for a 2-month storage time under ambient condition without encapsulation.

Time (d)	J_{SC} (mA/cm^2)	V_{OC} (V)	FF	PCE (%)	Rs (ohmcm^2)	Rsh (ohmcm^2)
0	31.0	0.70	0.68	14.91	2.84	883.08
10	30.8	0.69	0.65	13.84	3.11	548.76
20	31.0	0.69	0.63	13.76	3.21	313.05
40	31.0	0.68	0.60	12.79	3.45	260.91
60	30.9	0.68	0.57	11.88	3.95	193.43

The surface morphology of the active layer was examined through AFM and the molecular packing of polymer donors and blend film was studied by XRD measurements.

As shown in Figure 3-10, the root mean square (RMS) roughness was 1.03 nm for the as-cast TTOTF-based device. After annealing at 150°C, the RMS value slightly increased to 1.08 nm due to the annealing effect. While the TTOTCl:Y6 blend film at both room temperature and 160°C annealing temperature showed smaller RMS roughness values of 0.92 nm and 0.94 nm, respectively. This result suggests a smoother surface morphology and favorable interaction between TTOTCl and Y6, induced by the chlorine atom of the polymer donor TTOTCl. The more uniform surface morphology of the TTOTCl:Y6 blend film formed a desirable nanoscale phase separation and interpenetrating network in the active layer. This is beneficial for efficient charge dissociation and transportation, as well as minimizing recombination loss in OSCs, eventually resulting in higher J_{SC} and OSC performance.[89,90] In addition, the much smaller surface roughness of TTOTCl:Y6 blend film is also favorable for obtaining close contact between the active layer and HTL, which is favorable for obtaining higher FF.

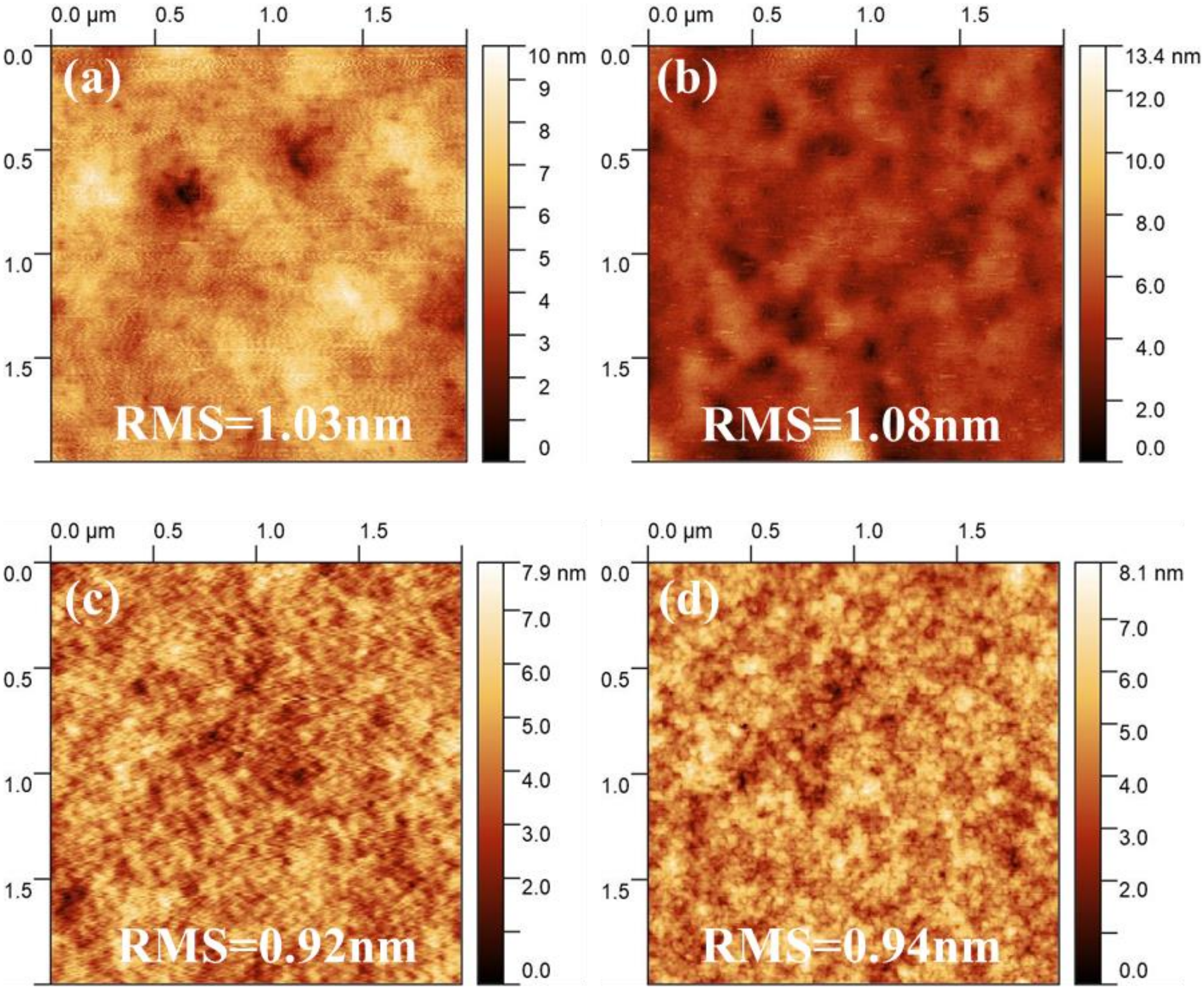

Figure 3-10. AFM height images of TTOTF:Y6 blend film at room temperature (a) and annealing at 150°C (b), TTOTCl:Y6 blend film at room temperature (c) and annealing at 160°C (d).

As shown in Figure 3-11 (a, b), neither lamellar nor π- π stacking peak was observed in room temperature TTOTF neat film in both in-plane and out-of-plane directions. The broad peak at 2θ = ~21° of the TTOTF neat film in the in-plane direction slowly intensified with the increasing temperatures. The π- π stacking (010) peak (2θ = ~21°) in the out-of-plane line cuts appeared at annealing temperature of 150°C and 200°C, indicating a more crystalline and ordered molecular packing of TTOTF when annealed above 150°C. Furthermore, a lamellar peak at 2θ = 4.89° with a d-spacing of 0.90 nm appeared in the 50°C annealed TTOTF neat film. The (001) peak intensified and decreasing d-spacings (0.9 nm for 100°C, 0.885 nm for 150°C and 0.866 nm for 200°C) were observed in TTOTF neat films with increased annealing temperatures. However, no peaks were observed in the 150°C-annealed TTOTF:Y6 blend film in both directions, indicating poor crystallinity and amorphous features in the active layer. On the other hand, a peak at 2θ = 5.0° was observed for the as-spun TTOTCl neat film, which corresponds to the (001) planes of the polymer main chain π-stacks with an interlamellar distance of 1.77 nm. As the annealing temperature increased, this (001) peak intensified, indicating that the crystallinity of the polymer film improved. The d-spacing decreased slightly to 1.73 nm for the 130°C-annealed TTOTCl film (2θ = ~5.1°) and to 1.70 nm for the 160°C- and 190°C-annealed TTOTCl films (2θ = ~5.2°). The peak at 2θ = ~21° weakened with increasing annealing temperatures in the in-plane and out-of-plane directions, but remained strong even at a high annealing temperature of 190 °C. The broad peak centered at 2θ = ~21° for the annealed TTOTCl films might be composed of the π- π stacking (010) peak with a π-π distance of 0.42 nm. Comparing to the TTOT neat films, the above XRD data clearly show that fluorination and chlorination of BDT significantly helped to improve the polymer chain packing of TTOTF and TTOTCl. However, as show in Figure 3-12, the optimized 160°C- annealed TTOTCl:Y6 blend film showed no (001) peak in the out-of-plane direction, indicating that TTOTCl became more disordered in the blend film, which can account for the lower SCLC hole mobility compared to the TTOTCl neat film.

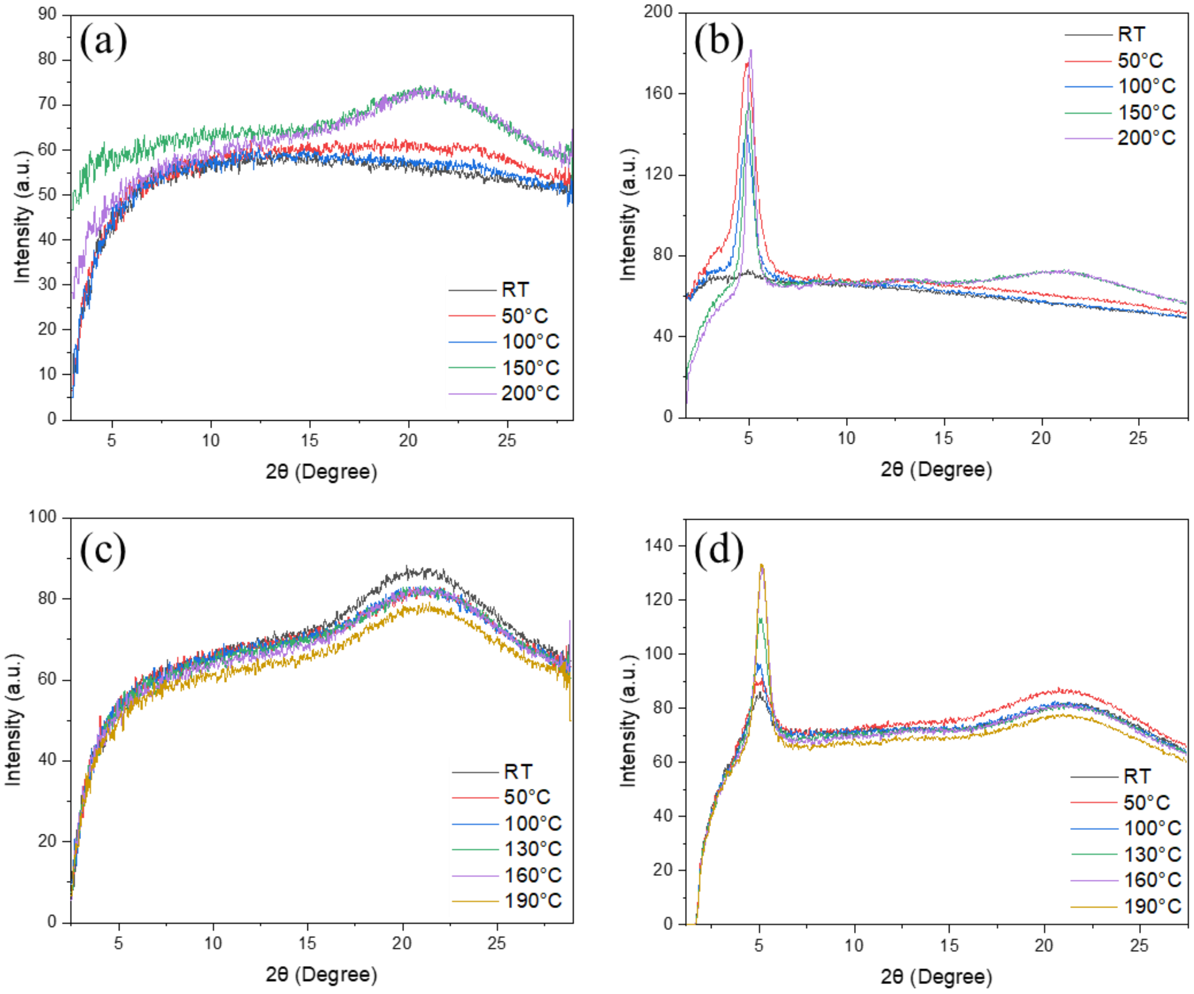

Figure 3-11. In-plane and out-of-plane line cuts of GIXD patterns of (a, b) TTOTF and (c, d) TTOTCl neat films at different annealing temperatures.

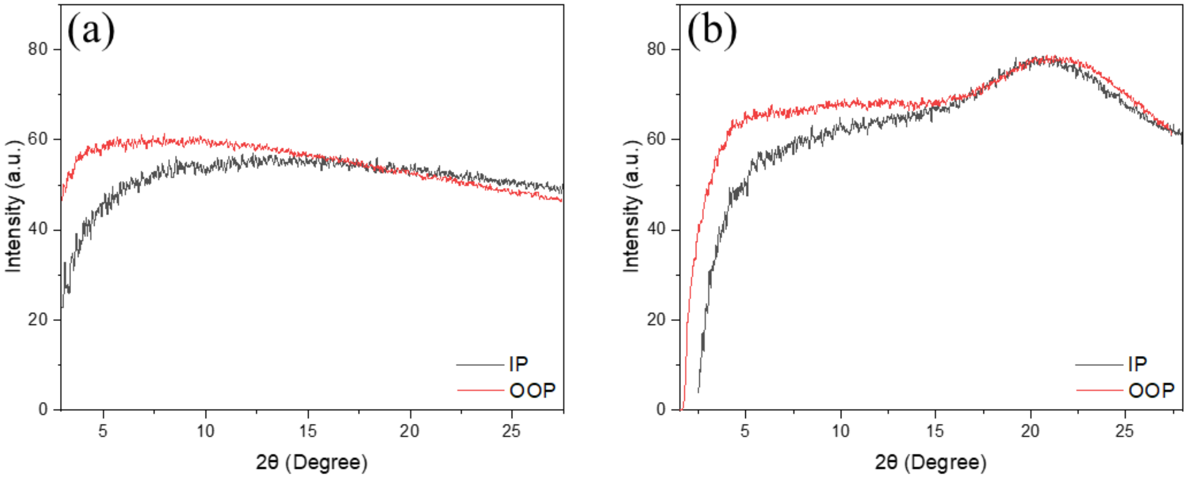

Figure 3-12. In-plane and out-of-plane line cuts of GIXD patterns of (a) TTOTF:Y6 blend film annealed at 150°C and (b) TTOTCl:Y6 blend film annealed at 160°C.

3.6 Conclusions and future directions

To summarize, two new wide bandgap polymer donors TTOTF and TTOTCl were designed and synthesized by utilizing the halogenation strategy. Both polymers showed strong UV absorption between 425 to 620 nm with wide optical bandgaps of over 1.97 eV. The incorporation of the fluorine atom successfully brought down the E_{HOMO} of TTOT from -5.33 to -5.46 eV. The optimized OSC device based on TTOTF:Y6 showed a significantly improved PCE of 13.57%, with a V_{OC} of 0.72 V, an increased FF of 0.69 and a J_{SC} of 27.61 mA/cm^2. On the other hand, the incorporation of the chlorine atom further downshifted the E_{HOMO} to -5.48 eV. The hole mobility of the TTOTCl neat film still maintained at a magnitude of 10^{-3} cm^{2}V^{-1}S^{-1}. As a result, the optimized TTOTCl based OSC achieved a record-high J_{SC} of 31.03 mA/cm^2, an FF of 0.68 and a V_{OC} of 0.70 V, resulting in a two-fold higher PCE of 14.91% comparing to TTOT-based OSC. Furthermore, comparing with TTOTF-based OSCs, the TTOTCl-based devices showed a more balanced μ_h/μ_e ratio (1.53 vs. 1.81), higher EQE quenching efficiency and more favorable film morphology, resulting in a better J_{SC} and photovoltaic performance. In addition, with the incorporation of the LiTFSI layer, the best TTOTCl-based OSC showed an improvement in both Voc and FF, resulting in a 7% PCE enhancement (PCE=15.96%) comparing with the device without LiTFSI. The stability studies conducted on unencapsulated TTOTF and TTOTCl-based devices demonstrated the great potential of both materials to achieve long-term stability in ambient conditions. This work demonstrated that the halogenation on the polymer donor is highly effective for bringing down E_{HOMO}, reducing energy loss and enhancing device performance in OSCs. It also indicated that TTOTCl is a promising wide bandgap polymer donor for the development of highly efficient and air stable non-fullerene OSCs.

Despite the high device performance, the V_{OC} and FF still remained relatively low to the state-of-art values (FF: up to 0.78,[50] V_{OC}: up to 1.1 V[91]) in non-fullerene OSCs. The V_{OC} improvement in TTOTCl-based devices may be achieved by pairing with a narrow bandgap acceptor with a higher E_{HOMO} to lower the E_{HOMO} offset and reduce the energy loss in OSCs. Further investigations and optimizations also need to be carried out to understand the effect of LiTFSI layer and improve the film quality.

3.7 Experimental section

Synthesis of TTOTCl and TTOTF

To a dried 25ml 2-necked round bottom flask, tris(o-tolyl)phosphine ($P(o\text{-}tol)_3$) (0.08 equiv.), compound 4 (1 equiv.) and BDTTDFSn (1 equiv.) or BDTTDClSn (1 equiv.) were added. This was followed by adding 4ml anhydrous chlorobenzene and stirring the mixture until dissolved. Then tris-(dibenzylideneacetone)dipalladium ($Pd_2(dba)_3$) (0.02 equiv.) was injected through septum in anhydrous chlorobenzene to the stirring mixture. After 24 h reaction at 90°C under dark and argon atmosphere, 0.5 ml 2-bromobenzene was added. After cooling to room temperature, the mixture was poured into 150 ml methanol. The solid was collected by filtration, purified through Soxhlet extraction using acetone, hexane, and chloroform. The target polymer TTOTF and TTOTCl were obtained from chloroform fraction, the yield was 47.0mg (45%) and 148.5mg (99%) respectively.

OSC device fabrication

The OSC devices were fabricated using an inverted structure of ITO/ZnO (40 nm)/Active layer/MoO3 (10 nm)/Ag (100 nm). The ITO glass substrate was emersed and ultrasonicated in deionized water, HPLC acetone and HPLC iso-propanol for 20 minutes. The ZnO precursor solution was prepared by mixing 197 mg zinc acetate, 54 µl ethanolamine and 2 ml 2-methoxyethanol at room temperature overnight. Then the solution was filtered with 0.22 µm PTFE filter before use. A 40-nm thick ZnO was spin coated onto 10 min O_2 plasma cleaned ITO glass substrate at a spin rate of 3500 rpm for 60 s, followed by annealing at 200°C for one hour in the air. The active layer was prepared by stirring a mixture of donor and acceptor material (D/A ratio=1:1) at a concentration of 20 mg/ml overnight in the glovebox. Then the solution was filtered through a 0.22 µm PTFE filter. TTOTF:Y6 (117 nm) and TTOTCl:Y6 (120 nm) was coated onto the substrate at a spin rate of 2000 and 3000 rpm, respectively. The device was then transferred to the thermal evaporator and vacuumed until the chamber pressure is below 1×10^{-6} torr. The MoO_3 layer (10 nm) was coated at a deposition rate of 0.5 Å/s, and the Ag layer (100 nm) was coated at a deposition rate of 1 Å/s. Each device has an area of 0.0574 cm^2. An Agilent B2912A Semiconductor Analyzer equipped with a Science Tech SLB300-A Solar Simulator was used to measure the current density-voltage (J-V) curve, and the light source came from a 450 W xenon lamp and an air mass (AM 1.5G) filter.

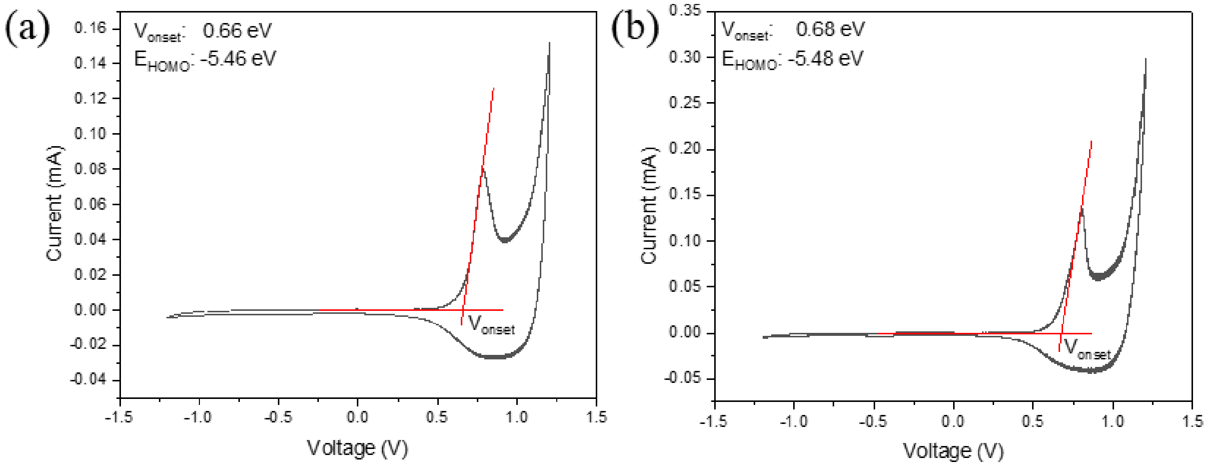

Figure 3-13. Cyclic voltammograms of (a) TTOTF and (b) TTOTCl thin films.

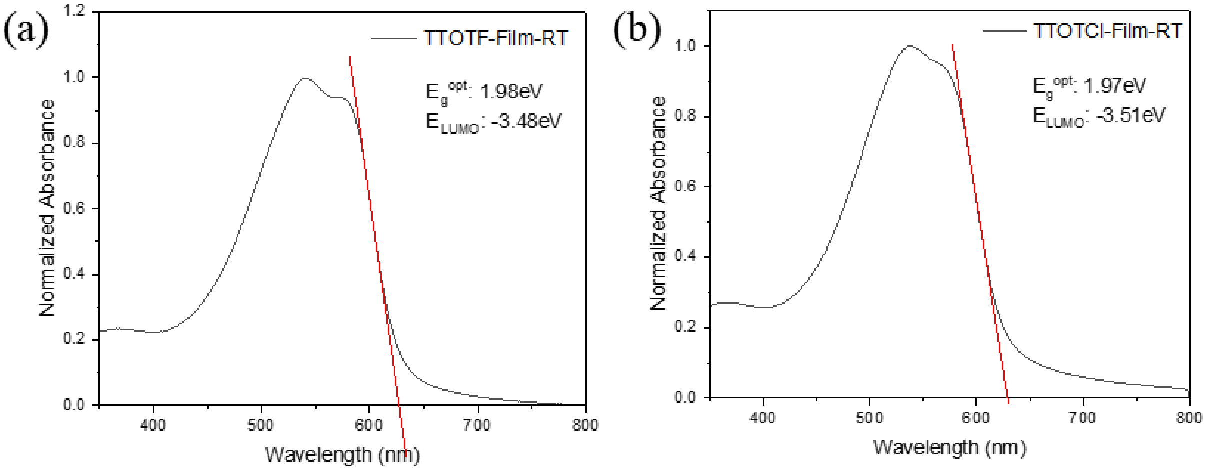

Figure 3-14. UV-vis absorption spectra of (a) TTOTF and (b) TTOTCl thin films at room temperature.

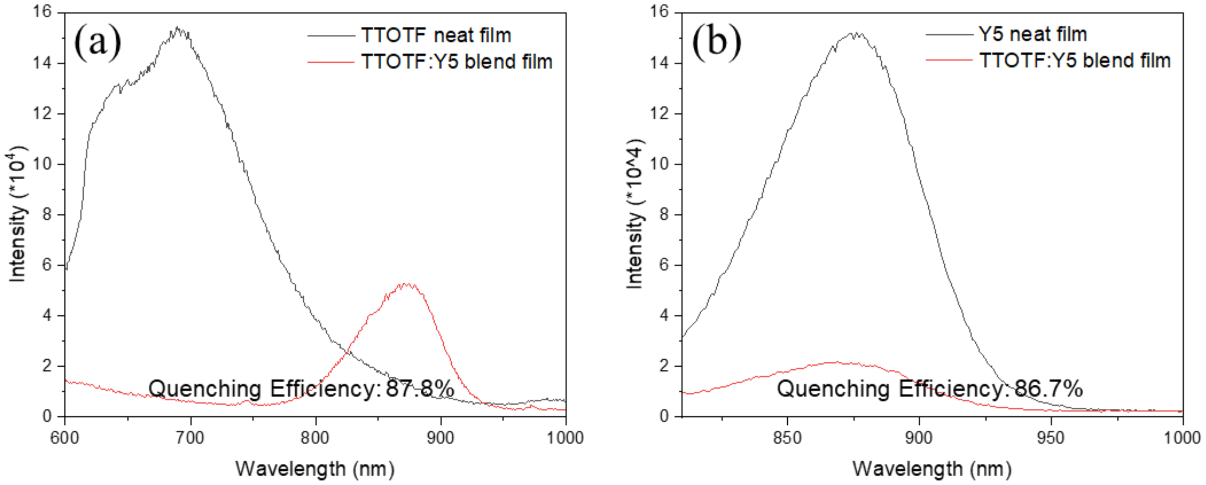

Figure 3-15. PL spectra and quenching efficiencies of (a) TTOTF neat and TTOTF:Y5 blend films excited at 570 nm. (b) Y5 neat and TTOTF:Y5 blend films excited at 790 nm.

Table 3-7. Performance optimization of TTOTF:Y6 based devices with different active layer film thickness.

Temperature	Thickness	J_{SC} (mA/cm^2) [a]	V_{OC} (V) [a]	FF [a]	PCE (%) [a]
RT	146 nm	25.48 (24.92± 1.16)	0.77 (0.77 ± 0.0021)	0.56 (0.50 ± 0.016)	10.17 (9.58 ± 0.74)
RT	117 nm	25.03 (25.01 ± 0.34)	0.78 (0.77 ± 0.0027)	0.62 (0.61 ± 0.0075)	12.14 (11.91 ± 0.29)
RT	108 nm	24.00 (23.61 ± 0.31)	0.78 (0.78 ± 0.0001)	0.64 (0.63 ± 0.0067)	11.89 (11.58 ± 0.22)
RT	100 nm	23.55 (22.62 ± 0.98)	0.78 (0.78 ± 0.0032)	0.62 (0.63 ± 0.0054)	11.36 (10.99 ± 0.45)

Processing solvent: chloroform, D/A ratio: 1:1.

[a] The values in parenthesis are average values and standard deviation obtained from at least four devices.

Table 3-8. Performance optimization of TTOTF:Y6 based devices with different annealing temperatures.

Temperature	J_{SC} (mA/cm^2) [a]	V_{OC} (V) [a]	FF [a]	PCE (%) [a]
RT	25.03 (25.01 ± 0.34)	0.78 (0.77 ± 0.0027)	0.62 (0.61 ± 0.0075)	12.14 (11.91 ± 0.29)
100 °C	26.20 (25.68 ± 0.89)	0.75 (0.75 ± 0.0051)	0.65 (0.64 ± 0.021)	12.77 (12.15 ± 0.46)
150 °C	**27.61 (26.50 ± 0.62)**	**0.72 (0.71 ± 0.0060)**	**0.69 (0.68 ± 0.0093)**	**13.57 (12.68 ± 0.46)**
200 °C	25.37 (24.77 ± 1.17)	0.68 (0.68 ± 0.0041)	0.68 (0.66 ± 0.012)	11.82 (11.11 ± 0.60)

Processing solvent: chloroform, D/A ratio: 1:1, annealing time: 20min, active layer thickness: 117nm.

[a] The values in parenthesis are average values and standard deviation obtained from at least four devices.

Table 3-9. Performance optimization of TTOTF:Y5 based devices with different active layer film thickness.

Temperature	Spin speed (rpm)	J_{SC} (mA/cm^2) [a]	V_{OC} (V) [a]	FF [a]	PCE (%) [a]
RT	3000	16.83 (15.87± 0.44)	0.95 (0.95 ± 0.0039)	0.55 (0.55 ± 0.0066)	8.76 (8.24 ± 0.24)
RT	2000	18.35 (16.98 ± 0.70)	0.95 (0.95 ± 0.0029)	0.56 (0.55 ± 0.019)	9.64 (8.79 ± 0.36)
RT	1000	18.29 (17.67 ± 0.45)	0.94 (0.94 ± 0.0023)	0.54 (0.54 ± 0.013)	9.38 (9.02 ± 0.31)
RT	800	16.43 (15.80 ± 0.48)	0.94 (0.94 ± 0.0022)	0.52 (0.52 ± 0.0050)	8.00 (7.71 ± 0.28)

Processing solvent: chloroform, D/A ratio: 1:1.

[a] The values in parenthesis are average values and standard deviation obtained from at least four devices.

Table 3-10. Performance optimization of TTOTF:Y5 based devices with different annealing temperatures.

Temperature	J_{SC} (mA/cm^2) [a]	V_{OC} (V) [a]	FF [a]	PCE (%) [a]
RT	18.35 (16.98 ± 0.70)	0.95 (0.95 ± 0.0029)	0.56 (0.55 ± 0.019)	9.64 (8.79 ± 0.36)
100 °C	17.86 (17.81 ± 0.25)	0.94 (0.94 ± 0.0033)	0.58 (0.57 ± 0.0064)	9.80 (9.56 ± 0.18)
150 °C	17.37 (16.51 ± 0.62)	0.92 (0.92 ± 0.0019)	0.61 (0.61 ± 0.0034)	9.79 (9.21 ± 0.38)
200 °C	7.26 (5.34 ± 1.37)	0.88 (0.86 ± 0.013)	0.50 (0.45 ± 0.034)	3.18 (2.11 ± 0.75)

Processing solvent: chloroform, D/A ratio: 1:1, annealing time: 20min, active layer thickness: 119nm.

[a] The values in parenthesis are average values and standard deviation obtained from at least four devices.

Table 3-11. Performance optimization of TTOTCl:Y6 based devices with different active layer film thickness and solvent additive.

Temperature/SA	Thickness	J_{SC} (mA/cm^2) [a]	V_{OC} (V) [a]	FF [a]	PCE (%) [a]
RT	170 nm	25.76 (25.18 ± 0.51)	0.77 (0.77 ± 0.0018)	0.52 (0.52 ± 0.011)	10.36 (10.04 ± 0.24)
RT	130 nm	27.78 (26.94 ± 0.57)	0.79 (0.79 ± 0.0031)	0.59 (0.59 ± 0.0073)	13.05 (12.58 ± 0.36)
RT	120 nm	26.70 (26.45 ± 0.73)	0.79 (0.79 ± 0.0017)	0.63 (0.63 ± 0.016)	13.30 (13.04 ± 0.31)
RT	105 nm	25.03 (24.00 ± 0.81)	0.78 (0.77 ± 0.0057)	0.65 (0.63 ± 0.037)	12.72 (11.66 ± 0.88)
RT with 0.5% CN	105 nm	22.69 (22.18 ± 0.29)	0.78 (0.77 ± 0.0017)	0.70 (0.69 ± 0.0041)	12.28 (11.93 ± 0.19)

Processing solvent: chloroform, D/A ratio: 1:1.

[a] The values in parenthesis are average values and standard deviation obtained from at least four devices.

Table 3-12. Performance optimization of TTOTCl:Y6 based devices with different annealing temperatures.

Temperature	J_{SC} (mA/cm^2) [a]	V_{OC} (V) [a]	FF [a]	PCE (%) [a]
RT	26.70 (26.45 ± 0.73)	0.79 (0.79 ± 0.0017)	0.63 (0.63 ± 0.016)	13.30 (13.04 ± 0.31)
100 °C	27.26 (26.69 ± 0.64)	0.76 (0.75 ± 0.0059)	0.67 (0.67 ± 0.0045)	14.00 (13.44 ± 0.36)
130 °C	28.77 (27.98 ± 0.79)	0.73 (0.73 ± 0.0028)	0.69 (0.69 ± 0.0085)	14.43 (13.92 ± 0.31)
160 °C	**31.03 (29.65 ± 1.60)**	**0.70 (0.70 ± 0.0063)**	**0.68 (0.68 ± 0.014)**	**14.91 (14.27 ± 0.51)**
190 °C	27.14 (27.07 ± 0.45)	0.68 (0.68 ± 0.0039)	0.70 (0.69 ± 0.014)	13.04 (12.62 ± 0.47)

Processing solvent: chloroform, D/A ratio: 1:1, annealing time: 20min, active layer thickness: 120nm.

[a] The values in parenthesis are average values and standard deviation obtained from at least four devices.

Table 3-13. Performance optimization of TTOTCl:Y6 based devices with different D/A ratio.

D/A ratio	J_{SC} (mA/cm^2) [a]	V_{OC} (V) [a]	FF [a]	PCE (%) [a]
1:1	31.03 (29.65 ± 1.60)	0.70 (0.70 ± 0.0063)	0.68 (0.68 ± 0.014)	14.91 (14.27 ± 0.51)
1:1.2	29.15 (28.40 ± 0.44)	0.72 (0.71 ± 0.0035)	0.67 (0.65 ± 0.0015)	13.97 (13.05 ± 0.60)
1.2:1	27.73 (27.17 ± 0.41)	0.71 (0.71 ± 0.0055)	0.68 (0.67 ± 0.0096)	13.39 (12.81 ± 0.47)

Processing solvent: chloroform, annealing condition: 160 °C for 20min, active layer thickness: 120nm.

[a] The values in parenthesis are average values and standard deviation obtained from at least four devices.

Table 3-14. Performance optimization of TTOTCl:Y6 based devices with different acceptors.

Acceptor	Thickness	J_{SC} (mA/cm^2) [a]	V_{OC} (V) [a]	FF [a]	PCE (%) [a]
Y6	120 nm	26.70 (26.45 ± 0.73)	0.79 (0.79 ± 0.0017)	0.63 (0.63 ± 0.016)	13.30 (13.04 ± 0.31)
ITIC	144 nm	16.96 (16.51 ± 0.27)	0.97 (0.71 ± 0.0047)	0.62 (0.62 ± 0.0037)	10.29 (9.98 ± 0.22)
ITIC	132 nm	16.84 (16.59 ± 0.24)	0.97 (0.97 ± 0.0039)	0.63 (0.62 ± 0.0042)	10.31 (10.06 ± 0.20)
ITIC	114 nm	15.19 (15.21 ± 0.67)	0.98 (0.97 ± 0.0038)	0.64 (0.63 ± 0.013)	9.55 (9.38 ± 0.29)
ITIC	104 nm	14.59 (13.90 ± 0.69)	0.97 (0.71 ± 0.0047)	0.63 (0.63 ± 0.0010)	9.04 (8.56 ± 0.48)

Processing solvent: chloroform, D/A ratio: 1:1.

[a] The values in parenthesis are average values and standard deviation obtained from at least four devices.

Table 3-15. Performance optimization of TTOTCl:Y6 based devices with different MoO_3 thickness.

MoO_3 Thickness	J_{SC} (mA/cm^2) [a]	V_{OC} (V) [a]	FF [a]	PCE (%) [a]
10	31.03 (29.65 ± 1.60)	0.70 (0.70 ± 0.0063)	0.68 (0.68 ± 0.014)	14.91 (14.27 ± 0.51)
8	29.52 (27.02 ± 1.26)	0.71 (0.70 ± 0.0054)	0.69 (0.65 ± 0.011)	14.42 (13.15 ± 0.69)
12	28.76 (28.24 ± 0.47)	0.71 (0.71 ± 0.0030)	0.68 (0.68 ± 0.0025)	13.86 (13.64 ± 0.24)

Processing solvent: chloroform, D/A ratio: 1:1, annealing condition: 160 ^{o}C for 20min, active layer thickness: 120nm.

[a] The values in parenthesis are average values and standard deviation obtained from at least four devices.

Table 3-16. Performance optimization of TTOTCl:Y6 based devices with LiTFSI layer in ACN.

LiTFSI Spin Speed (rpm)	J_{SC} (mA/cm^2) [a]	V_{OC} (V) [a]	FF[a]	PCE (%) [a]	Rs (ohmcm^2)	Rsh (ohmcm^2)
4000	29.98 (29.38 ± 0.75)	0.72 (0.71 ± 0.0079)	0.71 (0.70 ± 0.0083)	15.31 (14.55 ± 0.52)	2.92	599
5000	**31.18 (29.82 ± 0.69)**	**0.72 (0.71 ± 0.0059)**	**0.71 (0.70 ± 0.011)**	**15.96 (14.78 ± 0.56)**	**2.47**	**364**

Active layer: TTOTCl:Y6-160°C, LiTFSI processing solvent: ACN, LiTFSI concentration: 10M.

[a] The values in parenthesis are average values and standard deviation obtained from at least four devices.

Table 3-17. Performance optimization of TTOTCl:Y6 based devices with LiTFSI layer in DMF and NMP.

LiTFSI Solvent	LiTFSI Thickness (nm)	J_{SC} (mA/cm^2)	V_{OC} (V)	FF	PCE (%)	Rs (ohmcm^2)	Rsh (ohmcm^2)
DMF	40	28.59	0.68	0.66	12.85	3.24	697
DMF	30	28.38	0.70	0.68	13.46	3.33	349
DMF	10	29.88	0.70	0.66	13.74	3.29	483
NMP	40	27.44	0.68	0.66	12.49	3.21	663
NMP	30	28.13	0.69	0.65	12.72	3.42	581
NMP	10	27.84	0.70	0.67	13.09	3.35	646
Without LiTFSI		31.03	0.70	0.68	14.91	2.84	883

Active layer: TTOTCl:Y6-160°C, LiTFSI concentration: 10M.

Table 3-18. Performance optimization of TTOTCl:Y6 based devices with LiTFSI layer in ACN.

Solvent	LiTFSI Spin Speed (rpm)	J_{SC} (mA/cm^2)	V_{OC} (V)	FF	PCE (%)	Rs (ohmcm^2)	Rsh (ohmcm^2)
ACN	3000	28.90	0.72	0.69	14.28	3.57	550
ACN	4000	27.80	0.73	0.72	14.51	2.73	590
ACN	5000	28.70	0.72	0.71	14.74	2.67	577
ACN	6000	29.83	0.73	0.71	15.36	2.62	912

Active layer: TTOTCl:Y6-160°C, LiTFSI processing solvent: ACN, LiTFSI concentration: 6M.

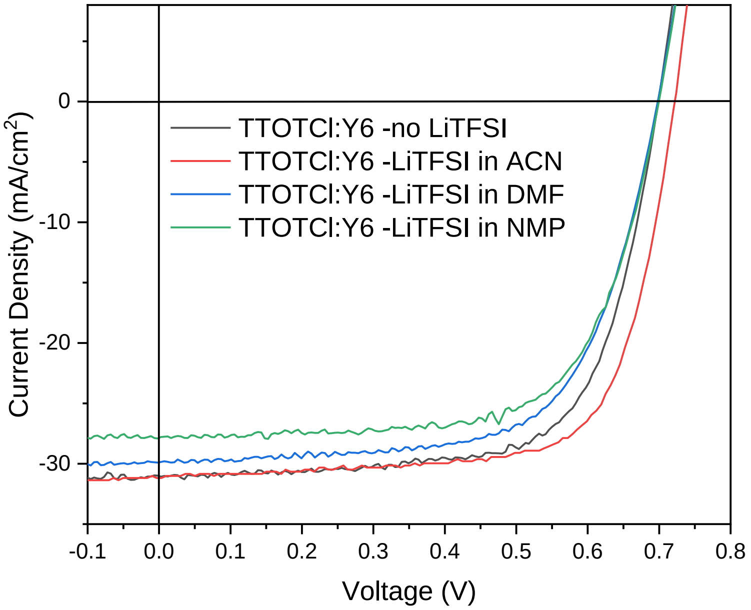

Figure 3-16. J-V curves of the OSC devices based on the optimized TTOTCl:Y6 blend films annealed at 160°C without LiTFSI layer and with LiTFSI in ACN, DMF and NMP.

Table 3-19. Dielectric constant and hole mobility of TTOTF and TTOTCl blend films.

	Temp	C_g (pF) [a]	f (Hz)	ε_r[a]	$\mu_{h,max}$ ($\mu_{h,avg}$ ± std) ($cm^2\ V^{-1}\ S^{-1}$) [a]
TTOTF:Y6	RT	1406	5×10^5	4.04	2.71×10^{-4} ($2.28\times10^{-4} \pm 3.15\times10^{-5}$)
	150°C	1495	5×10^5	4.30	1.13×10^{-3} ($8.73\times10^{-4} \pm 1.41\times10^{-4}$)
TTOTCl:Y6	RT	1864	5×10^5	6.24	4.85×10^{-4} ($4.40\times10^{-4} \pm 3.87\times10^{-5}$)
	160°C	1909	5×10^5	6.39	9.34×10^{-4} ($8.47\times10^{-4} \pm 7.44\times10^{-5}$)

[a] Above values are obtained from at least five devices.

Table 3-20. Dielectric constant and hole mobility of TTOTF and TTOTCl neat films.

Neat Film	Temp	C_g (pF) [a]	f (Hz)	ε_r[a]	$\mu_{h,max}$ ($\mu_{h,avg}$ ± std) ($cm^2\ V^{-1}\ S^{-1}$) [a]
TTOTF	RT	758	5×10^5	2.54	9.09×10^{-4} ($8.47\times10^{-4} \pm 5.03*10^{-5}$)
	150°C	690	5×10^5	2.31	1.99×10^{-3} ($1.65\times10^{-3} \pm 2.18*10^{-4}$)
TTOTCl	RT	1288	5×10^5	3.30	1.01×10^{-3} ($8.23\times10^{-4} \pm 1.84*10^{-4}$)
	160°C	1192	5×10^5	3.05	1.36×10^{-3} ($1.11\times10^{-3} \pm 1.15*10^{-4}$)

[a] Above values are obtained from at least four devices.

Table 3-21. Dielectric constant and electron mobility of TTOTF and TTOTCl blend films.

Blend Film	Temp	C_g (pF) [a]	f (Hz)	ε_r[a]	$\mu_{e,max}$ ($\mu_{e,avg}$ ± std) ($cm^2\ V^{-1}\ S^{-1}$) [a]
TTOTF:Y6	150°C	1449	5×10^5	4.16	6.26×10^{-4} ($5.17\times10^{-4} \pm 8.44\times10^{-5}$)
TTOTCl:Y6	160°C	1871	5×10^5	4.42	6.12×10^{-4} ($4.40\times10^{-4} \pm 1.37\times10^{-4}$)

[a] Above values are obtained from eight devices.

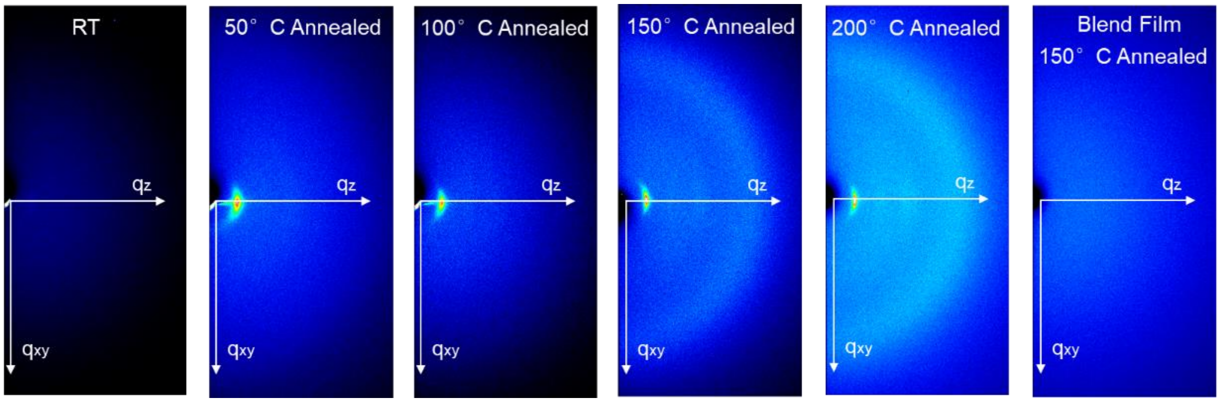

Figure 3-17. 2D-GIXD patterns of the TTOTF neat and blend films at different annealing temperatures.

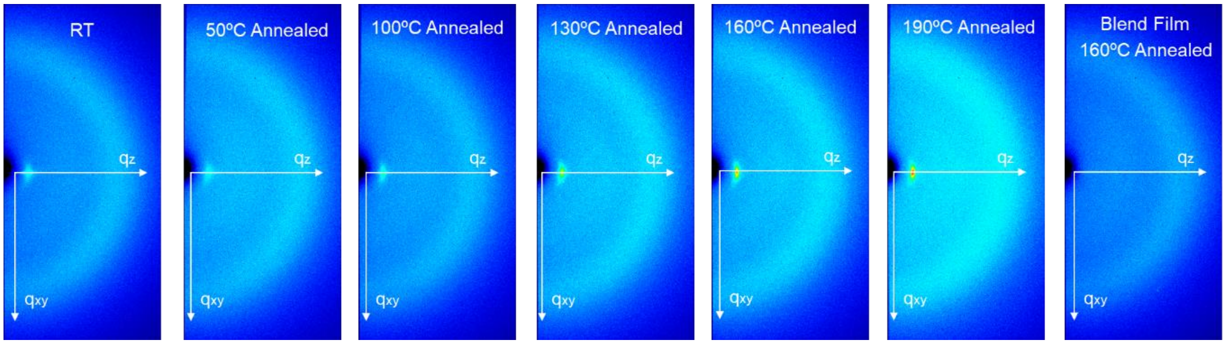

Figure 3-18. 2D-GIXD patterns of the TTOTCl neat and blend films at different annealing temperatures.

Chapter 4 Summary and future directions

This thesis presents the successful design, synthesis and characterization of a series of TO based conjugated polymers donors for non-fullerene OSCs. Previously, our group reported two TO based polymer donors PTOBT and PBDTTO, which are copolymers of TO with common D building blocks BT and BDT, respectively, have shown good device performances of 9.04% and 13.29% when matching with the non-fullerene acceptor ITIC and Y6. However, the SCLC hole mobility of PTOBT and PBDTTO remained relatively low ($< 3 \times 10^{-4}$ $cm^2V^{-1}s^{-1}$) due to the unfavourable edge-on orientation or disordered molecular packing of the polymer films.

In Chapter 2, to improve the steric repulsion caused by alkyloxime side chains and the adjacent BDT unit, a thiophene unit was incorporated to act as a π bridge between the BDT and TO unit. A new wide bandgap polymer donor TTOT was designed and synthesized. It exhibited a wide optical bandgap of 1.98 eV and was able to form complementary light absorption with most of NFAs. In addition, TTOT polymer neat film showed a high hole mobility of up to 3.36×10^{-3} $cm^2V^{-1}s^{-1}$. By matching with the non-fullerene acceptor Y6, the as-cast TTOT-based OSC achieved a PCE of 7.65% with a J_{SC} of 23.58 mA/cm^2, V_{OC} of 0.62 V, and FF of 0.52. However, the incorporation of electron-donating thiophene spacer led to a rise in E_{HOMO} to -5.33 eV, which resulted in the relatively low V_{OC} of the OSCs.

In Chapter 3, to improve the V_{OC} of TTOT-based OSC, halogenation strategies were utilized to downshift the E_{HOMO} of TTOT. Two new wide bandgap polymer donors TTOTF and TTOTCl were designed and synthesized. Both polymers have wide optical bandgaps of over 1.97 eV and similar light absorption profile from 425 to 620 nm. Comparing to TTOT, TTOTF has a lower-lying E_{HOMO} of -5.46 eV and TTOTCl further downshifted the E_{HOMO} to -5.48 eV. The photovoltaic performance of these two polymers were investigated by matching with NFA Y6.

The best TTOTF-based OSC device exhibited a high PCE of 13.57%, with a J_{SC} of 27.61 mA/cm^2, improved V_{OC} of 0.72 V and FF of 0.69. While the optimized TTOTCl-based OSC device showed an even higher PCE of 14.91%, with a record-high J_{SC} of 31.03 mA/cm^2, a V_{OC} of 0.70 V and an FF of 0.68. The largely improved SCLC hole mobility and more balanced μ_h/μ_e ratio in TTOTF and TTOTCl blend films led to a rise in FF and J_{SC} in OSCs. The unencapsulated OSCs based on these two polymers demonstrated excellent long-term air stability, retaining nearly 80% PCE after two months of storage time. Furthermore, by incorporating a hole transport enhancement layer, the PCE of TTOTCl-based OSC was enhanced to 15.96% with an improved V_{OC} of 0.72 V and FF of 0.71. Further investigations and optimizations are needed to fully understand the effect and improve the film quality of the LiTFSI layer. In addition, another approach to further enhance the photovoltaic performance of the TTOTCl-based OSC is to match TTOTCl with non-fullerene acceptors that have higher E_{HOMO}'s than Y6. As a result, a lower energy loss will be obtained in the device through reducing HOMO offset between donor and acceptor materials.

This thesis demonstrated the use of thiophene π spacers in combination with fluorine or chlorine substitutions is highly effective for reducing energy loss, enhancing charge carrier mobility, and improving film morphology in OSCs. Overall, the TO-based polymer TTOTCl was shown to be a promising donor material for fabricating highly efficient and air stable OSCs.

Bibliography

1. Cousins, P. J. *et al.* Generation 3: Improved performance at lower cost. in *2010 35th IEEE Photovoltaic Specialists Conference* 275–278 (2010). doi:10.1109/PVSC.2010.5615850.

2. Goetzberger, A., Hebling, C. & Schock, H.-W. Photovoltaic materials, history, status and outlook. *Mater. Sci. Eng. R Reports* **40**, 1–46 (2003).

3. Kaltenbrunner, M. *et al.* Ultrathin and lightweight organic solar cells with high flexibility. *Nat. Commun.* **3**, 770 (2012).

4. Coakley, K. M. & McGehee, M. D. Conjugated Polymer Photovoltaic Cells. *Chem. Mater.* **16**, 4533–4542 (2004).

5. Gao, L. *et al.* High-Efficiency Nonfullerene Polymer Solar Cells with Medium Bandgap Polymer Donor and Narrow Bandgap Organic Semiconductor Acceptor. *Adv. Mater.* **28**, 8288–8295 (2016).

6. Yan, C. *et al.* Non-fullerene acceptors for organic solar cells. *Nat. Rev. Mater.* **3**, 18003 (2018).

7. Cheng, P. & Zhan, X. Stability of organic solar cells: challenges and strategies. *Chem. Soc. Rev.* **45**, 2544–2582 (2016).

8. Li, C. *et al.* Non-fullerene acceptors with branched side chains and improved molecular packing to exceed 18% efficiency in organic solar cells. *Nat. Energy* **6**, 605–613 (2021).

9. Liu, Q. *et al.* 18% Efficiency organic solar cells. *Sci. Bull.* **65**, 272–275 (2020).

10. Rafique, S., Abdullah, S. M., Sulaiman, K. & Iwamoto, M. Fundamentals of bulk heterojunction organic solar cells: An overview of stability/degradation issues and

strategies for improvement. *Renew. Sustain. Energy Rev.* **84**, 43–53 (2018).

11. Zhao, F., Wang, C. & Zhan, X. Morphology Control in Organic Solar Cells. *Adv. Energy Mater.* **8**, 1703147 (2018).

12. Facchetti, A. Polymer donor–polymer acceptor (all-polymer) solar cells. *Mater. Today* **16**, 123–132 (2013).

13. Sherafatipour, G. *et al.* Degradation pathways in standard and inverted DBP-C70 based organic solar cells. *Sci. Rep.* **9**, 4024 (2019).

14. Krebs, F. C., Gevorgyan, S. A. & Alstrup, J. A roll-to-roll process to flexible polymer solar cells: model studies, manufacture and operational stability studies. *J. Mater. Chem.* **19**, 5442–5451 (2009).

15. Cros, S. *et al.* Definition of encapsulation barrier requirements: A method applied to organic solar cells. *Sol. Energy Mater. Sol. Cells* **95**, S65–S69 (2011).

16. Revoju, S. Molecular Design, Synthesis and Performance Evaluation of Phenothiazine-based Small Molecules for Organic Solar Cells. (2018). doi:10.13140/RG.2.2.27203.50728.

17. Mikhnenko, O. V, Blom, P. W. M. & Nguyen, T.-Q. Exciton diffusion in organic semiconductors. *Energy Environ. Sci.* **8**, 1867–1888 (2015).

18. Lin, J. D. A. *et al.* Systematic study of exciton diffusion length in organic semiconductors by six experimental methods. *Mater. Horizons* **1**, 280–285 (2014).

19. Stübinger, T. & Brütting, W. Exciton diffusion and optical interference in organic donor-acceptor photovoltaic cells. *J. Appl. Phys.* **90**, 3632–3641 (2001).

20. Haugeneder, A. *et al.* Exciton diffusion and dissociation in conjugated polymer/fullerene blends and heterostructures. *Phys. Rev. B - Condens. Matter Mater. Phys.* **59**, 15346–15351 (1999).

21. Li, W., Yao, H., Zhang, H., Li, S. & Hou, J. Potential of Nonfullerene Small Molecules with High Photovoltaic Performance. *Chem. – An Asian J.* **12**, 2160–2171 (2017).

22. Sun, H., Chen, F. & Chen, Z.-K. Recent progress on non-fullerene acceptors for organic photovoltaics. *Mater. Today* **24**, 94–118 (2019).

23. Li, S., Zhang, Z., Shi, M., Li, C.-Z. & Chen, H. Molecular electron acceptors for efficient fullerene-free organic solar cells. *Phys. Chem. Chem. Phys.* **19**, 3440–3458 (2017).

24. Zhang, G. *et al.* Delocalization of exciton and electron wavefunction in non-fullerene acceptor molecules enables efficient organic solar cells. *Nat. Commun.* **11**, 3943 (2020).

25. Huang, J. *et al.* Highly Efficient Organic Solar Cells Consisting of Double Bulk Heterojunction Layers. *Adv. Mater.* **29**, 1606729 (2017).

26. Eftaiha, A. F., Sun, J.-P., Hill, I. G. & Welch, G. C. Recent advances of non-fullerene, small molecular acceptors for solution processed bulk heterojunction solar cells. *J. Mater. Chem. A* **2**, 1201–1213 (2014).

27. Zhang, J., Tan, H. S., Guo, X., Facchetti, A. & Yan, H. Material insights and challenges for non-fullerene organic solar cells based on small molecular acceptors. *Nat. Energy* **3**, 720–731 (2018).

28. Wen, S. *et al.* High-efficiency organic solar cells enabled by halogenation of polymers based on 2D conjugated benzobis(thiazole). *J. Mater. Chem. A* **8**, 13671–13678 (2020).

29. Zhang, S., Qin, Y., Zhu, J. & Hou, J. Over 14% Efficiency in Polymer Solar Cells Enabled by a Chlorinated Polymer Donor. *Adv. Mater.* **30**, 1800868 (2018).

30. Li, S. *et al.* A Wide Band Gap Polymer with a Deep Highest Occupied Molecular Orbital Level Enables 14.2% Efficiency in Polymer Solar Cells. *J. Am. Chem. Soc.* **140**, 7159–7167 (2018).

31. Yuan, J. *et al.* Single-Junction Organic Solar Cell with over 15% Efficiency Using Fused-Ring Acceptor with Electron-Deficient Core. *Joule* **3**, (2019).

32. Zhang, Z. *et al.* Selenium Heterocyclic Electron Acceptor with Small Urbach Energy for As-Cast High-Performance Organic Solar Cells. *J. Am. Chem. Soc.* **142**, 18741–18745 (2020).

33. Cui, Y. *et al.* Single-Junction Organic Photovoltaic Cells with Approaching 18% Efficiency. *Adv. Mater.* **32**, 1908205 (2020).

34. Ma, R. *et al.* Improving open-circuit voltage by a chlorinated polymer donor endows binary organic solar cells efficiencies over 17%. *Sci. China Chem.* **63**, 325–330 (2020).

35. Cai, Y., Huo, L. & Sun, Y. Recent Advances in Wide-Bandgap Photovoltaic Polymers. *Adv. Mater.* **29**, 1605437 (2017).

36. Sun, L. *et al.* Medium-Bandgap Conjugated Polymer Donors for Organic Photovoltaics. *Macromol. Rapid Commun.* **40**, 1900074 (2019).

37. Xie, Y. *et al.* Fibril Network Strategy Enables High-Performance Semitransparent Organic Solar Cells. *Adv. Funct. Mater.* **30**, 2002181 (2020).

38. Wu, Y. *et al.* Rationally pairing photoactive materials for high-performance polymer solar

cells with efficiency of 16.53%. *Sci. China Chem.* **63**, 265–271 (2020).

39. Chao, P. *et al.* Enhanced Photovoltaic Performance by Synergistic Effect of Chlorination and Selenophene π-Bridge. *Macromolecules* **53**, 2893–2901 (2020).

40. Li, W. *et al.* Fused-ring phenazine building blocks for efficient copolymer donors. *Mater. Chem. Front.* **4**, 1454–1458 (2020).

41. Xu, S. *et al.* Optimizing the conjugated side chains of quinoxaline based polymers for nonfullerene solar cells with 10.5% efficiency. *J. Mater. Chem. A* **6**, 3074–3083 (2018).

42. Chen, S. *et al.* Ultrafast Channel II process induced by a 3-D texture with enhanced acceptor order ranges for high-performance non-fullerene polymer solar cells. *Energy Environ. Sci.* **11**, 2569–2580 (2018).

43. Zhao, J. *et al.* Bithieno[3,4-c]pyrrole-4,6-dione-Mediated Crystallinity in Large-Bandgap Polymer Donors Directs Charge Transportation and Recombination in Efficient Nonfullerene Polymer Solar Cells. *ACS Energy Lett.* **5**, 367–375 (2020).

44. Lin, Y. *et al.* An Electron Acceptor Challenging Fullerenes for Efficient Polymer Solar Cells. *Adv. Mater.* **27**, 1170–1174 (2015).

45. Fan, B. *et al.* Achieving over 16% efficiency for single-junction organic solar cells. *Sci. China Chem.* **62**, 746–752 (2019).

46. Ma, Y., Kang, Z. & Zheng, Q. Recent advances in wide bandgap semiconducting polymers for polymer solar cells. *J. Mater. Chem. A* **5**, 1860–1872 (2017).

47. Duan, C., Huang, F. & Cao, Y. Recent development of push–pull conjugated polymers for bulk-heterojunction photovoltaics: rational design and fine tailoring of molecular

structures. *J. Mater. Chem.* **22**, 10416–10434 (2012).

48. He, K., Kumar, P., Yuan, Y. & Li, Y. Wide bandgap polymer donors for high efficiency non-fullerene acceptor based organic solar cells. *Mater. Adv.* **2**, 115–145 (2021).

49. Cui, C., Wong, W.-Y. & Li, Y. Improvement of open-circuit voltage and photovoltaic properties of 2D-conjugated polymers by alkylthio substitution. *Energy Environ. Sci.* **7**, 2276–2284 (2014).

50. Cui, Y. *et al.* Achieving Over 15% Efficiency in Organic Photovoltaic Cells via Copolymer Design. *Adv. Mater.* **31**, 1808356 (2019).

51. Cui, C. *et al.* High-performance polymer solar cells based on a 2D-conjugated polymer with an alkylthio side-chain. *Energy Environ. Sci.* **9**, 885–891 (2016).

52. Zhang, Y. *et al.* Indacenodithiophene and Quinoxaline-Based Conjugated Polymers for Highly Efficient Polymer Solar Cells. *Chem. Mater.* **23**, 2289–2291 (2011).

53. Zhang, Y. *et al.* Fluorination vs. chlorination: a case study on high performance organic photovoltaic materials. *Sci. China Chem.* **61**, 1328–1337 (2018).

54. Zhao, Q., Qu, J. & He, F. Chlorination: An Effective Strategy for High-Performance Organic Solar Cells. *Adv. Sci.* **7**, 2000509 (2020).

55. Qian, D. *et al.* Design, Application, and Morphology Study of a New Photovoltaic Polymer with Strong Aggregation in Solution State. *Macromolecules* **45**, 9611–9617 (2012).

56. Zhang, L. *et al.* Reduced Energy Loss in Non-Fullerene Organic Solar Cells with Isomeric Donor Polymers Containing Thiazole π-Spacers. *ACS Appl. Mater. Interfaces* **12**, 753–762

(2020).

57. Jung, J. W., Liu, F., Russell, T. P. & Jo, W. H. Medium Bandgap Conjugated Polymer for High Performance Polymer Solar Cells Exceeding 9% Power Conversion Efficiency. *Adv. Mater.* **27**, 7462–7468 (2015).

58. Cuesta, V. *et al.* Increase in efficiency on using selenophene instead of thiophene in π-bridges for D-π-DPP-π-D organic solar cells. *J. Mater. Chem. A* **7**, 11886–11894 (2019).

59. Agneeswari, R. *et al.* Influence of thiophene and furan π–bridge on the properties of poly(benzodithiophene-alt-bis(π–bridge)pyrrolopyrrole-1,3-dione) for organic solar cell applications. *Polymer (Guildf).* **229**, 123991 (2021).

60. Zhang, S. *et al.* Enhanced Photovoltaic Performance of Diketopyrrolopyrrole (DPP)-Based Polymers with Extended π Conjugation. *J. Phys. Chem. C* **117**, 9550–9557 (2013).

61. Pathiranage, T. M. S. K., Magurudeniya, H. D., Biewer, M. C. & Stefan, M. C. Effect of thiophene spacers in benzodithiophene-based polymers for organic electronics. *J. Polym. Sci. Part A Polym. Chem.* **55**, 3942–3948 (2017).

62. Liu, D. *et al.* Molecular design of a wide-band-gap conjugated polymer for efficient fullerene-free polymer solar cells. *Energy Environ. Sci.* **10**, 546–551 (2017).

63. Nikolka, M. *et al.* High-mobility, trap-free charge transport in conjugated polymer diodes. *Nat. Commun.* **10**, 2122 (2019).

64. Riede, M., Spoltore, D. & Leo, K. Organic Solar Cells—The Path to Commercial Success. *Adv. Energy Mater.* **11**, 2002653 (2021).

65. Xue, R., Zhang, J., Li, Y. & Li, Y. Organic Solar Cell Materials toward

Commercialization. *Small* **14**, 1801793 (2018).

66. He, K. *et al.* Alkyloxime Side Chain Enabled Polythiophene Donors for Efficient Organic Solar Cells. *Macromolecules* **53**, 8796–8808 (2020).

67. He, K. *et al.* A Wide Bandgap Polymer Donor Composed of Benzodithiophene and Oxime-Substituted Thiophene for High-Performance Organic Solar Cells. *ACS Appl. Mater. Interfaces* **13**, 26441–26450 (2021).

68. Kahle, F.-J. *et al.* Does Electron Delocalization Influence Charge Separation at Donor–Acceptor Interfaces in Organic Photovoltaic Cells? *J. Phys. Chem. C* **122**, 21792–21802 (2018).

69. Han, G. & Yi, Y. Local Excitation/Charge-Transfer Hybridization Simultaneously Promotes Charge Generation and Reduces Nonradiative Voltage Loss in Nonfullerene Organic Solar Cells. *J. Phys. Chem. Lett.* **10**, 2911–2918 (2019).

70. Benatto, L., Bassi, M. de J., de Menezes, L. C. W., Roman, L. S. & Koehler, M. Kinetic model for photoluminescence quenching by selective excitation of D/A blends: implications for charge separation in fullerene and non-fullerene organic solar cells. *J. Mater. Chem. C* **8**, 8755–8769 (2020).

71. Xu, J. *et al.* Efficient wide-bandgap copolymer donors with reduced synthesis cost. *J. Mater. Chem. C* (2021) doi:10.1039/D1TC01746B.

72. Feng, K. *et al.* Low-Energy-Loss Polymer Solar Cells with 14.52% Efficiency Enabled by Wide-Band-Gap Copolymers. *iScience* **12**, 1–12 (2019).

73. Yao, C. *et al.* Fluorination of a polymer donor through the trifluoromethyl group for high-

performance polymer solar cells. *J. Mater. Chem. A* **8**, 12149–12155 (2020).

74. Wang, C. *et al.* A zinc(ii) complex of di(naphthylethynyl)azadipyrromethene with low synthetic complexity leads to OPV with high industrial accessibility. *J. Mater. Chem. A* **7**, 24614–24625 (2019).

75. Grant, T. M., Dindault, C., Rice, N. A., Swaraj, S. & Lessard, B. H. Synthetically facile organic solar cells with >4% efficiency using P3HT and a silicon phthalocyanine non-fullerene acceptor. *Mater. Adv.* **2**, 2594–2599 (2021).

76. He, Y. *et al.* A new n-type polymer based on N,N′-dialkoxynaphthalenediimide (NDIO) for organic thin-film transistors and all-polymer solar cells. *J. Mater. Chem. C* **6**, 1349–1352 (2018).

77. Gohier, F., Frère, P. & Roncali, J. 3-Fluoro-4-hexylthiophene as a Building Block for Tuning the Electronic Properties of Conjugated Polythiophenes. *J. Org. Chem.* **78**, 1497–1503 (2013).

78. Menke, S. M., Ran, N. A., Bazan, G. C. & Friend, R. H. Understanding Energy Loss in Organic Solar Cells: Toward a New Efficiency Regime. *Joule* **2**, 25–35 (2018).

79. Burke, T. M., Sweetnam, S., Vandewal, K. & McGehee, M. D. Beyond Langevin Recombination: How Equilibrium Between Free Carriers and Charge Transfer States Determines the Open-Circuit Voltage of Organic Solar Cells. *Adv. Energy Mater.* **5**, 1500123 (2015).

80. Wang, S., Yuan, W. & Meng, Y. S. Spectrum-Dependent Spiro-OMeTAD Oxidization Mechanism in Perovskite Solar Cells. *ACS Appl. Mater. Interfaces* **7**, 24791–24798

(2015).

81. Yuan, W., Zhao, H., Hu, H., Wang, S. & Baker, G. L. Synthesis and Characterization of the Hole-Conducting Silica/Polymer Nanocomposites and Application in Solid-State Dye-Sensitized Solar Cell. *ACS Appl. Mater. Interfaces* **5**, 4155–4161 (2013).

82. Arrechea, S. *et al.* Efficiency improvement using bis(trifluoromethane) sulfonamide lithium salt as a chemical additive in porphyrin based organic solar cells. *Nanoscale* **8**, 17953–17962 (2016).

83. Chen, X., Liang, T., Gao, K., Peng, X. & Cao, Y. Doping porphyrin-based bulk heterojunction solar cells with LITFSI and TFSA. *J. Mater. Chem. C* **5**, 11573–11578 (2017).

84. Wang, S. *et al.* Unveiling the Role of tBP–LiTFSI Complexes in Perovskite Solar Cells. *J. Am. Chem. Soc.* **140**, 16720–16730 (2018).

85. Bartelt, J. A., Lam, D., Burke, T. M., Sweetnam, S. M. & McGehee, M. D. Charge-Carrier Mobility Requirements for Bulk Heterojunction Solar Cells with High Fill Factor and External Quantum Efficiency >90%. *Adv. Energy Mater.* **5**, 1500577 (2015).

86. Ghasemi, M. *et al.* A molecular interaction–diffusion framework for predicting organic solar cell stability. *Nat. Mater.* **20**, 525–532 (2021).

87. Duan, L. & Uddin, A. Progress in Stability of Organic Solar Cells. *Adv. Sci.* **7**, 1903259 (2020).

88. Wang, K., Li, Y. & Li, Y. Challenges to the Stability of Active Layer Materials in Organic Solar Cells. *Macromol. Rapid Commun.* **41**, 1900437 (2020).

89. Sun, H. *et al.* A monothiophene unit incorporating both fluoro and ester substitution enabling high-performance donor polymers for non-fullerene solar cells with 16.4% efficiency. *Energy Environ. Sci.* **12**, 3328–3337 (2019).

90. Yu, R. *et al.* TCNQ as a volatilizable morphology modulator enables enhanced performance in non-fullerene organic solar cells. *J. Mater. Chem. C* **8**, 44–49 (2020).

91. Xu, X. *et al.* Realizing Over 13% Efficiency in Green-Solvent-Processed Nonfullerene Organic Solar Cells Enabled by 1,3,4-Thiadiazole-Based Wide-Bandgap Copolymers. *Adv. Mater.* **30**, 1703973 (2018).